UNIVERSITÀ DELLA CALABRIA

Dipartimento di Fisica

Scuola di Dottorato

In Scienze, Comunicazione e Tecnologie "Archimede"

Indirizzo

Fisica e Tecnologie Quantistiche

Con il contributo di INFN

CICLO XXVIII

ASPECTS OF PHASE TRANSITIONS IN GAUGE THEORIES AND SPIN MODELS ON THE LATTICE

Settore Scientifico Disciplinare

FIS/02 - Fisica Teorica Modelli e Metodi Matematici

Direttore: Ch.mo Prof. Pietro Pantano

Firma _____

Supervisore: Ch.mo Prof. Alessandro Papa

Firma _____

Dottorando: Dott./ssa Francesca Cuteri

Firma _____

"Vorrei essere libero come un uomo
Come l'uomo più evoluto che si innalza
con la propria intelligenza
e che sfida la natura con la forza
incontrastata della scienza

Con addosso l'entusiasmo di spaziare
senza limiti nel cosmo
è convinto che la forza del pensiero
sia la sola libertà"

Giorgio Gaber

Alla mia famiglia
(nonni inclusi)

Contents

Abstract

The main focus of this thesis are phase transitions both in gauge theories, in particular in Quantum ChromoDynamics (QCD), and in two-dimensional spin models. The approach is numeric, relying on dedicated simulation and analysis softwares, and takes advantage of the possibility to discretize our theories, and describe our models, on a lattice.

Three different kind of investigations have been carried out, two of them concerning QCD. The thermal deconfinement/chiral phase transition in QCD at zero chemical potential has been indeed, indirectly studied, respectively via the characterization of color-field flux tubes, as footprints for confinement in $SU(3)$ pure gauge theory, and via a study at imaginary chemical potential for the case of full QCD with two degenerate flavors of dynamical quarks $N_f = 2$.

In the former case a systematic study of the longitudinal profile of the chromoelectric field produced by the strong interaction of a pair of quark and antiquark in the QCD vacuum has been realized, both at zero and nonzero temperature. Measurements have been performed in numerical simulations implementing the appropriate field-related lattice operator. The characteristic sizes of the flux tubes have been extracted through a fitting procedure based on a well known picture for the confinement phenomenon called "dual superconductor model" that traces an analogy between color confinement and superconductivity. Such a picture is found to successfully describe our numerical results for the chromoelectric field distribution at zero temperature. Taking one step further in the dual analogy, the profile of the flux tube has been then studied at finite temperature and across the deconfinement transition. However, results indicate that the analogy cannot be pushed so far: as the temperature is increased towards and above the deconfinement temperature T_c, the amplitude of the field inside the flux tube gets considerably smaller, while the shape of the flux tube does not vary appreciably at the onset of deconfinement. An "evaporation" of flux tubes is observed that has no counterpart in ordinary (type-II) superconductivity and let the tube structure survive the phase transition, consistently with observations in heavy-ion collision experiments.

A somewhat different analysis about the thermal phase transition in $N_f = 2$ QCD (where direct studies are prevented either by the well known sign problem or by high numerical costs) can be carried out at imaginary values of chemical potential that are critical for the Roberge-Weiss (RW) phase transition. In particular, the nature of the RW phase transition at the endpoint of the first order critical RW line has been investigated. It is found to depend on the quark masses in a way that it is a triple first-order point in the limit of zero (infinite) masses and a second order critical endpoint at intermediate masses. Similar results are relevant for the understanding of the nature of the thermal transition at $\mu = 0$.

Coming to spin models and, to be more specific, to two-dimensional spin models characterized by non-Abelian symmetry groups $U(2)$ and $SU(N)$ for $N = 5, 8$, the existence of infinite order (BKT) phase transition has been checked. Such transitions were expected on the basis of analytical computations and have been, indeed, numerically detected in all considered models. By means of finite size scaling analysis it has been also observed that the BKT phase transition that takes place in $U(2)$ models belongs to the universality class of the two-dimensional XY model.

Sintesi in lingua italiana

Alcuni fenomeni critici di particolare interesse fisico, quali la transizione di fase termica nella teoria delle interazioni forti (QCD) e transizioni di fase di ordine infinito in modelli di spin 2D costituiscono il principale oggetto d'indagine in questa tesi. L'approccio è di natura numerica: esso fa affidamento su codici di simulazione e di analisi dedicati e si avvale della possibilità di discretizzare le teorie di gauge, e descrivere i modelli di spin, su reticolo.

Sono stati condotti tre diversi tipi d'indagine, due dei quali riguardanti la QCD. La transizione termica di deconfinamento nella QCD a potenziale chimico nullo è stata, infatti, studiata in maniera indiretta, rispettivamente mediante la caratterizzazione dei tubi di flusso cromoelettrici, impronta del confinamento nella teoria di pura gauge $SU(3)$, e mediante lo studio della QCD con due sapori di quark dinamici $N_f = 2$ a potenziale chimico immaginario non nullo.

Nel primo caso è stato realizzato uno studio numerico sistematico del profilo longitudinale del campo cromoelettrico prodotto dall'interazione forte di una coppia di sorgenti statiche (quark ed antiquark) nel vuoto della QCD. Lo studio è stato condotto sia in condizioni di temperatura nulla che a temperatura finita, entro ed oltre la temperatura critica per la transizione di fase di deconfinamento. Le misure sono state realizzate entro simulazioni numeriche mediante implementazione dell'appropriato operatore di reticolo sensibile al campo di colore. Le taglie caratteristiche dei tubi di flusso sono state estratte mediante una procedura di fit basata su di un ben noto scenario per il fenomeno del confinamento delle cariche di colore detto "modello del superconduttore duale" che traccia un'analogia fra il confinamento di colore e la superconduttività. A temperatura zero si è verificato come il modello descriva con successo le misure realizzate su reticolo. Facendo un passo in avanti nell'analogia della superconduttività duale, il profilo del tubo di flusso è stato studiato anche a temperatura finita e attraverso la transizione di deconfinamento. I risultati indicano che l'analogia non può essere portata avanti fino a questo punto. Si è osservato che, al crescere della temperatura verso ed oltre la temperatura critica di

deconfinamento, l'ampiezza del campo che costituisce il tubo di flusso diminuisce sensibilmente, mentre la forma del profilo del tubo di flusso non varia apprezzabilmente. Si osserva una "evaporazione" del tubo di flusso che non ha controparte nella teoria della superconduttività ordinaria. Il tubo di flusso sopravvive, di fatto, alla transizione di fase consistentemente con le osservazioni negli esperimenti di collisione di ioni ad alta energia.

Una diversa analisi della transizione di fase termica nella QCD per $N_f = 2$ (laddove studi diretti non sono possibili per via del ben noto problema del segno o dell'elevato costo numerico) può essere realizzata a valori immafinari del potenziale chimico che sono critici per la transizione di fase di Roberge- Weiss (RW). In particolare la natura della transizione RW all'estremità della linea critica RW del primo ordine è stata studiata come funzione della massa dei quark. La natura di questa particolare transizione è rilevante per la comprensione della transizione termica a potenziale chimico nullo in QCD. I risultati ci dicono che al punto estremo della linea critica RW si ha una transizione del primo ordine (in un punto triplo) nel limite di masse nulle (infinite), del secondo ordine a masse intermedie.

Venendo ai modelli di spin e, per essere più precisi, a modelli di spin 2D con simmetria non Abeliana di tipo $U(2)$ ed $SU(N)$ con $N = 5, 8$, è stata verificata l'esistenza di transizioni di fase di ordine infinito (BKT). Tali transitioni sono attese sulla base di predizioni analitiche e sono state, di fatto, osservate numericamente in tutti i modelli citati. Per mezzo di una analisi di "finite size scaling" è anche stato osservato che la transizione di fase che ha luogo nei modelli di spin con simmetria $U(2)$ appartiene alla stessa classe di universalità della analoga transizione nel modello XY in due dimensioni.

Introduction

The lattice formulation of Quantum Field Theories (QFT) has been introduced not so long ago by Wilson (1974). The success of lattice theories has been ratified by the possibility to make computations numerically, with the help of modern (super)computers, and by the accurate results (compared to experiments) and predictions produced in the last decades. Among others, there is one particular context in which the introduction of lattice techniques has marked a turning point in scientific research: the Quantum ChromoDynamics (QCD). The lattice formulation provides, indeed, the main useful tool to meet the need of studying the strong interactions, from first principles, in its non-perturbative regime at the typical hadronic energy scales. Beyond QCD applications, critical phenomena in spin models also call for non-perturbative lattice studies.

Critical phenomena and, in particular, phase transitions constitute the leitmotif of this works in which a collection of numerical investigations is presented. The phase transitions that have been studied are:

- the confinement/deconfinement transition in $SU(3)$ pure lattice gauge theory (LGT), indirectly studied through a quantitative analysis of the color flux tubes produced by the interaction of color sources;
- the finite temperature chiral/deconfinement phase transition in $N_f = 2$ QCD from imaginary chemical potential;
- the order/disorder (BKT) phase transition in 2D spin models with non-Abelian $U(N)/SU(N)$ symmetry.

The relevant concepts about phase transitions, critical phenomena and universality are discussed in Chap. 1.

In Chap. 2 an brief introduction on QCD, with particular reference to its lattice version, is given in order to set the context for the investigations on its thermal phase transition.

As an across-the-board topic for our study of both LGT and spin models, numerical methods in lattice theories are addressed in Chap. 3.

The last three chapters in this thesis summarize the main numerical findings in the three different explored contexts.

The investigation on $SU(3)$ flux tubes has been carried on in collaboration with prof. Paolo Cea and dr. Leonardo Cosmai from the University of Bari.

The thermal phase transition in $N_f = 2$ QCD at imaginary chemical potential has been the topic of investigation in a training period spent at the Institute For Theoretical Physics in Frankfurt (Goethe University), under the supervision of prof. Owe Philipsen and in collaboration with members of his research group.

Finally results concerning spin models have been produced in collaboration with prof. Oleg Borisenko and dr. Volodymir Chelnokov from the Bogolyubov Institute for Theoretical Physics of Kiev.

Chapter 1

Phase transitions and Critical phenomena

"Everything must change so that nothing changes"

Giuseppe Tomasi di Lampedusa, *Il Gattopardo (1958)*

The collection of all macroscopic parameters of a thermodynamic system (volume, temperature, pressure, applied external field, magnetization etc.) defines the thermodynamic state of that system. In statistical mechanics, to represent the thermodynamic state of a system, scalar functions called "thermodynamic potentials" are used, that may be written in terms of the partition function of the system. When a smooth change in the thermodynamic state of systems triggers an abrupt modification in the macroscopic physical (e.g. mechanical) properties of the system, we are faced with a *phase transition* and the corresponding value of the relevant macroscopic parameter that has been varied is said to be "critical".

According to the proposed classification, phase transitions fall into two possible categories. They are said to be *discontinuous* or *first order transitions* if there is a latent heat (i.e. a discontinuity in the internal energy of the system) or, more generally, a discontinuity in the first derivative of the relevant thermodynamic potential. They are said to be *continuous transitions* if, instead, no discontinuity in the first derivative of thermodynamic potential is present. It may also happen that a change in the behavior of a system does not correspond to any discontinuity, but just to rapid, but smooth, changes in the thermodynamic potential and all its derivatives: in this case there is no true phase transition, but a so-called *crossover transition*. The sketched distinction is further clarified through concepts like *correlation length* and *phase coexistence* and *symmetry breaking* that will be introduced in what follows.

In particular, the symmetry breaking phenomenon will be dealt with in Sec. 1.1. Sec. 1.2 will be devoted to the case of continuous phase transition and the scaling hypothesis will be discussed in Sec. 1.3

1.1 Phenomenology of phase transitions: symmetry breaking and critical behavior

A relevant quantity for phase transitions phenomenology is the *correlation length* of the system (ξ). It can be conceived (neglecting boundary effects) as the size of the smallest sample of the system showing the same macroscopic properties of the system as a whole. It is the scale of length over which the fluctuations of the microscopic properties of the system are correlated among each other. The actual value of ξ depends on the thermodynamic state of the system and it is sensitive to critical points.

Another quantity which is sensitive to phase transitions, and relevant for their classification, is the *order parameter* measuring the order in the spatial distribution of the microscopic degrees of freedom (dof) of the statistical system. It makes sense to introduce a measure of order since it is connected to the symmetry properties of the system whose breaking/restoration often happens in correspondence to a phase transition. A good order parameter (it can be a scalar as well as a vector and real as well as imaginary) is nonzero in the ordered (less symmetric) phase, while it vanishes in the disordered (more symmetric) phase. The phenomenon of *spontaneous symmetry breaking* accounts for a symmetry of the partition function of a system (formally expressed by its invariance under transformations by elements of the group specifying the symmetry) which is not shared by the states of that system that are actually realized. While local gauge symmetries cannot be spontaneously broken [1], a global symmetry such as Z_2 symmetry in Ising model and $SO(3)$ in Heisenberg model is broken down by the state of the system that is realized in its thermodynamic limit.

It is worth remarking, however, that the symmetry breaking mechanism is not the unique mechanism responsible for critical phenomena. Indeed, a *Berezinskii-Kosterlitz-Thouless* (BKT) phase transition (it will be the topic of Chap. 6) can take place in some systems of low space dimensionality, despite a symmetry breaking is forbidden by the energetics of the system. The main characteristic of a BKT transition is an essential singularity in the thermodynamic potential, while its derivatives of whatever order are continuous, and this behavior is understood as the unbinding of topological objects.

In the case of *first order transitions* (melting of a 3D solid, condensation of a gas into a liquid, etc.), the two (or more) states on either side of the critical point also coexist,

as two distinct states with distinct properties, exactly at the critical point. Beyond the critical point, a unique stable phase is reached whose properties are continuously connected to one of the co-existent phases at the critical point. Various thermodynamic quantities show discontinuous behavior at the critical point. Such transitions often exhibit hysteresis and the correlation length at the transition is generally finite.

In the case of a *continuous transition* (ferromagnetic transition, liquid-gas transition) the correlation length becomes infinite: fluctuations are correlated over all distance scales and a unique critical phase is realized. The two (or more) phases on either side of the critical point must become identical as it is approached. The differences in the various thermodynamic quantities between the competing phases, like the energy density and the magnetization also go to zero smoothly.

In the case of a *crossover transition* (deconfinement transition in QCD with 2+1 physical quarks), there are neither divergences nor singularities in any quantity: only rapid variations and with the location in thermodynamic variables depending on the studied observable. That is why critical regions rather than critical points are identified.

In the phase diagram, which is the graph, with external parameters on the axes, on which the phase of the system at equilibrium is specified for each point (tuple of parameters), phase transitions correspond to phase boundaries between regions of given phases. Boundaries corresponding to first order transitions may cross, and a *triple point* arises, where there is coexistence of three different phases. On the other hand, crossover transitions corresponds to *crossover regions* (no boundary can be identified) and this implies that a first order phase boundary must end before encountering a crossover region: a weakening of the transition (smoothen discontinuities) is expected, until it eventually ends up in a second order *critical end point* (CEP). As a particular case, it may also happen that it is a boundary consisting in triple points to end before a crossover region is met, and its ending is called *tricritical point*.

1.2 Continuous phase transitions: critical exponents and universality

As already stated, continuous phase transitions are characterized by the divergence of the correlation length as the relevant thermodynamic variable reaches its critical value. For definiteness we will now discuss what happens in correspondence to a paramagnet-ferromagnet transition with the relevant thermodynamic variable given by the temperature. As $T \to T_C^+$ an increasing number of microscopic dof (spin variables) become correlated to each other, effectively behaving as a single (rescaled) spin variable on a

scale of distance measured by the correlation length ξ. At the critical temperature the continuous phase transition takes place and $\xi = \infty$, so that critical behavior is dictated by fluctuations on all distance scales.

The strong correlation among an asymptotically infinite number of dof is what makes it difficult to study such kind of critical phenomena, but the *renormalization group* (RG) *approach* provides a solid method for the description of critical behaviors. Furthermore, there is also an advantage brought in by the large correlation lengths: it consists in the fact that the microscopic details of the interaction among the elementary dof become irrelevant, so that classes of systems can be identified whose properties fall in a small number of classes, each characterized only by dimensionality and symmetry properties of the Hamiltonian, rather than by its specific form. This phenomenon goes under the name of universality and is accounted for in the RG approach that also predict the scaling behavior of thermodynamic quantities showing a power-law dependence on the "distance from the critical point" in its vicinity. The powers in such a dependence are called *critical exponents*. Given that $t \equiv {}^{(T-T_C)}/_{T_C}$ and $h \equiv {}^{H}/_{k_B T_C}$ are the *reduced temperature* and *reduced external magnetic field* respectively, the exponents are defined as follows:

$$C \propto |t|^{-\alpha} \tag{1.1}$$

$$m \propto |t|^{\beta} \tag{1.2}$$

$$\chi \propto |t|^{-\gamma} \tag{1.3}$$

$$m \propto |t|^{1/\delta}, \; T = T_C \tag{1.4}$$

$$\xi \propto |t|^{-\nu} \tag{1.5}$$

$$\Gamma(r) \propto r^{-d+2-\eta} \tag{1.6}$$

where d is the dimensionality of the system, C the specific heat, m the magnetization, χ the magnetic susceptibility, ξ the already introduced correlation length and $\Gamma(r)$ the connected two-point correlation function for magnetic variables at distance r. Only the most singular contribution has been taken into account in the above equations and proportionality constants have been neglected. Systems showing the same set of critical exponents belong to the same universality class.

As mentioned, the power laws are not just observed, but predicted by the RG method. The present discussion about the (real space) RG method is inspired to [2–4]. The basic idea behind the RG approach is the correspondence between changes in the length-scale of the thermodynamic system and transformations of the dof and coupling constants such that the partition function is preserved. The length scale is iteratively increased by *coarse-graining*, i.e. by integrating/averaging over all fluctuations within a given length

scale. This is equivalent to studying the behavior of the system over a length-scale $x \to x' = x/b$: it corresponds to a rescaling of the lattice spacing, hence of the cutoff, if the theory lives on a lattice and to a redefinition of the interacting dof. After every coarse-graining step a *rescaling* step of all quantities is necessary by appropriate powers of the chosen length scale factor, moreover adequate transformations for the couplings are looked for, that bring the new effective Hamiltonian, involving only the dof that were not averaged out, in the same functional form as the original one, even tough depending on a new set of coupling constant and on rescaled effective dof. It is just the dependence of the new couplings on the old ones that defines the so-called *renormalization group equations*. The key observation that justifies the use of coarse-graining is the separation of scale between the correlation length at given values of the couplings $\xi(\{g_i\})$ and the distance over which fluctuations are averaged. Being the former much larger than the latter, dof on length scales $a \ll ba \ll \xi$ act as a single unit.

A generic renormalization group equation is the law of transformation for the coupling constants in the theory, induced by the chosen coarse-graining law of transformation for its dof $f\left(\left\{s^{(n)}\right\}\right)$, where variables are indicated with the superscript (n) counting the iterations in the RG procedure. It is convenient to introduce the operator

$$T\left(s^{(n+1)}, s^{(n)}\right) = \begin{cases} 1, & \text{if } s^{(n+1)} = f(\{s^n\}); \\ 0, & \text{otherwise.} \end{cases} \tag{1.7}$$

It is a weight operator satisfying $\sum_{s^{(n+1)}} T\left(s^{(n+1)}, s^{(n)}\right) = 1$, that must preserve the symmetry of the original Hamiltonian. Formally, then a RG group transformation can be expressed as

$$e^{-H^{(n+1)}\left(s^{(n+1)}\right)} = \mathrm{tr}_{s^{(n)}} T\left(s^{(n+1)}, s^{(n)}\right) e^{-H\left(s^{(n)}\right)}, \tag{1.8}$$

and according to the properties of $T\left(s^{(n+1)}, s^{(n)}\right)$ the partition function is left invariant. A RG iteration can be seen as a transformation in the manifold of all the coupling constants compatible with the symmetries of the model being investigated

$$\{g^{(n+1)}\} = \mathcal{R}_b\left(\{g^{(n)}\}\right), \tag{1.9}$$

where $\mathcal{R}$ is, in general, a complicated nonlinear transformation and b indicates the rescaling parameter in the coarse-graining. A sequence of RG iterations gives rise to a *renormalization group trajectory* that is the discrete flow in the manifold of all couplings of the point $\{g\}$ identifying the system. A corresponding flow for the correlation length

is established since that also changes as

$$\xi\left(\mathcal{R}_b^n\left(\{g^{(0)}\}\right)\right) = b^{-n}\xi\left(g^{(0)}\right). \tag{1.10}$$

The simplest asymptotic behavior of the system in the limit of infinitely many iterations is that the corresponding sequence of couplings smoothly converges towards some *fixed points* defined by the relation

$$g^* = \mathcal{R}_b\left(g*\right), \tag{1.11}$$

and with the property that the corresponding correlation length, subject to Eq. (1.10), shows a singularity, $\xi = \infty$, if the fixed point is a *critical point* and the corresponding Hamiltonian becomes scale invariant.

Fixed points are responsible for the universality phenomenon, since they are just properties of the RG transformations and do not depend on the specific form of the starting point Hamiltonian. It is then clear that the above introduced critical exponents characterizing the non-analyticities of ξ and other thermodynamic observables in correspondence to a continuous phase transition, must have their origin in the infinitely many iterations of the RG transformations. Critical points can be classified according to their attractive/repulsive nature by a linearization of the RG equation,

$$g' = g^* + \delta g' = \mathcal{R}_b\left(g^* + \delta g\right) \simeq \mathcal{R}_b\left(g^*\right) + \mathcal{K}_b\delta g = g^* + \mathcal{K}_b\delta g, \quad \text{with} \quad \mathcal{K}_b = \frac{\partial \mathcal{R}_b}{\partial g}, \tag{1.12}$$

and diagonalization of the transformation matrix $\mathcal{K}_b$. Critical phenomena are characterized by the eigenvalues and eigenvectors of the linear transformation matrix $\mathcal{K}_b$. Because of the linearity of $\mathcal{K}_b$ and the semi-group property of the RG transformations, real eigenvalues are generally expressed as $\lambda_i(b) = b^{y_i}$. Displacements in the couplings space from the critical point before and after a RG transformation can be expanded in the basis of the eigenvectors of $\mathcal{K}_b$ and the coefficients in this expansion u_i are called scaling variables since they are found to satisfy $u_i' = b^{y_i}u_i$.

The description of the critical behavior of a system in the RG approach is then reduced to the study of the properties of fixed points by means of the exponents of the eigenvalues of the linearized transformation y_i and the scaling variables u_i. These last are connected through the coupling constants to physical parameters like temperature, pressure, magnetic field, etc. The former are related to the critical exponents and determine the nature of the latter in the sense that a scaling variable is said to be relevant (irrelevant) if $y_i > 0$ ($y_i < 0$) so that the iteration of RG transformations amplifies (deamplifies) displacements from the fixed point. The meaning of universality is further clarified since our analysis tells that Hamiltonians that differ only by interaction terms corresponding

to irrelevant scaling variables give rise to the same critical behavior dictated by the same fixed point in the RG coupling space.

1.3 The scaling hypothesis

As already mentioned the $y_i > 0$ exponents in the eigenvalues of the linearized RG transformation are connected to the critical exponents. In what follows again, for definiteness, the universality class of the critical short-range Ising model is considered, but analogous results hold for any universality class with a single relevant thermal scaling variable and a relevant scaling variable connected to a symmetry breaking field in the action.

The relevant thermal scaling variable and the exponent of the corresponding eigenvalue are indicated by u_t, y_t, while u_h, y_h are the same quantities for the magnetic relevant field. There are also infinitely many irrelevant variables. The starting point, to get to the critical exponents and scaling relations between them, is a critical point in the coupling space for the model, which lies a finite distance apart from the fixed point. A finite number of RG iterations will suffice to bring that point in the region, around the fixed point, where RG equations in their linearized version are valid. The scaling variables in this region will, then, depend analytically on the reduced temperature $t = {}^{(T-T_C)}/_{T_C}$ and reduced field h (measuring the deviations from the critical point) and vanish when $t = h = 0$. We are allowed, indeed, to take u_t and u_h to be proportional to t and h respectively. The key quantity to be used is the singular part of the *reduced free energy per site*. Its RG flow, neglecting the finite contribution coming from the averaged out dof at each RG step, is described by the equation

$$f\left(\{g^{(0)}\}\right) = b^{-nd} f\left(\{g^{(n)}\}\right). \tag{1.13}$$

In terms of the scaling variables the transformation law for the singular free energy, neglecting all the irrelevant variables, becomes

$$f\left(u_t, u_h\right) = b^{-nd} f\left(b^{ny_t} u_t, b^{ny_h} u_h\right). \tag{1.14}$$

The condition $|b^{ny_t} u_t| = u_{t_0}$, on the number n of iterations of the RG transformation, is imposed for arbitrary, but small, u_{t_0}, to ensure the validity of the linear approximation. As a result, Eq. (1.14) rewritten in terms of h and t takes the form

$$f(t,h) = \left|\frac{t}{t_0}\right|^{d/y_t} \Phi\left(\frac{{}^{h}/_{h_0}}{|{}^{t}/_{t_0}|^{y_h/y_t}}\right), \tag{1.15}$$

where Φ is a *scaling function* whose only dependence on the particular system lies in the proportionality constant t_0 and h_0 in the relation between scaling variables and reduced temperature/field.

All thermodynamic critical exponents can be derived by the just obtained scaling law, through the corresponding thermodynamic quantities given by appropriate derivatives of the singular free energy. For the specific heat, one gets $C = {\partial^2 f}/{\partial t^2}\big|_{h=0} \propto |t|^{{d}/{y_t}-2}$ so that

$$\alpha = 2 - \frac{d}{y_t}. \tag{1.16}$$

The spontaneous magnetization is given by $M = {\partial f}/{\partial h}\big|_{h=0} \propto (-t)^{{(d-y_h)}/{y_t}}$ in a way that

$$\beta = \frac{d - y_h}{y_t}. \tag{1.17}$$

The expression for the susceptibility ${\partial^2 f}/{\partial h^2}\big|_{h=0} \propto |t|^{{(d-2y_h)}/{y_t}}$ results in

$$\gamma = \frac{2y_h - d}{y_t}. \tag{1.18}$$

Finally, taking into account how the magnetization M varies with the reduced field h one gets $M \propto h^{{d}/{y_h}-1}$ that gives

$$\delta = \frac{y_h}{d - y_h}. \tag{1.19}$$

The above results constitute a redundant set of relations expressing four thermodynamic critical exponents in terms of only two RG transformation eigenvalues y_t and y_h. The obvious implication is that *scaling relations* between them hold and $\alpha + 2\beta + \gamma = 2$ as well as $\alpha + \beta\,(1 + \delta) = 2$ are two such relations.

Chapter 2

Quantum Chromodynamics

> *"One might think this means that imaginary numbers are just a mathematical game having nothing to do with the real world. From the viewpoint of positivist philosophy, however, one cannot determine what is real. All one can do is find which mathematical models describe the universe we live in. It turns out that a mathematical model involving imaginary time predicts not only effects we have already observed but also effects we have not been able to measure yet nevertheless believe in for other reasons. So what is real and what is imaginary? Is the distinction just in our minds?"*
>
> Stephen William Hawking, *The Universe in a Nutshell (2001)*

The strong interactions, responsible for the hadronic and nuclear structure, are described by a quantum field theory, which is a non-Abelian gauge field theory called quantum chromodynamics (QCD). As a theoretical background to this work the derivation of the QCD Lagrangian from the requirement of local gauge invariance, its quantization within the framework of the Feynman functional-integral formalism, its regularization through the lattice formulation and its renormalization in the continuum limit will be discussed. Aiming at the investigation of some typical aspects of the theory of strong interactions, such as confinement/deconfinement phase transition, its order and the whole phenomenology it involves (in particular, the existence of chromoelectric flux tubes), we will focus our attention to QCD at non-vanishing temperature and density and concentrate on symmetry properties of the QCD action functional that are relevant to our studies and that may undergo spontaneous, rather than explicit, breaking. Finally the QCD phase diagram will be addressed.

Since, as a starting point for the lattice formulation of QCD, we will have to consider the theory quantized within the Feynman functional-integral formalism in its Euclidean

formulation, we will adopt Euclidean formulation already when discussing the continuum theory. The validity of the lattice approach with the supply of numerical methods is indeed based on a structural equivalence between lattice gauge theories and statistical mechanics made explicit in the Euclidean formulation (otherwise the oscillatory integrand appearing in the path integrals could not be interpreted as a Boltzman weight).

2.1 Continuum formulation of QCD

The theory of strongly interacting fields is a particular case of Yang-Mills theories [5] for which the local gauge invariance under local rotations among the $N_c = 3$ color indices of the quarks is required. QCD is an $SU(3)$ gauge theory. The fields whose dynamics is dictated by QCD are fermionic matter fields (quarks) and bosonic gauge fields (gluons). While quarks $\psi(x)$ are Dirac spinors carrying also color index (hence 4×3 components objects) and appearing in six possible flavors, gauge fields $A_\mu(x)$, describing color-charged gluons, are Lorentz vector fields whose components are matrices belonging to the algebra $\mathcal{L}SU(3)$ of the $SU(3)$ group[1]. The action will include a free fermionic term, a free bosonic and boson-boson interacting term and a fermion-boson interacting term. We start by discussing the fermionic and fermion-boson interacting parts of the QCD action, which is a Lorentz scalar bilinear functional of the fermionic fields

$$S_F\left[\psi, \bar{\psi}, A_\mu\right] = \sum_{f=1}^{N_f} \int d^4x\, \bar{\psi}^{(f)}(x) \left(\gamma_\mu D_\mu(x) + m^{(f)}\right) \psi^{(f)}, \tag{2.1}$$

with the index f of the sum running over N_f different quark flavors and

$$D_\mu(x) = \partial_\mu + iA_\mu(x). \tag{2.2}$$

In the action the γ matrices appear that are 4×4 matrices in Dirac space obeying the Euclidean anticommutation relations

$$\{\gamma_\mu, \gamma_\nu\} = 2\delta_{\mu\nu}. \tag{2.3}$$

The precise expression for the action is justified by the fact that from it the Euclidean Dirac equation in presence of an external field $A_\mu(x)$ can be obtained. At this point the invariance of the QCD action,

$$S_F\left[\psi', \bar{\psi}', A'_\mu\right] = S_F\left[\psi, \bar{\psi}, A_\mu\right], \tag{2.4}$$

[1] In terms of the generators T_a of $SU(3)$, $A_\mu(x) = A^a_\mu(x)\, T_a$, $a = 0, \ldots, 8$

under local rotations in color space has to be required. Such rotations are realized by 3×3 special unitary matrices $U(x)$ acting on the fermion fields (in the fundamental representation of the group) as

$$\psi(x) \to \psi'(x) = U(x)\,\psi(x), \qquad \bar{\psi}(x) \to \bar{\psi}'(x) = \bar{\psi}(x)\,U^{\dagger}(x). \tag{2.5}$$

By analogy with the QED case, the action in Eq. (2.1) already contains the so-called *covariant derivative* $D_{\mu}(x)$, which is the quantity, with the same transformation properties under gauge rotations as the fermionic fields $\psi(x)$, needed to ensure gauge invariance. The way gauge transformations act on gauge fields, as well as the same presence of gauge fields, is fixed by the gauge-invariance requirement:

$$A_{\mu}(x) \to A'_{\mu}(x) = U(x)\,A_{\mu}(x)\,U^{\dagger}(x) + i\,(\partial U(x))\,U^{\dagger}(x). \tag{2.6}$$

To complete the QCD action, the gluon action term governing the dynamics of gauge fields must be taken into account and be locally gauge invariant in its turn. The gluon action is constructed, by analogy to the QED case, starting from the commutator between covariant derivatives (in QED this provides us with the electromagnetic field strength tensor). What one gets in the QCD case is

$$\begin{aligned} F_{\mu\nu}(x) &= -i\,[D_{\mu}(x), D_{\nu}(x)] && (2.7)\\ &= \partial_{\mu}A_{\nu}(x) - \partial_{\nu}A_{\mu}(x) + i\,[A_{\mu}(x), A_{\nu}(x)] && (2.8)\\ &= \sum_{i=1}^{8}\left[\partial_{\mu}A^{i}_{\nu}(x) - \partial_{\nu}A^{i}_{\mu}(x) - f_{ijk}A^{j}_{\mu}(x)\,A^{k}_{\nu}(x)\right]T_i && (2.9) \end{aligned}$$

The gauge-invariant, Lorentz scalar gauge action can take the form

$$\begin{aligned} S_G[A] &= \frac{1}{2g^2}\int d^4x\ \mathrm{tr}\,[F_{\mu\nu}(x)\,F_{\mu\nu}(x)] && (2.10)\\ &= \frac{1}{4g^2}\sum_{i=1}^{8}\int d^4x\left[F^{i}_{\mu\nu}(x)\,F^{i}_{\mu\nu}(x)\right]. && (2.11) \end{aligned}$$

Quadratic pieces appear in the field strength tensor that are responsible for self interactions. With the QCD action at hand, one can write the expectation value of a generic observable in the path integral formalism,

$$\langle\mathcal{O}\rangle = \frac{\int \mathcal{D}\bar{\psi}\mathcal{D}\psi\mathcal{D}A_{\mu}\,\mathcal{O}\left[\bar{\psi},\psi,A_{\mu}\right]\,e^{-S_{QCD}}}{\int \mathcal{D}\bar{\psi}\mathcal{D}\psi\mathcal{D}A_{\mu}\,e^{-S_{QCD}}}, \tag{2.12}$$

where $S_{QCD} = S_F\left[\psi,\bar{\psi},A_{\mu}\right] + S_G[A]$.

2.1.1 Finite temperature continuum QCD

The partition function associated with a quantum mechanical system in contact with a heat bath at temperature T is the canonical ensemble partition function given by

$$Z = \mathrm{tr}\left[e^{-\beta \hat{H}}\right], \tag{2.13}$$

where $\beta = 1/k_B T \equiv 1/T$. On the other hand, if one considers (here we use the argument given in [6]) a quantum system whose state $|q\rangle = |q_1, q_2, \ldots, q_n\rangle$ is the simultaneous eigenstate of the coordinate operators Q_i with eigenvalues q_n for the n d.o.f. of the system, its partition function is

$$Z = \int \prod_{i=1}^{n} dq_i \left\langle q \left| e^{-\beta H} \right| q \right\rangle. \tag{2.14}$$

The corresponding path integral representation in configuration space, once introduced and integrated over conjugate momenta, is

$$Z = \int_q^q \mathcal{D}q \, e^{-\int_0^\beta d\tau \int d^3x \, \mathcal{L}(q,\dot{q})}, \tag{2.15}$$

where $\mathcal{L}$ is the Euclidean Lagrangian density. This path integral is a sum over all closed paths starting/arriving in q at "imaginary time" $\tau = 0/\tau = \beta$, i.e. satisfying $q_i(0) = q_i(\beta)$. The formal translation of the last expression to the case of a bosonic scalar field $\phi(\vec{x}, \tau)$ with Lagrangian density $\mathcal{L}(\phi, \partial_\mu \phi)$ is simply

$$Z = \int_{per} \mathcal{D}\phi \, e^{-\int_0^\beta d\tau \int d^3x \, \mathcal{L}(\phi,\partial_\mu \phi)}, \tag{2.16}$$

with fields at each space point satisfying periodic boundary conditions (BC) $\phi(\vec{x}, 0) = \phi(\vec{x}, \beta)$ and $\beta = 1/T$ being the compactification radius along the time direction on the Euclidean space-time surface where our fields live, that becomes in this way a torus with axis along the spatial direction and a radius becoming infinite only in the limit of vanishing temperature.

Analogous considerations can be made in QCD where one gets, once again, a partition function defined in a space-time with a compact time direction of extent β and fields fulfilling, in this case, periodic BC for gauge fields $A_\mu(\vec{x}, \tau) = A_\mu(\vec{x}, \tau + \beta)$ and anti-periodic BC for fermion fields $\psi(\vec{x}, \tau) = -\psi(\vec{x}, \tau + \beta)$, which ensures Bose/Einstein statistics for the former and Pauli principle for the latter. Needless to say the thermodynamic limit is achieved by sending only the spatial 3-volume to infinity.

Center symmetry and deconfinement

Beyond gauge invariance, that is by construction a symmetry of the QCD action, and beyond Lorentz invariance, there are other symmetry transformations under which the QCD action is invariant.

As a first example we will consider the center $Z(3)$ symmetry which is a symmetry of QCD at finite temperature and is only exactly valid in the limit of infinitely heavy quarks. What makes this symmetry crucial is that it is related to the confinement-deconfinement transition of QCD at finite temperature [7, 8]: as temperature is increased up to a critical value $T_c = 270$ MeV, pure gauge theory undergoes a phase transition from a confined phase (colored objects bound into colorless hadrons) to a deconfined phase (free gluons). As already stated, all bosonic fields at finite temperature have to satisfy periodic BC, of period β with respect to the Euclidean (imaginary) time axis. The $SU(3)$ matrices realizing the gauge transformation do not need to be periodic. Nevertheless, assuming they satisfy the relation

$$U(\tau + \beta, \vec{x}) = zU(\tau, \vec{x}), \tag{2.17}$$

where $z \in SU(3)$, we have that in order for the transformed gauge field to be periodic, i.e. $A'_\mu(\tau + \beta, \vec{x}) = (\tau, \vec{x})$, z has to commute with any $SU(3)$ matrix and be independent on the space-time coordinates. The only $SU(3)$ elements enjoying such properties are the elements of the center $Z(3)$ of the group

$$z = e^{\pi i n/N_c}\mathbb{1}, \quad n = 0, 1, \ldots, N_c - 1. \tag{2.18}$$

We call *center transformation* a transformation consisting in the multiplication of all temporal gauge transformation matrices in a given time slice with the same element z of the center group.

Despite the invariance of the QCD actions under center transformations, gauge-invariant operators can be built, which do not share the same invariance. One such operator is the Polyakov loop, defined as the path ordered product of the gauge fields directed along the Euclidean time axis from 0 to β,

$$L(\vec{x}) = \frac{1}{N_c}\mathrm{tr}\left\{Pe^{ig\int_0^\beta d\tau\, A_4(\tau,\vec{x})}\right\}. \tag{2.19}$$

Under a center symmetry transformation the Polyakov loop transforms as

$$L'(\vec{x}) = zL(\vec{x}). \tag{2.20}$$

If the ground state of the system respects the symmetry of the action, then the possible values for the Polyakov loop related by the center symmetry will occur with the same probability. The expectation value for $L(\vec{x})$ does then vanish since the same number of measurements on average will yield each of the possible values and $\sum_l v e^{2\pi i l/3} = 0$. Anytime $L(\vec{x}) \neq 0$, this signalizes that the center symmetry is spontaneously broken and the specific center sector can be identified from the phase of $L(\vec{x}) = |L(\vec{x})| e^{i\phi}$.

Now comes the physical interpretation of the breaking of center symmetry descending from the physical interpretation of the Polyakov loop: its expectation value is related to the free energy of a single quark

$$\langle L(\vec{x}) \rangle = e^{-\beta \Delta F_q}, \tag{2.21}$$

where ΔF_q is the difference between the free energy of a system with and without a single free quark. To a vanishing $\langle L(\vec{x}) \rangle$ corresponds an infinite amount of free energy to be provided to the system for the creation of a single static free quark state in the confined phase. $\langle L(\vec{x}) \rangle$ takes, instead, a finite nonzero expectation value in the deconfined phase, where the phases of the Polyakov loops cluster around any of the $Z(3)$ roots. The Polyakov loop is an order parameter distinguishing between the confined and the deconfined phase of pure gauge theory. Analogous considerations can be done taking into account the correlator between two Polyakov loops, whose physical interpretation is connected to the potential between a pair of a static quark and antiquark:

$$\left\langle L(\vec{x}) L^{\dagger}(\vec{y}) \right\rangle = e^{-\beta F_{q\bar{q}}(r)} \xrightarrow{r \to \infty} |\langle L \rangle|^2 . \tag{2.22}$$

For a static potential linearly growing at large distances as the confining potential does (with the coefficient of the linearly growing term given by the string tension $\sigma > 0$), $|\langle L \rangle|$ has to vanish.

The crucial role of the center symmetry in interpreting the confinement/deconfinement phase transition has been hypothesized by Svetitsky and Yaffe [8]: their guess was that the critical behavior of 4D $SU(3)$ gauge theory coincides with that of a 3D $Z(3)$ spin model. The order of the deconfinement transition has indeed been found to be first order in the gauge theory exactly as in the corresponding spin model.

A final remark is in order about the explicit breaking of center symmetry in presence of a fermionic contribution to the action. In this case, because of the statistical requirements of anti-periodic BC for fermion fields and of their transformation properties under gauge transformations that are only periodic up to $z \in SU(3)$,

$$\psi'(\vec{x}, \tau + \beta) = U(\vec{x}, \tau + \beta) \psi(\vec{x}, \tau + \beta) = -z U(\vec{x}, \tau) \psi(\vec{x}, \tau) = -z \psi'(\vec{x}, \tau) ; \tag{2.23}$$

the only permissible value for z is $z = 1$, hence no center symmetry is realized. As a consequence $|\langle L \rangle|$ does not need to vanish in the confined phase, where physically pair production screens the confining force. $|\langle L \rangle|$ can still serve as an indicator for confinement, but it is no longer an order parameter and, for physical quark masses, no non-analytic phase transition does happen, but rather a smooth crossover.

2.1.2 Finite density continuum QCD

There are phenomena, in the fragmentation region of heavy ion collisions and in the dense nuclear matter constituting the nuclei of compact neutron stars, where, while temperature is relatively low, the net quark number density (i.e. the difference between the total number of quarks and that of anti-quarks) does not vanish.

Nonzero quark number density phenomena require a description in terms of nonzero quark chemical potential μ, within the grand canonical ensemble. The corresponding expression for the partition function is

$$Z\left(V,T,\mu\right) = \mathrm{tr}\left[e^{-\beta\left(\hat{H}-\mu\hat{N}_q\right)}\right], \tag{2.24}$$

where $\hat{N}_q$ is the quark number operator given by

$$\hat{N}_q = \int d^3x\, \bar{\psi}\left(x\right)\gamma_0\psi\left(x\right) = \int d^3x\, \psi^\dagger\left(x\right)\psi\left(x\right). \tag{2.25}$$

It follows that, with the introduction of the chemical potential, the QCD fermionic action in Eq. (2.1) is simply modified into

$$S_F\left[\psi,\bar{\psi},A_\mu,\mu\right] = \int d^3x \int_0^\beta d\tau\, \bar{\psi}\left(x\right)\left(\gamma_\mu D_\mu\left(x\right) + m - \mu\gamma_0\right)\psi\left(x\right). \tag{2.26}$$

It happens that the integrand in Eq. (2.25) changes its sign under the effect of charge conjugation transformation so that we have $\mu > 0\,(\mu < 0)$ for net quark (anti-quark) excess. On the other hand both the integration measure and the $\mu = 0$ action are invariant under charge conjugation transformations in a way that the partition function is an even function of μ. The chemical potential may also be viewed as a constant, imaginary, time-directed, background $U\left(1\right)$ field coupled to the zeroth component of the fermion current $j^0 = \bar{\psi}\gamma^0\psi$:

$$\mu N_q = -ig\int d^3x\, A_0 j_0, \quad A_0 = i\mu/g. \tag{2.27}$$

Roberge-Weiss symmetry

As Roberge and Weiss have pointed out in their paper in 1986 [9], a new interesting symmetry for QCD with fermions, that looks like a remnant of the $Z(3)$ symmetry holding in the pure-gauge case, is found if a purely imaginary chemical potential $i\mu_i$ is considered. This symmetry and its spontaneous breaking are of particular interest because they can be used to constrain the QCD phase diagram in the physically meaningful real imaginary potential case that is, as we will see later on, too difficult to be studied directly.

The QCD partition function for a purely imaginary chemical potential (the same as in Eq. (2.26) with μ replaced by ${}^{i\mu_i}/_T$) clearly has a periodicity of 2π. What brings us to the discovery of the Roberge-Weiss symmetry, consisting in a periodicity of ${}^{2\pi}/_3$ of the partition function, is the fact that the μ-dependence of the partition function, at finite temperature, can be eliminated from the action integrand and transferred to the BC on fields, by means of a change of variables which is a modification, by a $U(1)$ rotation, of the fermionic fields

$$\psi(\vec{x},\tau) \to \psi'(\vec{x},\tau) = e^{i\frac{\mu_i}{T}\tau}\psi(\vec{x},\tau). \tag{2.28}$$

Boundary conditions on fermionic fields then become

$$\psi(\vec{x},\tau+N_T) = -e^{i\frac{\mu_i}{T}}\psi(\vec{x},\tau). \tag{2.29}$$

Assuming then the periodicity, in the imaginary time direction, up to a $Z(3)$ element of the $SU(3)$ matrices performing gauge transformations, and gauge transforming the partition function, one gets simply new BC

$$\psi(\vec{x},\tau+N_T) = -e^{-i\frac{2\pi k}{3}}e^{i\frac{\mu_i}{T}}\psi(\vec{x},0), \quad k\in\mathbb{Z}. \tag{2.30}$$

We just went, through steps preserving the invariance of the partition function from ${}^{i\mu_i}/_T$ to ${}^{i\mu_i}/_T + {}^{i2\pi k}/_3$ which means that, for the QCD partition function periodicity, we have

$$Z\left(i\frac{\mu_i}{T}\right) = Z\left(i\frac{\mu_i}{T} + i\frac{2\pi k}{3}\right). \tag{2.31}$$

This symmetry unveils an equivalence between discrete imaginary chemical potential values ${}^{\mu_i}/_T = {}^{2\pi n}/_3$ and center transformations preserving the invariance of Z.

In this context, for critical imaginary potential values

$$\left(\frac{\mu_i}{T}\right)_c = \frac{2\pi}{3}\left(n+\frac{1}{2}\right), \quad n=0,\pm1,\pm2,\ldots \tag{2.32}$$

there are transitions between adjacent $Z(3)$ sectors, with the particular center sector identified by the phase of the Polyakov loop $L = |L|\, e^{i\phi}$, while all physical observables stay invariant. Such $Z(3)$ transitions have been predicted from perturbative studies [9] and have been numerically found to be first order phase transition at high temperatures and crossover at low temperatures, where, instead, the periodicity is smoothly realized.

2.1.3 Asymptotic freedom vs. non-perturbative regime

We are now going to move from the continuum to the lattice formulation of QCD. Such a choice is well motivated if one is interested in phenomena concerning the low-energy domain of strong interactions. The reason lies in the dependence of the strong coupling constant on the energy scale.

QCD is an asymptotically free theory [10–12]: the coupling gets weaker and weaker for small quark separations, allowing perturbative calculations for all phenomena in the high-energy/short-distances regime. A perturbative treatment of the theory in the low-energy/long-distances regime is, instead, prevented by the growth of the strong coupling: lattice QCD with its numerical tools is the natural choice for the non-perturbative treatment of QCD.

Renormalization has to be achieved in order to remove divergences appearing in QCD beyond tree level and a regularization procedure is needed to isolate these divergences. What happens is that the renormalization procedure inevitably introduces a *scale* μ. This scale, that is the scale at which the subtraction of divergences takes place, is called *renormalization scale*: it is in principle completely arbitrary, but renormalized finite Green functions depend on it. Variations in the renormalization scale affects the contribution to a given results of tree level diagrams with respect to finite contributions coming from loop diagrams.

The particular choice of μ (as well as the choice of a particular renormalization scheme) affects physical observable quantities, in the sense that it produces different expressions connected by finite renormalizations[2]. The *renormalization group equations* are the differential equations governing the response of renormalized Green functions and parameters to infinitesimal changes of μ such that physical observables are μ-independent. They take forms that are specific to the renormalization scheme employed. The renormalization group equation for the renormalized coupling constant is given in the MS

[2]If exact calculations were doable, expressions for physical quantities would turn out to be equivalent among each other regardless of the μ and renormalization scheme choice. This is not true at any fixed order in perturbation theory

scheme by

$$\beta\left(g_R\right) = \mu \frac{\partial g_R}{\partial \mu}\bigg|_{g,m}, \tag{2.33}$$

where g and m are the bare coupling constant and bare mass regarded as fixed constants. Thus the β function represents the rate of change of the renormalized coupling g_R at the scale μ corresponding to fixed bare g and m. What it tells us is that we are dealing with a *running coupling constant*. It can be shown that for QCD with three colors and n_f approximately massless quarks, the β function to its lowest order is given by

$$\beta\left(g_R\right) = -\frac{b_0 g_R^3}{\left(4\pi\right)^2}, \quad b_0 = 11 - \frac{2}{3} n_f. \tag{2.34}$$

Clearly g_R decrease with increasing μ if $n_f < {}^{33}/_2$ and so does the strong coupling strength defined in analogy with QED as $\alpha_S\left(\mu\right) \equiv {}^{g_R^2}/_{4\pi}$, whose μ dependence can be expressed integrating Eq. (2.34), which has the solution

$$\alpha_S\left(\mu\right) = \frac{4\pi}{\beta_0 \ln\left({}^{\mu^2}/_{\Lambda^2}\right)}, \tag{2.35}$$

where Λ is a *scale parameter*, to be determined experimentally, characterizing the scale of mass at which α_S becomes strong while μ decreases. Eq. Eq. (2.35) tells us that the coupling decreases as the inverse logarithm of the renormalization scale for large values of it: this is what is meant by asymptotic freedom.

Experimental determinations for the mass scale Λ yield $\Lambda \approx 200$ MeV meaning that perturbation theory is valid only at $Q \gg 200$ MeV. On the other hand, the strong coupling at momenta equal or lower than Λ, that is at distances of the order of the size of light hadrons, is such that perturbative expansion breaks down and non-perturbative methods are needed.

2.2 Lattice formulation of QCD

The "benefit" of formulating QCD on the lattice is twofold. First of all, while Green functions for gauge field theories correspond to a system characterized by an infinite number of degrees of freedom, the corresponding path integrals are only mathematically well-defined for systems with a denumerable number of degrees of freedom, whence the necessity of the introduction of a space-time lattice. Secondly, the introduction of the lattice, although it breaks translational and rotation invariance, has the effect of regularizing field theories by rendering the momentum integrations in Feynman integrals ultraviolet finite. The elimination of the short distance contribution to the space-time

integration amounts, indeed, to the introduction of a momentum cutoff. The momentum cutoff will then be removed, in the renormalization procedure, by extracting the continuum limit of the theory where also translational and rotation invariance are recovered. Furthermore, lattice formulation is the most suited method to deal with the non-perturbative aspects of the theory.

Let us now turn our attention straight to the specific case of lattice QCD referring, for a more detailed description, to [6, 13, 14].

For the above mentioned reasons a 4D lattice structure is introduced,

$$\Lambda = \{n = (n_1, n_2, n_3, n_4) \,|n_1, n_2, n_3 = 0, 1, \ldots N-1; n_4 = 0, 1, \ldots N_T - 1\}\,, \qquad (2.36)$$

where N denotes the number of lattice sites in the three spatial directions, while N_T is the number of lattice sites in the temporal direction which, as we will see in a moment, will be smaller than N if we are in the case of nonzero temperature.

In this structure, two adjacent points in a given directions are separated, in that direction, by a distance a which defines the lattice constant and is our unit of distance so that the position of any object in the lattice is identified by the corresponding n value in $x = an$.

In a naive discretization, spinors are placed at the lattice points such that the fermionic degrees of freedom, carrying the same color, Dirac and flavor indices as in the continuum, are $\psi(n)$ and $\bar{\psi}(n)$ with $n \in \Lambda$.

In the continuum the action S_F^0 for a free fermion field is given by Eq. (2.1), but on the lattice both the integral over space-time and the partial derivative, are discretized to obtain the expression

$$S_F^0\left[\psi, \bar{\psi}\right] = a^4 \sum_{n\in\Lambda} \bar{\psi}(n) \left(\sum_{\mu=1}^{4} \gamma_\mu \frac{\psi(n+\hat{\mu}) - \psi(n-\hat{\mu})}{2a} + m\psi(n) \right), \qquad (2.37)$$

which is the starting point for the introduction of gauge fields.

The same procedure adopted in the continuum formulation can then be applied to construct a gauge invariant lattice action: once again the introduction of gauge fields is enforced, but with some subtle differences. The local gauge transformations on the lattice are implemented by choosing an element $\Omega(n) \in SU(3)$, for each lattice site n, and transforming the fermion fields according to

$$\psi(n) \to \psi(n)' = \Omega(n)\,\psi(n)\,, \qquad \bar{\psi}(n) \to \bar{\psi}(n)' = \bar{\psi}(n)\,\Omega(n)^\dagger\,. \qquad (2.38)$$

The term that contains the discretized derivative, unlike the mass term, is not invariant and transforms according to

$$\bar{\psi}(n)\,\psi(n+\hat{\mu}) \to \bar{\psi}(n)'\,\psi(n+\hat{\mu})' = \bar{\psi}(n)\,\Omega(n)^{\dagger}\,\Omega(n+\hat{\mu})\,\psi(n+\hat{\mu})\,. \tag{2.39}$$

Gauge invariance can be achieved by the introduction of a gauge field $U_{\mu}(n)$ labeled by position n and direction μ indices, so that each $U_{\mu}(n)$ lives on the link connecting the sites n and $n+\hat{\mu}$ and we call it a *link variable*. If we define the gauge transformation of the new field by

$$U_{\mu}(n) \to U_{\mu}(n)' = \Omega(n)\,U_{\mu}(n)\,\Omega(n+\hat{\mu})^{\dagger}\,, \tag{2.40}$$

the quantity $\bar{\psi}(n)\,U_{\mu}(n)\,\psi(n+\hat{\mu})$ happens to be gauge invariant.

Link variables pointing in the negative μ direction, although not independent, are introduced for notational convenience according to the definition

$$U_{-\mu}(n) \equiv U_{\mu}(n-\hat{\mu})^{\dagger}\,, \tag{2.41}$$

and transform according to

$$U_{-\mu}(n) \to U_{-\mu}(n)' = \Omega(n)\,U_{-\mu}(n)\,\Omega(n-\hat{\mu})^{\dagger}\,. \tag{2.42}$$

It is to be noticed that gluon fields are introduced in the lattice formulation as elements of the gauge group, while in the continuum formulation they were elements of the algebra associated with that group.

The connection between group-valued links and algebra-valued gauge fields is realized in the gauge transporter

$$G(x,y) = Pe^{ig\int_{\mathcal{C}_{xy}} A\cdot ds}, \tag{2.43}$$

which is the path ordered exponential integral of the gauge field A_{μ} along some curve $\mathcal{C}_{xy}$ connecting x and y, with the property of transforming as $U_{\mu}(n)$ does. It is possible to introduce an algebra-valued lattice gauge fields defined by the relation

$$U_{\mu}(n) = e^{igaA_{\mu}(n)}, \tag{2.44}$$

meaning that, up to the first order, $U_{\mu}(n)$ can be interpreted as a lattice version of the gauge transporter connecting n to $n+\hat{\mu}$.

The so-called *naive fermion action* for fermions in an external gauge field may, then, be written as

$$S_F\left[\psi,\bar{\psi},U\right]=a^4\sum_{n\in\Lambda}\bar{\psi}\left(n\right)\left(\sum_{\mu=1}^{4}\gamma_\mu\frac{U_\mu\left(n\right)\psi\left(n+\hat{\mu}\right)-U_{-\mu}\left(n\right)\psi\left(n-\hat{\mu}\right)}{2a}+m\psi\left(n\right)\right) \tag{2.45}$$

and the gauge-invariance principle is satisfied by construction, that is $S_F\left[\psi',\bar{\psi}',U'\right]=S_F\left[\psi,\bar{\psi},U\right]$. It can be shown that in the naive continuum limit $a\to 0$, the action in Eq. (2.45) approaches the corresponding continuum form.

2.2.1 Pure gauge theory on the lattice

The subsequent step, in analogy with the continuum case is the construction of the bosonic part of the action. We have to construct a lattice gauge invariant action in terms of the link variables, with the condition that, in the naive continuum limit $a\to 0$, the continuum counterpart must be recovered. Traces over closed loops of link variables, which are gauge-invariant, are good candidates for the construction of the gauge action.

A possible gluon action with the correct naive continuum limit (the first to be introduced in [15]) contains the simplest closed loop that can be defined on the lattice, i.e. the so-called *plaquette*, which is the following path-ordered product of link variables

$$\begin{aligned}U_{\mu\nu}\left(n\right)&=U_\mu\left(n\right)U_\nu\left(n+\hat{\mu}\right)U_{-\mu}\left(n+\hat{\mu}+\hat{\nu}\right)U_{-\nu}\left(n+\hat{\nu}\right)\\&=U_\mu\left(n\right)U_\nu\left(n+\hat{\mu}\right)U_\mu\left(n+\hat{\nu}\right)^\dagger U_\nu\left(\hat{\nu}\right)^\dagger.\end{aligned} \tag{2.46}$$

The Wilson gauge action is a sum over all plaquettes, with each plaquette counted with only one orientation,

$$S_G\left[U\right]=\frac{2}{g^2}\sum_{n\in\Lambda}\sum_{\mu<\nu}\mathrm{Re}\,\mathrm{tr}\left[I-U_{\mu\nu}\left(n\right)\right]. \tag{2.47}$$

The factor $2/g^2$ is dictated by the continuum limit requirement

$$\lim_{a\to 0}S_G\left[U\right]=S_G\left[A\right], \tag{2.48}$$

with $S_G\left[A\right]$ denoting the gauge action in the continuum Euclidean formulation.

The general form for vacuum expectation value of a generic operator $\hat{O}$, to which the functional O corresponds, can be written in terms of the complete naive expression for

the lattice QCD path integral:

$$\langle\Omega|\, O\,|\Omega\rangle = \langle O\rangle = \frac{\int DU\, D\bar{\psi}\, D\psi O\left[U,\psi,\bar{\psi}\right] e^{-S_F\left[\psi,\bar{\psi},U\right]-S_G[U]}}{\int DU\, D\bar{\psi}\, D\psi e^{-S_F\left[\psi,\bar{\psi},U\right]-S_G[U]}}. \tag{2.49}$$

The integral is over all field configurations. What renders it mathematically manageable, is the fact that, on the lattice, original quantum fields are reduced to a countable number of classical variables. Correspondingly the path integral measures are defined as

$$D\bar{\psi}\, D\psi = \prod_{n\in\Lambda}\prod_{f,\alpha,c} d\bar{\psi}^{(f)}\,(n)_{\alpha,c}\, d\psi^{(f)}\,(n)_{\alpha,c}\,, \tag{2.50}$$

with f,α,c flavor, Dirac and color index respectively, and

$$DU = \prod_{n\in\Lambda}\prod_{\mu=1}^{4} dU_\mu\,(n)\,. \tag{2.51}$$

This is not the end of the story since the spinors variables have to be turned into anti-commuting variables to include the correct Fermi-Dirac statistical behavior for fermion fields. Before addressing fermion fields, it is useful to introduce observables consisting in traces of products of link variables along closed loops, whose physical interpretation has to do with the potential between static color sources and their (de)confinement.

The Wilson loop

A Wilson loop consists of two so-called *Wilson lines* and two temporal transporters. A Wilson line corresponds to a path $\mathcal{C}_{nm}$ connecting two different spatial points $\mathbf{n}$ and $\mathbf{m}$ by means of the ordered product of link variables whose time argument is fixed to the value n_t,

$$S\,(\mathbf{m},\mathbf{n},n_t) = \prod_{(\mathbf{k},j)\in\mathcal{C}_{nm}} U_j\,(\mathbf{k},n_t)\,. \tag{2.52}$$

A temporal transporter instead, corresponds to a path on the lattice which is a straight line in the temporal directions, obtained as an ordered product of link variables all situated at a given spatial position, say $\mathbf{n}$, and connecting two temporal points, say 0 to n_t

$$T\,(\mathbf{n},n_t) = \prod_{j=0}^{n_t-1} U_4\,(\mathbf{n},j)\,. \tag{2.53}$$

The Wilson loop in its whole is obtained by taking the trace of the product of the Wilson lines and gauge transporters attached to each other to give a closed loop

$$\begin{aligned} W[U] &= \operatorname{tr}\left[S(\mathbf{m},\mathbf{n},n_t)\,T(\mathbf{n},n_t)^{\dagger}\,S(\mathbf{m},\mathbf{n},0)^{\dagger}\,T(\mathbf{m},n_t)\right] \\ &= \operatorname{tr}\left[\prod_{(k,\mu)\in L} U_{\mu}(k)\right]. \end{aligned} \tag{2.54}$$

It can be shown that, given a rectangular path on the lattice $\mathcal{C}_{R,T}$, with R and T extension of the loop in the temporal and in each spatial direction respectively, the static quark potential is defined by means of the behavior of the corresponding Wilson loop for large T values,

$$V(R) = -\lim_{T\to\infty}\frac{1}{T}\ln\left\langle W_{\mathcal{C}_{R,T}}[U]\right\rangle, \tag{2.55}$$

because one finds that

$$\left\langle W_{\mathcal{C}_{R,T}}(U)\right\rangle = \frac{\int DU\,D\bar{\psi}\,D\psi W_{\mathcal{C}_{R,T}}[U]\,e^{-S_{QCD}\left[\psi,\bar{\psi},U\right]}}{\int DU\,D\bar{\psi}\,D\psi e^{-S_{QCD}\left[\psi,\bar{\psi},U\right]}} \underset{T\to\infty}{\sim} C\,e^{-TV(R)}, \tag{2.56}$$

where $\left\langle W_{\mathcal{C}_{R,T}}(U)\right\rangle$ is a short-hand notation for $\langle\Omega|\,W_{\mathcal{C}_{R,T}}(U)\,|\Omega\rangle$.

Moreover, the so-called *string tension* can be introduced, which is defined as

$$\sigma \equiv \lim_{R\to\infty}\frac{1}{R}V(R). \tag{2.57}$$

In the confined phase of our theory the potential between a quark and an antiquark is expected to grow linearly with distance. This can be readily understood in the context of a flux tube model connecting the quark and antiquark, where the color-electric field lines are confined in a tube-like shape between the two quarks. No field lines leak out of the tube, therefore the field strengths per unit length remains constant over the extension of the tube and the potential rises linearly with the distance of the quarks. Thus we have, coherently with Eq. (2.57),

$$V(R)\overset{R\to\infty}{\longrightarrow}\sigma R \tag{2.58}$$

and correspondingly the expectation value of the Wilson loop exhibits the asymptotic area law behavior $\left\langle W_{\mathcal{C}_{R,T}}(U)\right\rangle \to e^{-\sigma RT}$.

The Eq. (2.56) is the basis for the so-called *Wilson loop criterion*, which says that static quark confinement holds if Wilson loops obey the area law and the associated string tension is not zero. The Wilson loop criterion is very important since it allows us to

distinguish different phases, with and without static quark confinement, by means of this gauge invariant observable. Therefore the string tension has been used as an order parameter.

The Polyakov loop

At zero temperature, the potential of a static quark-antiquark pair can be determined by studying the ground state expectation value of the Wilson loop observable for large Euclidean times. At finite temperatures, instead, the lattice has a finite extension in the time direction, and the Wilson loop no longer plays this role, but we can consider a different gauge invariant quantity whose expectation value yields a measure of the free energy of a single colored static source and which behave like a order parameter for the deconfining transition. It is the Polyakov loop, the correlators of a pair of which gives a finite temperature definition of the potential between static sources, as a special case of Wilson loop.

The expression for the Polyakov loop on the lattice is the discretized version of the continuum expression we have already met in Eq. (2.19):

$$P(\mathbf{m}) = \mathrm{tr}\left[\prod_{j=0}^{N_T-1} U_4(\mathbf{m}, j)\right]. \tag{2.59}$$

The relations summarizing physical interpretation of Polyakov loop and Polyakov loop correlators are:

$$\left\langle P(\mathbf{m})\, P(\mathbf{n})^{\dagger}\right\rangle = e^{-N_T a V(a|\mathbf{n}-\mathbf{m}|)}, \quad |\langle P\rangle| \sim e^{-\beta F_q}. \tag{2.60}$$

There is no rigorous proof of the identity between the potential as defined by means of the Polyakov loop and the one connected to Wilson loop expectation value. There only exists a proof of the fact that the string tension derived from the Polyakov loop correlator is bounded from above by the one obtained from the Wilson loop correlator [16].

As we have already mentioned in Sec. 2.1.1 the Polyakov loop acts, at least in pure gauge theory, as an order parameter for the confinement/deconfinement phase transition.

These statement becomes clear if we notice that we may interpret the $\langle P\rangle$ quantity as the probability to observe a single static charge because $|\langle P\rangle|$ is related to the free energy of a single color charge $|\langle P\rangle| \sim e^{-\beta F_q}$. Then, being finite the critical temperature at which the phase transition takes place, the condition $\langle P\rangle = 0$ is realized for $F_q \to \infty$, while $\langle P\rangle$ is finite for finite values of the free energy. This observation is bound to

the phenomenological fact that in the confined phase an infinite energy is required to separate a quark anti-quark pair while the creation of a new pair tied to the old one is more likely to happen.

2.2.2 The continuum limit

The continuum limit of the theory is the limit in which physical observables become insensitive to the underlying lattice structure approaching their physical value. In this sense, the lattice structure acts as a regulator to be removed in the renormalization procedure.

The so-called *naive continuum limit* $a \to 0$ consists in checking that the $SU(N)$ Wilson gauge action approached the corresponding continuum action. This was true for our choice of action, but there exists an infinite number of lattice actions characterized by the same naive continuum limit. What matters is that when removing the lattice cutoff, for $a \to 0$, physical observables should become independent of a and agree with the corresponding experimental values. The fact that a discrete action tends to the correct continuous one in the naive limit does not suffice to ensure that the discrete theory possesses a true continuum limit corresponding to the interacting field theory we are interested. Moreover the a-independence of physical observables implies a nontrivial dependence of the bare parameters on the cutoff a.

A necessary condition for a lattice field theory to be referable in the continuum limit to a well defined field theory is that it must exhibit a critical region in parameter (coupling, masses) space, where the correlation lengths ξ diverge signalizing that the system lost its memory of the underlying lattice structure. This condition can be deduced by simply requiring the finiteness of the physical masses, in the spectrum of our theory, and traces the analogy between cutoff removal in field theory and the RG flow towards a fixed point in the RG approach for statistical systems (see Chap. 1).

In the case of a pure gauge theory there is only one parameter which has to be tuned in a way to bring the system near its criticality: it is the dimensionless bare coupling g_0, on which the correlation length in lattice units must depend in a way that

$$\hat{\xi}\left(g_0\right) \underset{g_0 \to g_0^*}{\longrightarrow} \infty, \tag{2.61}$$

if the system presents, as required in the limit $a \to 0$, a fixed point g_0^*. The correlation length ξ depends both on g_0, by virtue of the requirement in Eq. (2.61), and on a because $\xi = \hat{\xi} a$, but the fact that Eq. (2.61) holds only in the $a \to 0$ limit signalizes an implicit dependence of $\hat{\xi}$ on a which occurs as a dependence on a of the bare coupling.

An important consequence of this dependence is that, for dimensional reasons, the existence of a functional dependence of the kind $g_0 = f(a)$ implicitly introduces a mass scale Λ_L in our theory. Since, for sufficiently small a values, a universal function $g_0(a)$ must exists, which ensures the finiteness of any physical observable, the Λ_L value is univocally determined for a fixed lattice action, and it constitutes the scale by means of which we are able to extract physical quantities starting from the dimensionless quantities numerically measured.

The functional form of the connection between g_0 and a has to be determined, if we have to understand how to reach the continuum limit of the theory and to give a meaning to the measuring process.

Given an observable Θ with mass dimension d_Θ, the numerically measurable quantity is the dimensionless and g_0-dependent $\hat{\Theta}$. What we expect is that the existence of a continuum limit together with an adequate tuning of g_0 with a ensures

$$\Theta(g_0(a), a) = \left(\frac{1}{a}\right)^{d_\Theta} \hat{\Theta}(g_0) \underset{\substack{a\to 0 \\ g_0 \to g_0^*}}{\longrightarrow} \Theta_{phys}. \tag{2.62}$$

The quantity g_0, as a function of the dimensionless product $a(\Theta_{phys})^{1/d_\Theta}$, may then be determined, for sufficiently small a, by knowing the dependence of $\hat{\Theta}$ on g_0 and by fixing $\Theta(g_0(a), a)$ at its physical value Θ_{phys}. Any observable may be used for this purpose because of the universality of the relation $g_0(a)$ at small enough a.

The above-described method to obtain $g_0(a)$ involves the use of renormalization group technique and equations based right on the observation that for $a \to 0$ the value of any observable must become independent of a, i.e. RG equations of the form

$$\left[a\frac{\partial}{\partial a} - \beta(g_0)\frac{\partial}{\partial g_0}\right] O(g_0, a, \ldots) = 0 \tag{2.63}$$

must hold, with $\beta(g_0) = -a\frac{\partial g_0}{\partial a}$ is the Callan-Symanzik β-function. $\beta(g_0)$ can be determined by inserting into the RG equation some expression for our observable deduced e.g. in perturbation theory. For the $SU(N)$ case, one finds to lowest order in g_0

$$\beta(g_0) \approx -\frac{11N}{48\pi^2} g_0^3 \tag{2.64}$$

and deduces that g_0 is driven towards its fixed point value $g_0^* = 0$, where $\beta(g_0) = 0$, when the lattice spacing a is decreased. The continuum limit is realized at vanishing bare coupling. Integrating $\beta(g_0)$ we have

$$a = \frac{1}{\Lambda_L} e^{-\frac{1}{2\beta_0 g_0^2}}, \tag{2.65}$$

with $\beta_0 = {}^{11N}/_{48\pi^2}$ and the appearance of the above introduced integration constant with the dimension of a mass as a scale parameter for our theory. Including N_F flavors of massless quarks and considering the first two orders in g_0 in the power expansion for the β-function, i.e. with

$$\beta\left(g_0\right) = -\beta_0 g_0^3 - \beta_1 g_0^5, \qquad \beta_0 = \frac{1}{16\pi^2}\left(11 - \frac{2}{3}N_F\right), \quad \beta_0 = \frac{1}{\left(16\pi^2\right)^2}\left(102 - \frac{38}{3}N_F\right) \tag{2.66}$$

the results are:

$$a = \frac{1}{\Lambda_L} R\left(g_0\right), \qquad R\left(g_0\right) = \left(\beta_0 g_0^2\right)^{-\beta_1/2\beta_0} e^{-1/\beta_0 g_o^2}. \tag{2.67}$$

The problem we are faced with when considering the continuum limit, consists in recognizing the region in the coupling constant space where we can extract continuum physics while performing numerical calculations on finite lattices. According to Eq. (2.67), and given the condition expressed by Eq. (2.62), we deduce that for $g_0 \approx g_0^* = 0$,

$$\hat{\Theta}\left(g_0\right) \underset{g_0 \to 0}{\approx} \hat{C}_\Theta \left(R\left(g_0\right)\right)^{d_\Theta} \tag{2.68}$$

must hold, $\hat{C}_\Theta$ being a dimensionless constant to be determined by studying the ratio ${}^{\hat{\Theta}(g_0)}/_{(R(g_0))^{d_\Theta}}$ as a function of g_0 and noticing the *asymptotic scaling* of this quantity.

Within the scaling region one hence obtains

$$\Theta_{phys.} = \hat{C}_\Theta \left(\Lambda_L\right)^{d_\Theta}. \tag{2.69}$$

Only within the scaling window continuum physics can be extracted from numerical calculations.

2.2.3 Fermions on the lattice: Wilson fermions

A naive discretization of the fermionic part of the QCD action has already been proposed in Sec. 2.2, but that does not take into account the implementation of Fermi statistics for the fermion fields and it contains the lattice artifacts called *doublers*. The former problem is solved by use of Grassmann anticommuting numbers for the fermion fields: anticommuting fermion fields obey Fermi statistics since the v.e.v. of a product of fermion fields change its sign under the interchange of the quantum numbers of any two of the involved fermions. Grassmann calculus tells us what are the rules for computing fermionic Gaussian integrals just like the one defining the fermionic partition function,

once the action is made explicitly bilinear in fermion fields. In particular the *Matthews-Salam formula* identifies the fermionic partition function $Z_F[U]$ as the so-called *fermion determinant*

$$Z_F[U] = \int d\psi_N d\bar{\psi}_N \dots d\psi_1 d\bar{\psi}_1 \, e^{\sum_{i,j=1}^{N} \bar{\psi}_i M_{ij}[U] \psi_j} = \det(M[U]). \tag{2.70}$$

As for the doublers, they are removed by adding the Wilson term to the fermion action. In the single-flavor case the naively discretized fermion action, being bilinear in the fermion fields, takes the form

$$S_F\left[\psi, \bar{\psi}, U\right] = a^4 \sum_{n,m \in \Lambda} \sum_{a,b,\alpha,\beta} \bar{\psi}_{a,\alpha}(n) \; D_{a,b,\alpha,\beta}(n \mid m) \; \psi_{b,\beta}(m), \tag{2.71}$$

with

$$D_{a,b,\alpha,\beta}(n \mid m) = \sum_{\mu=1}^{4} (\gamma_\mu)_{\alpha\beta} \frac{U_\mu(n)_{ab} \, \delta_{n+\hat{\mu},m} - U_{-\mu}(n)_{ab} \, \delta_{n-\hat{\mu},m}}{2a} + m\delta_{\alpha,\beta}\delta_{a,b}\delta_{n,m}. \tag{2.72}$$

Doublers appears already in the free fermion case $U_\mu(n) = \mathbb{1}$, where the expression for the Dirac operator Fourier transformed into the momentum space is

$$\tilde{D}(p) = m\mathbb{1} + \frac{i}{a} \sum_{\mu} \gamma_\mu \sin(p_\mu a). \tag{2.73}$$

Being diagonal, the expression for the Dirac operator in momentum space can be inverted to give the quark propagator that, in the $m = 0$ case, is given by

$$\tilde{D}^{-1}(p) = \frac{-ia^{-1} \sum_\mu \gamma_\mu \sin(p_\mu a)}{a^{-2} \sum_\mu \sin^2(p_\mu a)} \xrightarrow{a \to 0} \frac{-i \sum_\mu \gamma_\mu p_\mu}{p^2}. \tag{2.74}$$

Beyond the single fermion pole at $p = (0,0,0,0)$ of the continuum, on the lattice there appears the doublers: 15 unphysical poles at the edges of the Brillouin zone, whenever all components are either $p_\mu = 0$ or $p_\mu = \pi/a$.

A solution to the doublers problem was suggested by Wilson and consists in adding the so-called *Wilson term* of the form $-a\partial_\mu\partial_\mu$ to the momentum space Dirac operator that becomes

$$\tilde{D}(p) = m\mathbb{1} + \frac{i}{a} \sum_{\mu} \gamma_\mu \sin(p_\mu a) + \mathbb{1} \frac{1}{a} \sum_{\mu} (1 - \cos(p_\mu a)). \tag{2.75}$$

The new term vanishes for $p_\mu = 0$ while providing an additional mass-like term of $2/a$ in correspondence to $p_\mu = \pi/a$ components, that makes doublers decouple in the limit

$a \to 0$. The Wilson Dirac operator in real space is then

$$D_{a,b,\alpha,\beta}\left(n \mid m\right) = \left(m + \frac{4}{a}\right) \delta_{\alpha,\beta}\delta_{a,b}\delta_{n,m} - \frac{1}{2a}\sum_{\mu=\pm 1}^{\pm 4} \left(\mathbb{1} - \gamma_\mu\right)_{\alpha\beta} U_\mu\left(n\right)_{a,b}\delta_{n+\hat{\mu},m}, \quad (2.76)$$

where, by convention, $\gamma_{-\mu} = -\gamma_\mu$.

To study the limit of large quark masses it is convenient to express the Wilson's Dirac operator in term of the hopping mass parameter

$$\kappa = \frac{1}{2\left(am + 4\right)}, \quad (2.77)$$

so that, upon rescaling the fermion fields by a factor $\left(2a\kappa\right)^{-1/2}$, we have

$$D_{a,b,\alpha,\beta}\left(n \mid m\right) = \delta_{\alpha,\beta}\delta_{a,b}\delta_{n,m} - \kappa\sum_{\mu=\pm 1}^{\pm 4} \left(\mathbb{1} - \gamma_\mu\right)_{\alpha\beta} U_\mu\left(n\right)_{a,b}\delta_{n+\hat{\mu},m}. \quad (2.78)$$

Clearly κ becomes smaller and smaller for increasing mass values and one can expand both the quark propagator and the fermion determinant in powers of κ. Such expansions teach us that quark propagators are nothing but sums of non-back-tracking paths of link variables connecting two given lattice sites, with the dominant contribution given, in the static limit, by the straight Wilson line. On the other hand the fermion determinant is a similar sum, but over closed loops of link variables. We remark that the Wilson action enjoys charge conjugation symmetry, parity symmetry, Euclidean reflection symmetry and the Dirac operator is also γ_5-hermitian which implies that the fermion determinant is real.

2.2.4 Temperature and chemical potential

As it has already been pointed out, the partition function for an Euclidean quantum field theory in the functional integral formalism at finite temperature becomes a weighted sum over all field configurations living on a Euclidean space-time surface compactified along the time direction. In two space-time dimensions this surface has the shape of a thorus whose axis lies along the spatial direction. The radius of the thorus becomes infinite in the limit of vanishing temperature. In short, the concept of finite temperature in the path integral formalism is introduced by merely compactifying the Euclidean time direction and imposing consistent periodic BC on the fields.

As for the lattice formulation of these theories, in the thermodynamic limit, the lattice we should consider in the finite temperature case would extend over a finite number N_T of lattice sites in the time direction (the zero-temperature field theory is recovered in

the limit $N_T \to \infty$), while it should have infinite extension $N_S = \infty$ in the other three directions. The inverse temperature β being related to N_T, by

$$\beta = N_T a \tag{2.79}$$

i.e. $T = 1/N_T a$, if we put, for convenience $k_B = 1$. In numerical simulations, N_s must be kept as large as possible so that $N_s \gg N_T$ and the finite volume effects are negligible.

For what concerns the implementation on the lattice of the chemical potential corresponding to a non-vanishing quark number density, it is not doable just by adding to the Dirac operator the temporal component of the conserved vector current $\bar{\psi}(x)\gamma_4\psi(x)$ multiplied by μ. The reason is that such a term in the action would produce, in the continuum limit, a divergence in the energy density. A proper discretization of the chemical potential [17] comes from the determination of the Noether current, corresponding to the global $U(1)$ symmetry, for the lattice action. Such current is expressed by nearest-neighbor terms in the temporal direction, so that the chemical potential is implemented by replacing the temporal hopping term in the Wilson-Dirac operator with

$$-\frac{1}{2a}\sum_{n\in\Lambda}\left(f(a\mu)(\mathbb{1}-\gamma_4)_{\alpha\beta}U_4(n)_{ab}\,\delta_{n+\hat{4},m} + f(a\mu)^{-1}(\mathbb{1}+\gamma_4)_{\alpha\beta}U_4\left(n-\hat{4}\right)^{\dagger}_{ab}\delta_{n-\hat{4},m}\right). \tag{2.80}$$

$f(a\mu)$ is found to be, in its simplest form,

$$f(a\mu) = e^{a\mu}, \tag{2.81}$$

since the original action has to be reproduced for $\mu = 0$ and this requires $f(0) = 1$, the form of the density term requires $f(a\mu) = 1 + a\mu + \mathcal{O}(a\mu)^2$ and time reflection invariance wants $f(a\mu) = 1/f(-a\mu)$. Also the physically observed particle-antiparticle asymmetry is built in through this choice since it favors, by $e^{a\mu}$, the propagation forward in time, while disfavoring the backward propagation by $e^{-a\mu}$. In the sum over closed loops that represents the fermion determinant in the hopping expansion, the hopping factors $f(a\mu)^{\pm 1}$ cancel unless for loops that wind around the compact time direction acquiring a factor $f(a\mu)^{wN_T}$, with w number of windings. It is then easier to modify all temporal hopping terms in a given timeslice by

$$f(a\mu)^{\pm N_T} = e^{\pm\mu/T}, \tag{2.82}$$

with plus (minus) sign for forward (backward) hopping.

The introduction of chemical potential spoils, for $a\mu \neq 0$, the γ_5-hermiticity of the Dirac operator that satisfies instead

$$\gamma_5 D(f)\gamma_5 = D^\dagger(1/f^*). \tag{2.83}$$

This relation means that the Dirac operator is γ_5-hermitian only for $f = 1/f^*$ and, for real $f = e^{a\mu}$, only for $a\mu = 0$. In presence of a nonzero real chemical potential the determinant of the Dirac operator becomes complex and a positive real Boltzmann weight cannot be obtained just by considering even numbers of fermion flavors. The use of importance sampling is then compromised and this is known as the "sign problem".

We remark that an unphysical imaginary value for the chemical potential $\mu = i\eta$, $\eta \in \mathbb{R}$ would instead ensure γ_5-hermiticity since the condition $f = 1/f^*$ gives

$$f(ia\eta) = 1/f(ia\eta)^* = 1/f(-ia\eta) \tag{2.84}$$

and this equality is clearly fulfilled if $f(a\mu) = e^{a\mu}$.

2.3 The phase diagram of QCD

The phase diagram of QCD has been studied for a long time both theoretically (with perturbative high-energy, low-energy hadronic models, rather than numeric non perturbative studies) and experimentally through heavy ion collisions experiment (RHIC) and other high energy experiments at LHC.

In this chapter we have discussed some of the symmetry of the QCD action and their breaking under suitable values for the external macroscopic parameters affecting the phenomenology (temperature and fermionic chemical potential) or the internal microscopic parameters (quark masses, coupling constant). It is just the spontaneous or explicit breaking and/or the restoration of particular symmetries (chiral, center, Roberge-Weiss, etc.) that enriches the phase diagram of QCD with phase transitions whose precise location and order, depending on $T, \mu, m^{(f)}, g$, is not always settled and is the subject of intensive studies.

Here, we only give a short description of the current knowledge about the phase diagram.

The hadronic confined phase is the phase of QCD at low temperatures and densities, where the elementary particles (quarks and gluons) are confined within hadrons. This phase can be well described by the Hadron Resonance Gas Model (HRG), in which hadrons are treated as a free gas. At a certain density threshold, the HRG description

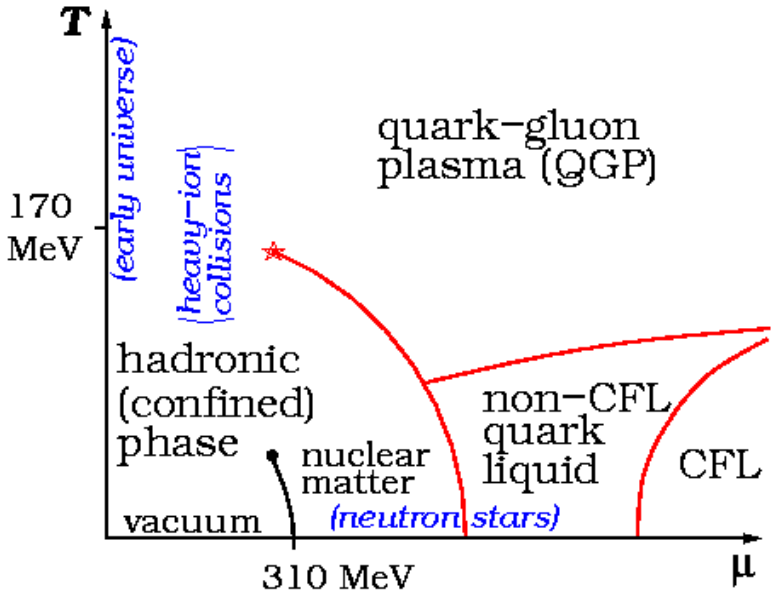

FIGURE 2.1: The QCD $T-\mu$ phase diagram

breaks since all particles start to overlap and eventually cannot be identified any more (transposing the "critical density" to a critical temperature under the assumption of an ideal gas of hadrons and hadronic resonances, $T_C \approx 170$ MeV is found [18]). Moreover, because of the exponential increase of the number of hadron species as a function of the resonance mass produced in hadronic interactions, an upper limit for the temperature of hadronic matter (Hagedorn temperature [19]) is settled at $T_C \approx 150-200$ MeV. Beyond such critical temperature hadronic matter turns into a plasma of quarks and gluons.

The already discussed asymptotic freedom of QCD, due to the running of the coupling constant, indeed ensures that there is a transition, called *thermal transition*, to a deconfined phase (where quarks and gluons can be described as a gas of non-interacting particles) while T and μ increase. In this new phase quarks and gluons, rather than hadrons, are the fundamental degrees of freedom and the so-called *quark-gluon plasma* is formed, which is characterized by deconfinement and also chiral symmetry restoration.

The chiral symmetry of QCD and the corresponding transition and order parameter were not discussed since they are less relevant for our studies, but it is useful to introduce them here shortly. The massless QCD action is symmetric under chiral rotations of the fermion fields.[3] A mass term in the action breaks explicitly such a symmetry, but also in the massless limit a spontaneous breaking of the chiral symmetry takes place at the onset of the deconfinement transition. The observable that acts as an order parameter for the spontaneous breaking of chiral symmetry is the *effective quark mass*, also known as *fermionic condensate* and measured by the expectation value $\langle\bar{\psi}\psi\rangle$. In the confined

[3]Here we are referring to the chiral rotations realized by the transformations $\psi \to \psi' = e^{i\alpha\gamma_5 T_i}\psi$, $\bar{\psi} \to \bar{\psi}' = \psi e^{i\alpha\gamma_5 T_i}$, where $T_i, i = 1, 2, \ldots, N_f^2 - 1$ are the generators of $SU(N_f)$.

case there is a non-vanishing effective constituent quark mass $M_q \approx 0.3$ GeV coming from the spontaneous breaking, so that for $T < T_{ch}$ we have $\langle \bar{\psi}\psi \rangle \neq 0$. On the contrary, in the deconfined phase, for $T > T_{ch}$, chiral symmetry is exactly restored (in the massless case) and $\langle \bar{\psi}\psi \rangle = 0$.

Even if neither the chiral condensate nor the Polyakov loop are strict order parameters for the confinement/deconfinement phase transition for $0 < m_q < \infty$, since the center and chiral symmetries become exact only in the limits $m_q \to \infty$ and $m_q \to 0$ respectively, their values can be studied to approximately locate the position of the phase transition lines in the phase diagram.

What is already known, from numerical studies, about the thermal transition is that in the physical region for the masses of quarks[4] and for vanishing chemical potential it is not a true phase transition, but a rapid crossover, and it happens for $T_C = 150 - 170$ MeV [20]. Being a crossover the actual value for T_C is not uniquely definable, but generally depends on the observable used for its definition.

The sign problem prevents investigations at $\mu \gg 0$, so that our current knowledge about this region is based on models of QCD that only partially reproduce the full theory. The model calculations predict a first order transition at large μ. Consequently, a critical end point (CEP) is expected at the end of the first order line.

[4] for two degenerate light quarks plus the strange quark at their physical masses m_{ud} and m_s

Chapter 3

Numerical methods in lattice theories

> *"Any one who considers arithmetical methods of producing random digits is, of course, in a state of sin. For, as has been pointed out several times, there is no such thing as a random number - there are only methods to produce random numbers, and a strict arithmetic procedure of course is not such a method. [...] We are dealing with mere "cooking recipes" for making digits; probably they can not be justified, but should merely be judged by their results."*

John von Neumann, *Various techniques used in connection with random digits (1951)*

As we will see, the simulation of a certain theory requires the use of numerical techniques both for the generation of the lattice we have to put the theory on, together with the dof defined on it, and for the extraction of the expectation values of physical observables. Moreover, to all numerical estimates of these observables, corresponds a statistical error that has to be determined as well, by making use of statistical concepts implemented in a numerical way.

These are the topics to which this chapter is devoted. Our attention will be focused on the properties and implementation of some Monte Carlo algorithms with some specific examples (Secs. 3.1.1, 3.1.3, 3.1.2, 3.1.4). A discussion of the so-called *smoothing algorithms* will follow and, finally, we will address the statistical analysis of data and the determination of statistical errors affecting the numerical estimates of thermodynamic observables.

3.1 Monte Carlo methods and algorithms

When calculating the partition function Z for a statistical system, from which thermodynamic properties can be deduced, any time there is no exact analytic expression for Z, one is faced with the necessity of performing a sum over a quite often huge number of states (infinite in the thermodynamic limit). A statistical treatment of the theory is then feasible only thanks to the development of approximate techniques, mainly consisting of computational methods.

The employment of numerical methods, in its turn, requires a discretized and finite-size version of the model to be studied. In such a model Z becomes a numerically evaluable finite sum or a finite-dimensional integral.

In this context, a Monte Carlo (MC) method is a numerical technique for computing such sums/integrals and estimating properties of the system under study, by making use of some sequences of random numbers.

For the case of a single random variable the MC procedure can be implemented in three steps: the generation of a sequence on uniformly distributed random numbers $r_1, r_2, \ldots$, the production of a second sequence of random numbers $x_1, x_2, \ldots$ from the first one in a way that the new sequence has the distribution one wants to sample (importance sampling), and the estimation of the probability for a generic random x to take values in a specific region. It is clearly a way to effectively compute the definite integral of the distribution function. In multidimensional problems, over a generic region, this may be the only way to get the integral via vectors of random variables. The accuracy with which the integral is estimated depends, of course, on how wide the sample of our random numbers is, with an uncertainty behaving like $\mathcal{O}\left(1/\sqrt{N}\right)$ whatever the dimensionality of the system.

Behind the described procedure there is the assumption that the expectation value of some function $f(x)$, with regard to a probability distribution of density $\rho(x)$, can be approximated by an arithmetical average over a finite sets of values

$$\langle f \rangle_\rho = \frac{\int_a^b \mathrm{d}x \rho(x) f(x)}{\int_a^b \mathrm{d}x \rho(x)} = \lim_{N\to\infty} \frac{1}{N} \sum_{n=1}^{N} f(x_n) . \tag{3.1}$$

MC methods must then reside on the possibility of simulating the process of transition of the system among its possible states in such a way that the probability for the system to be in a given state after some steps of transition is equal, provided the equilibrium has been reached, to the weight of that state in the partition function for the real system i.e. to its Boltzmann weight. In this way the dof of our system will follow the

correct distribution and this is a peculiar property of the Markov processes. A stochastic sequence of N states is a Markov chain if the sequence is ergodic, aperiodic and if states are positive. Provided these three conditions hold, together with the sufficient condition called "detailed balance"[1], we are sure that for $N \to \infty$ a unique equilibrium distribution exists being a fixed point of the Markov process. If, once the equilibrium has been reached, we compute the average of a generic observable over a sufficiently long range of computer time, i.e over a sufficiently long sequence of equilibrium states, we will get a good estimate of the ensemble average for that observable [6, 13, 14, 21–25].

The design of a MC algorithm basically consists in identifying the correct Markov process, i.e. the correct set of transition probabilities between successive states of the system $P(\mu \to \nu)$, satisfying ergodicity and the detailed balance condition for the Boltzmann distribution. This may be a hard task, but there is some freedom to be exploited: first of all detailed balance condition only fixes the ratio $P(\mu\to\nu)/P(\nu\to\mu)$, secondly it is automatically satisfied for the trivial transition $\mu \to \mu$. The problem can then be rephrased by decomposing the transition probabilities into the product of a selection probability $g(\mu \to \nu)$ for our system to generate the state ν being fed the state ν, and an acceptance ratio $A(\mu \to \nu)$ that is the probability to accept the $\mu \to \nu$ transition rather than reject it. There is, this way, complete freedom on how to choice selection probabilities, while acceptance ratios have to be tuned for the detailed balance condition to hold. Of course the higher the acceptance ratios, the better to speed up the algorithm.

The strategy to be followed is the following:

- Given the initial state μ, a candidate state ν is proposed that differs from the initial state by the change of some local variable (es. spin flip on sites, change of links). The state ν is chosen according to a selection probability $g(\mu \to \nu)$ with the requirement that it satisfies ergodicity;
- The acceptance probability for the transition $\mu \to \nu$ is chosen with the requirement to fulfill the detailed balance condition and the state of the system is updated to ν or stays μ accordingly.

Different MC methods are simply different recipes on: how to select dof to be changed on the lattices (local or not), how to choice selection probabilities and acceptance ratios depending on the specific system under study.

Historically, modern Monte Carlo methods have their birth in the 1940s thanks to the studies of Fermi, Ulam, von Neumann, Metropolis et al.

[1] If we indicate by μ and ν, two generic states of our system that are connected by a transition in the Markov chain, the detailed balance condition is $e^{-\beta E_\mu} P(\mu \to \nu) = e^{-\beta E_\nu} P(\nu \to \mu)$.

3.1.1 Metropolis algorithm

The first example of thermal importance sampling method has been introduced by Nicolas Metropolis and his co-workers in their paper on hard sphere gases, dating back to 1953 [26], where they proposed an algorithm, known by then as Metropolis algorithm and being by then the most widely used among the MC algorithms.

The "Metropolis recipe" is the following:

- Update a single variable at a time (single-spin flip, single-link update);
- Equal selection probability of $1/N$ for all the N states accessible in the updating procedure (as many as spins/links);
- Acceptance ratios, fulfilling detailed balance

$$A(\mu \to \nu) = \begin{cases} e^{-\beta(E_\nu - E_\mu)}, & \text{if } E_\nu - E_\mu > 0; \\ 1, & \text{otherwise.} \end{cases} \tag{3.2}$$

Being a local updating procedure, in order to achieve ergodicity one has to perform a so-called *sweep* over all variables (sites, or links) of the lattice.

Let us now briefly analyze the reasons behind these choices and their consequences. Local changes involving only one variable allows for transitions to states not too far within each other and this mimic the behavior of systems at thermal equilibrium for which energy fluctuations are so small that the system only visits a subset of its possible states in a narrow energy range. The acceptance ratios are maximized by the choice in Eq. (3.2). The consequence of this choice is that the transition to a new state of equal or lower energy is always accepted, but also transitions to states with higher energy are at a certain rate accepted and in this way the algorithm incorporates quantum fluctuations.

3.1.2 Overrelaxation

The method called overrelaxation may be thought of as just a particular way of choosing the candidate variable for updates, within a Metropolis-like algorithm. It, indeed, exploits the fact that Metropolis accept-reject step always allows transitions to states of equal energy. Then one can change a single variable as much as possible, provided that a new one with the same probability weight is selected, and speed up the motion of the system in its configuration space.

A remark is in order, about the non-ergodicity of the overrelaxation algorithm: it only samples subspaces of constant action within the configuration space, hence generating a microcanonical ensemble of states. This problem can, of course, be circumvented by interposing overrelaxation steps between some ergodic updating procedure.

Overrelaxation is quite easy to be implemented for gauge field theories as $U(1)$ and $SU(2)$ and can also be implemented for $SU(3)$ [27].

3.1.3 Heat-bath algorithm

The heat bath Monte Carlo algorithm (Yang, 1963) owes its name to the fact that it is based on the idea of regarding the computer just as if it was a heat bath which is successively put in contact with each variable to be updated on our lattice. The variable being updated, as a response to this contact, fluctuates thermally throughout the group manifold until, when the thermal source is removed, it is left in one of its allowed states with a probability given by the associated Boltzmann weight.

To better understand how it works, the "heat-bath recipe" is the following:

- Update a single variable at a time (single-spin flip, single-link update);
- Selection probability for the $\mu \to \nu$ transition given by the canonical equilibrium distribution for the μ state of the system

$$g\left(\mu \to \nu\right) = \frac{e^{-\beta E_\mu}}{Z}, \tag{3.3}$$

  so that detailed balance condition is automatically fulfilled;
- Acceptance ratios $A\left(\mu \to \nu\right) = 1$ as a consequence: variable always change!

The numerical task in the implementation of the heat bath is to generate the desired distribution out of a sequence of uniformly distributed random numbers.

For some well behaved distributions this can be done via transformation method by computing and inverting the cumulative distribution function corresponding to our target distribution. However, in many practical applications for which it is too difficult to do so analytically, a useful alternative is von Neumann's acceptance-rejection technique [28]. Basically, for a real valued variable to be updated according to a $1D$ probability distribution function (p.d.f.), one just identifies a curve, $g\left(x\right)$, enclosing the desired p.d.f. for which the transformation method is easily applicable (the step function, at worst, may do the job). After the generation of a random number distributed according to $g\left(x\right)$ (our

selection probability), to satisfy detailed balance, one has to perform an accept-reject step via the generation of a second random number uniformly in $[0, g(x)]$ and accept x in case this second number lies below the p.d.f. value for x.

Implementing heat bath for gauge field theories is an involved task: while one can design an algorithm directly producing $SU(2)$ variables, this is not the case for $SU(3)$ where one has to apply a pseudo heat-bath method by iteratively performing the heat bath on the $SU(2)$ subgroups of $SU(3)$ [29].

3.1.4 HMC algorithm

QCD with fermions is an interacting fermion-boson quantum field theory, but it can be simulated in terms of bosonic variables alone, after having performed the Gaussian integrals over the fermion variables. Integration is mandatory if we want to apply the algorithmic ideas just introduced that cannot be directly applied to Grassman numbers.

A relevant problem affecting fermion-boson interacting theories, however, is that the effective bosonic action is non-local and this implies that if we try to apply single-link Metropolis update, the simulation would be really slow since we would have to evaluate the determinant of the fermion matrix many times. The algorithmic cost would, moreover, not decrease considering global updates because of very low acceptance rates.

Classical dynamics algorithms (based on discretized differential equations) are a solution to this problem because they allow changes of all variables in every updating step, with the number of necessary quark matrix inversions not depending on the number of links being changed and the acceptance rate not becoming too small. Such algorithms were proposed for pure gauge field theory by Callaway and Rahman [30] and later on used for fermionic quantum field theories as suggested by Polonyi and Wyld [31].

Basically, one uses the fact that the Euclidean path integral associated with a quantum theory can be rewritten as the partition function for a classical statistical mechanical system in four spatial dimensions with a canonical Hamiltonian governing the dynamics in the simulation time. This makes the expectation values of observables computable (in the thermodynamic limit) in terms of microcanonical ensemble averages at fixed energy. Ergodicity then allows us to approximate these ensemble averages by simulation-time averages over sufficiently long "classical" trajectories[2].

Clearly an exact solution to the so-called *molecular dynamics* (MD) equations of motion would produce a time series of configurations all belonging to the same equal-energy

[2]By "classical" trajectory here one means a sequence in simulation time of configurations generated by iterating the discretized version of classical dynamics equations corresponding to the Hamiltonian.

hypersurface and, in a Monte Carlo simulation all such candidate configurations would be accepted, but the equations of motion have to be discretized and solved numerically, so that the value of the Hamiltonian on the new configuration is just close (not equal) to its value on the starting configuration. Either an extrapolation to vanishing discrete step size, or a Metropolis accept-reject step against the known exact probability weight of the configuration, are then needed to avoid the propagation of numerical errors.

To move to the actual implementation of the *hybrid Monte Carlo* algorithm, we consider lattice QCD with two degenerate flavors of quarks in the Wilson formulation (see Sec. 2.2.3). The lattice action is given by:

$$S\left[U,\phi\right]=S_g\left[U\right]+\sum_{n,m\in\Lambda}\left(\phi_n^\dagger\left[DD^\dagger\right]^{-1}_{nm}\phi_m\right)\equiv S_g\left[U\right]+\left(\phi^\dagger\left[DD^\dagger\right]^{-1}\phi\right), \tag{3.4}$$

where with ϕ we indicate the pseudofermion fields introduced to rewrite the fermionic determinant [3] [32]. As outlined above, the strategy is to introduce conjugate momenta for our field variables in order to build the Hamiltonian that will govern the updating process. With π_n conjugate momenta for ϕ_n fields (both complex valued spinors at fixed flavor) and $P_{n\mu i}$ real momentum variables conjugate to the parameters $\omega_{n\mu i}$ appearing in the exponential map for the gauge fields $U_{n,\mu}\in SU(3)$, the Hamiltonian takes the form

$$H[P,\pi,U,\phi]=\frac{1}{2}\sum_{n,\mu,j}P^2_{n\mu j}+\frac{1}{2}\sum_n\pi_n^\dagger\pi_n+S\left[U,\phi\right], \tag{3.5}$$

with the j-index in the sum over $P^2_{n\mu j}$ running on the eight components of $P_{n\mu}$ as an element of $\mathcal{L}SU(3)$. In this context the lattice action acts like a potential and our expectation values can be calculated in this extended path integral representation as

$$\langle O\rangle=\frac{\int\mathcal{D}P\mathcal{D}U\mathcal{D}\pi\mathcal{D}\pi^\dagger\mathcal{D}\phi\mathcal{D}\phi^\dagger\;O\left[U,\phi\right]e^{-H[P,\pi,U,\phi]}}{\int\mathcal{D}P\mathcal{D}U\mathcal{D}\pi\mathcal{D}\pi^\dagger\mathcal{D}\phi\mathcal{D}\phi^\dagger\;e^{-H[P,\pi,U,\phi]}}. \tag{3.6}$$

By solving numerically the Hamilton equations in the simulation time governed by $H[P,\pi,U,\phi]$ in terms of $U_{n\mu}(\tau)$, we will sample an almost-microcanonical subset of configurations. Ergodicity and canonical-microcanonical equivalence tell us that $\langle O\rangle$ can be obtained as time-average over sufficiently long configuration-trajectories.

In the HMC algorithm the fields that are updated in a MD trajectory are the gauge fields U. For the MD evolution, some appropriate integration scheme as to be adopted, for instance the leapfrog or second order minimal (2MN) scheme [33].

Performing the integration process is not enough since ergodicity must be ensured, and this is done in the *hybrid algorithm* by combining the classical dynamics algorithm with

[3] Flavor, color and spinor indices are not displayed.

the stochastic Langevin approach as suggested by Duane [34]: Gaussian-distributed conjugate momenta are generated randomly at the beginning of every MD trajectory.

Finally the problem of how to update the fermionic fields ϕ has to be addressed. One could use a MD update also for these variables, but, as a faster alternative, one can generate fermion fields configurations in terms of a new set of variables $\xi = \left(K^\dagger\right)^{-1}\phi$. By generating a complex vector ξ with Gaussian distribution $e^{-\xi^\dagger\xi}$ and calculating $\phi = K^\dagger\xi$, one obtains an ensemble of the fermionic fields ϕ distributed according to $e^{-\phi^\dagger\left(DD^\dagger\right)^{-1}\phi}$.

We are now in a position to summarize what has been discussed up to here in the "HMC recipe":

- Update all variables at a time;
- Selection probability according to the MD integration process that takes as input Gaussian-distributed conjugate momenta and pseudofermion fields (to ensure ergodicity);
- Acceptance ratios tuned to fulfill detailed balance condition

$$A\left(U,\phi\to U'\phi'\right) = \begin{cases} e^{-(H[P',\pi',U',\phi']-H[P,\pi,U,\phi])}, & \text{if } H\left[P',\pi',U',\phi'\right] > H\left[P,\pi,U,\phi\right]; \\ 1, & \text{otherwise.} \end{cases} \tag{3.7}$$

Here

$$\begin{aligned} &H\left[P',\pi',U',\phi'\right] - H\left[P,\pi,U,\phi\right] \\ &= \mathrm{tr}\left[P^2\right] - \mathrm{tr}\left[P'^2\right] + S_G\left[U\right] - S_G\left[U'\right] + \phi^\dagger\left(\left(DD^\dagger\right)^{-1} - \left(D'D'^\dagger\right)^{-1}\right)\phi. \end{aligned} \tag{3.8}$$

The hybrid Monte Carlo algorithm implemented as described above has the advantage of being fast in exploring the configuration space while allowing for high acceptance rates if the accuracy of the MD is well tuned through the choice of the time step. Fixed the "temporal length" of the HMC trajectory, it has been proven to be advantageous to use a multiple timescales approach [35] consisting in the choice of different number of integration steps (i.e. different step sizes) for the different contributions to the action requiring higher accuracy for the cheaper contributions.

What slows down the algorithm is the necessity to compute the vector $\left(D'D'^\dagger\right)^{-1}\phi$ while integrating MD equations. This can be done by the iterative procedure called *conjugate gradient* method for the solution of the system $\left(D'D'^\dagger\right)x = \phi$. It is a Krylov space based method for which convergence is ensured after N steps for a $N\times N$ real, symmetric,

positive definite matrix. Depending on the requested accuracy, sometimes much fewer steps are necessary.

3.2 Smoothing methods: the smearing procedure

Being, generally, interested in the behavior of long distance correlators and in physical signals produced by stable or metastable configurations on our lattice, we are faced with the problem that these signals are washed out by the quantum short-distance fluctuations typical of the gauge field.

Smoothing methods have been designed with the exact purpose of locally suppressing UV fluctuations to disentangle the signal from the noise, so that one can carry out reliable measurements with a relatively small statistics. Here, we focus our attention on some smearing techniques that have been used in our studies.

Smearing a configuration basically means replacing each link variable by a linear combination of itself and a local average of products of other links along specific paths (commonly staples) connecting the endpoints of the link being smeared. The local average and the original link are assigned a specific weight in the combination that produces what is called a fat link. Fat links are then used in the construction of operators/correlators to be measured. Such a procedure can be iterated.

Thanks to the smearing techniques the ground state overlap is enhanced while contaminations due to excited states are more and more suppressed. One must, nevertheless, take into account that through subsequent iterations smearing involves links over increasingly larger distances and physical signals may be affected. Moreover, smearing leads out of the gauge group $SU(3)$ we are dealing with, and in both the variants of smearing that will be introduced in what follows a projection of the link variable back to $SU(3)$ is implemented.

3.2.1 APE smearing

Already introduced in the late eighties [36], the APE smearing techniques consists in the substitution of a link variable by a weighted combination of itself and products of links over $2(D-2)+2$ perpendicular staples (D is the dimension of the lattice) connecting its endpoints. On a 4D lattice this means:

$$\tilde{U}_\mu(x) = (1-\alpha)U_\mu(x) + \frac{\alpha}{6}\sum_{\mu\neq\nu} C_{\mu\nu}(x), \tag{3.9}$$

where

$$C_{\mu\nu}(x) = U_\nu(x)U_\mu(x+\hat{\nu})U_\nu^\dagger(x+\hat{\mu}) \quad (3.10)$$

$$+ \; U_\nu^\dagger(x-\hat{\nu})U_\mu(x-\hat{\nu})U_\nu(x-\hat{\nu}+\hat{\mu}). \quad (3.11)$$

The parameter α represent the smearing fraction and is the one to be tuned, together with the number of iterations of the procedure. The algorithm is implemented in two steps:

- The combination in Eq. (3.9) is computed;
- The link variable $\tilde{U}_\mu(x)$ is reunitarized by a projection to $SU(3)$ which is done by maximizing the quantity $\mathrm{Re}\,\mathrm{tr}\left[X\tilde{U}_\mu(x)^\dagger\right]$ for $X \in SU(3)$: then we have that $X = U'_\mu(x) = \mathcal{P}_{SU(3)}[\tilde{U}_\mu(x)]$.

Performing this transformation over all links in our lattice defines an APE smearing sweep to be, possibly, iterated. Studies measuring the average plaquette and the distribution of the smallest plaquette, as indicators of the quality of smearing, show that the single APE-smearing step is optimal for $\alpha = 0.75$

3.2.2 HYP smearing

Also in the case of HYP smearing [37] gauge configurations are smoothed through the substitution of links by linear combination of themselves and a path of "neighboring" links, but with these paths lying within a hypercube containing the original link. The fact that links beyond the hypercube are not involved in the smearing procedure ensures a minimal distortion even of the short distance properties of configurations. On a 4D lattice the fat HYP-links are built in a three steps procedure that we illustrate backwards:

- The final HYP-smeared link is constructed via projected APE blocking out of already fattened links

$$U'_\mu(x) = \mathcal{P}_{SU(3)}[(1-\alpha_1)U_\mu(x) + \frac{\alpha_2}{6}\sum_{\pm\nu\neq\mu}\tilde{U}_{\nu;\mu}(x)\tilde{U}_{\mu;\nu}(x+\hat{\nu})\tilde{U}^\dagger_{\nu;\mu}(x+\hat{\mu}))]; \quad (3.12)$$

- The intermediate step is another projected APE blocking out of already fattened links, but only staples in four (out of six possible) directions are involved

$$\tilde{U}_{\mu;\nu}(x) = \mathcal{P}_{SU(3)}[(1-\alpha_2)U_\mu(x) + \frac{\alpha_2}{4}\sum_{\pm\rho\neq\nu,\mu}\bar{U}_{\rho;\nu,\mu}(x)\bar{U}_{\mu;\rho,\nu}(x+\hat{\rho})\bar{U}^\dagger_{\rho;\nu,\mu}(x+\hat{\mu}))]; \quad (3.13)$$

- The initial step is a projected APE blocking out of links of the original configuration, but only two staples in a given direction are used

$$\bar{U}_{\mu;\nu\rho}(x) = \mathcal{P}_{SU(3)}[(1-\alpha_3)U_\mu(x) + \frac{\alpha_3}{2}\sum_{\pm\eta\neq\rho,\nu,\mu} U_\eta(x)U_\mu(x+\hat{\eta})U_\eta^\dagger(x+\hat{\mu}))]; \quad (3.14)$$

In all steps $U_\mu(x)$ is the original thin links and the directions indicated in subscripts after the colon symbol indicate that the corresponding links are not "decorated" with staples extending in that direction. Also in the case of HYP smearing a way to optimize the set of three smearing parameters $(\alpha_1, \alpha_2, \alpha_3)$ is to check which combination of them produces an approximate maximization of the average plaquette (or maximal shift in the distribution of smallest plaquette) and this yields ($\alpha_1 = 0.75$, $\alpha_2 = 0.60$, $\alpha_3 = 0.30$) as the optimal choice. One can similarly tune the three parameters by requiring approximate minimization of the noise-to-signal ratio of the static-light pseudoscalar corelation function and this leads to the choice ($\alpha_1 = 1.00$, $\alpha_2 = 1.00$, $\alpha_3 = 0.50$).

3.3 Statistical analysis of data

The result of our lattice simulation is a sample of measurements $\{o_1, o_2, \ldots, o_N\}$ of a given observable taken over a subset of states in the canonical ensemble of possible states for our system.

To proceed to the purpose of quoting a final result for our observable, a statistical treatment of lattice data is necessary in order to extract the best estimate of it, out of our data, and the corresponding statistical error. The assumption is that our measured quantities are random variables that are normally distributed around the true value $\langle O \rangle$, with variance σ_O^2. Suppose we are extracting our observable out of N measurements: as an unbiased estimator for the mean we just take the sample average $\hat{O}$ and the corresponding statistical error will be the standard deviation of the mean $\sigma_{\hat{O}} = \frac{1}{\sqrt{N}}\sigma_O$. At least, what just stated would be correct, and the statistical error would decrease as $1/\sqrt{N}$ if our N measurements were uncorrelated, which is not the case, unfortunately.

Our sample is, indeed, the series of measurements extracted on the i-th step of a Markov process: autocorrelation between measurements can not be neglected, rather has to be correctly estimated in terms of the autocorrelation function defined, at equilibrium, as

$$\Gamma_O(t) \equiv \frac{\langle (O_i - \langle O_i \rangle)(O_{i+t} - \langle O_{i+t} \rangle) \rangle}{\sigma_O^2}. \quad (3.15)$$

The estimator for the variance of our data can then be computed to be, up to some approximation,

$$\sigma^2_{\hat{O}} = \frac{\sigma^2_O}{N} 2\,\tau_{O,int} \quad \text{where} \quad \tau_{O,int} = \frac{1}{2} + \sum_{t=1}^{N} \Gamma_O(t)\,, \tag{3.16}$$

and it is a factor $2\,\tau_{O,int}$ bigger than the variance for a sample of the same number of uncorrelated measurements. Rephrased, this means that our statistics is effectively decreased by the same factor, leaving us with just $N/2\,\tau_{O,int}$ uncorrelated data. The quantity $\tau_{O,int}$ can be computed as described in [38, 39], but as an alternative our sample of autocorrelated data can be reduced to a sample of uncorrelated via data-blocking methods.

The sample is split into sub-samples of a size M that can be tuned by looking for a plateau in the dependence of σ_O on it. The presence of such a plateau is the hint that the standard deviation starts to show the $1/\sqrt{M}$ behavior expected for uncorrelated samples. In combination with blocking the jackknife method can be used for the error analysis. It consists in computing the averages over subsamples

$$\hat{o}_i = \frac{1}{M} \sum_{j=(i-1)M+1}^{iM} o_i, \quad \text{with} \quad 1 < i < n = N/M \tag{3.17}$$

and the so-called *partial jackknife averages* over the all-but-one subsample averages

$$\hat{o}^J_i = \frac{1}{n-1} \sum_{j \neq 1} \hat{o}_i, \tag{3.18}$$

because these are the ingredients to compute the unbiased jackknife estimate of the observable

$$O^{JK} = n\hat{O} - \frac{n-1}{n} \sum_{i=1}^{n} \hat{o}^J_i, \tag{3.19}$$

and its variance

$$\sigma^2_O = (n-1) \left[\frac{1}{n} \sum_{i=1}^{n} \left(\hat{o}^J_i - \hat{o}^J_i \right)^2 \right]. \tag{3.20}$$

Further details on the analysis of lattice simulation data can be found in textbooks [13, 14, 21].

Chapter 4

Numerical study of the confinement phenomenon

The color confinement phenomenon accounts for our inability to detect colored particles in nature, with the QCD spectrum consisting in color singlets particle states only. Whereas the mechanism producing such a phenomenon has not been explained from first principles yet, color confinement can be interpreted within a few possible scenarios. Lattice QCD numerical studies are then relevant in order to verify/disprove the validity of the proposed models.

The picture for confinement that is discussed in this work is the *dual superconductor model*.

It was conceived, by 't Hooft [40] and Mandelstam [41], that the vacuum of QCD could be modeled as a coherent state of color magnetic monopoles, called *dual superconductor* since the condensation of color *magnetic monopoles* in the QCD vacuum is thought to be analogous to the formation of *Cooper pairs* in the BCS theory of superconductivity. A dual superconductor is basically a superconductor in which the roles of the electric and magnetic fields are exchanged. The analogy is suggested both by the the absence of free quarks, and by the fact that meson resonances lie approximately on Regge trajectories indicating that a quark-antiquark pair is connected by a string [42], with a constant string tension i.e. an energy that increases linearly with the distance R between the color charges (*linearly confining pontential*). The non-perturbative dynamics at large distances must then squeeze the chromoelectric and chromomagnetic fields giving rise to color-field flux tubes connecting the two charges and being the footprint of color confinement [43, 44].

On a qualitative ground the formation of color flux tubes can, then, be interpreted as the dual analog of the Meissner effect in an ordinary superconductor. In a normal medium, the chromoelectric field would be described by a Coulomb potential, the energy of the system would vary, with the charge q and distance R, as $-q^2/R$ and field lines would spread out radially while connecting the two charges.

In a dual superconductor, instead, the Meissner effect attempts to eliminate the chromoelectric field. The vacuum, anyway, contains the color sources so that the Gauss law prevents the complete disappearance of the chromoelectric field. As a result a thin flux tube of color field lines connecting the quark and the antiquark is formed.

Although the mechanism for the dynamical formation of color magnetic monopoles is not explained yet, over the years, Monte Carlo simulations of lattice QCD, allowing a nonperturbative study of the chromoelectric fields between static quarks, have provided many evidences for the condensation of color magnetic charges in the QCD vacuum [45–50].

Moreover, again by MC simulations in lattice QCD, the tubelike distribution of color fields in presence of static quarks in the QCD vacuum has been studied nonperturbatively [51–67].

One of the research subjects addressed in this work is the study of quark confinement in $SU(3)$ pure gauge theory at zero and nonzero temperature. Special emphasis is put on the behavior of flux tubes across the deconfinement transition.

Before illustrating the results of numeric investigations in Sec. 4.5 and Sec. 4.6, a short description of the ordinary superconductivity will be given in Sec. 4.1, followed by an introduction on dual superconductivity in Sec. 4.2. Moreover, the numerical strategy in the study of flux tubes will be illustrated in Sec. 4.3, with particular reference to the implementation of the field-measuring procedure within the MILC code [1] discussed in Sec. 4.4 and Sec. 4.4.1.

4.1 Aspects of superconductivity

Here a short summary of a few aspects of the theory of superconductivity is given for later convenience. Much more detailed discussions can be found, for example, in [68, 69]. Superconductivity was discovered at the beginning of the twentieth century when H. K. Onnes, after having successfully liquefied helium, started to investigate resistivity of

[1] This work was in part based on the MILC collaboration's public lattice gauge theory code. See `http://physics.utah.edu/~detar/milc.html`

mercury at low temperatures. He found that the resistivity suddenly dropped to small values of the order of $\rho = 10^{-6}\Omega$, at 4.2K. A transition to a new state, which was called superconducting state, was then found to happen in many conductors under a certain critical temperature, below which zero electrical resistance is achieved. The aim of explaining this phenomenon from a theoretical point of view was pursued and achieved by Bardeen, Cooper and Schrieffer [70, 71] who developed a quantum mechanically based, microscopic theory named, after them, the BCS theory. However, the macroscopic behavior of superconductors had already been successfully described, to some extent, within the classical *London Model* [72] and through the *Ginzburg-Landau theory* (GL) for the conductor-superconductor phase transition in the context of the *macroscopic quantum model* for superconductors [73].

As concerns the macroscopic magnetic behavior of a superconductor, which is the feature that distinguish it from a perfect conductor, it has to do with the Meissner effect. Also in pure perfect superconductors, indeed, electrical resistance drops to minimal values at low temperature. The difference is that, while superconductors and perfect conductors react in exactly the same way, i.e. expelling the magnetic field, if they are cooled and then immersed in an external field, what changes in the two cases is that superconductors do not behave as classical electrodynamics predicts if they are first subjected to the application of an external magnetic field and then cooled under T_c.

In this situation, in which the material already has a constant magnetic field through it, when it is cooled trough the superconducting transition, the magnetic field would be expected to remain, due to the zero-resistance condition alone and according to the Ohm and Faraday's laws ($\vec{E} = \rho\vec{J}$ and $\nabla \times \vec{E} = -\partial\vec{B}/\partial t$ respectively). What happens, instead, is that a superconducting material, unlike a perfect conductor, has $\vec{B} = \mu_0 (H + M) = 0$ inside, because of the presence of persistent superficial electric currents also in this case, hence regardless of the order of the operations of cooling and application of an external constant field (superconductivity is a thermodynamic state). The Meissner effect is just this kind of magnetic screening effect with the expulsion of the magnetic field which is constrained outside the superconductor in the low-T nonzero-H case. The superconductor shows both zero resistivity and *perfect diamagnetism*: the magnetization totally cancels the external field inside the material. Unlike the diamagnetism of normal material caused by microscopic magnetic moments induced in the material by the external field, however, the magnetization of the superconductor is caused by macroscopic supercurrents flowing close to the surface of the specimen.

Screening currents flow in a thin surface layer. Indeed, according to London theory of superconductivity the magnetic flux density decays exponentially in the superconductor taking $1/e$ of its value at the surface at a distance λ which constitutes the so-called *London*

penetration depth. This result can be easily derived by use of the second London equation

$$-\vec{\nabla}\times\left(\frac{m_s}{n_s q_s^2}\vec{J}_s\right)=\vec{B}, \tag{4.1}$$

where the subscript s indicates that mass, density, charge and current refers to the superelectrons, later identified with the Cooper pairs in the BCS theory. In the case of a static and uniform $\vec{B}$ field, parallel to the surface of a semi-infinite superconductor, one gets

$$\vec{\nabla}^2\vec{B}=\frac{1}{\lambda^2}\vec{B}\quad\text{with}\quad\lambda=\sqrt{\frac{m_s}{n_s q_s^2}}. \tag{4.2}$$

The London penetration depth is found to be nearly independent of temperature at low temperatures. At temperatures of the order of about the 80% of the critical temperature T_c, instead, λ increases rapidly and approaches infinity as $T\to T_c$. The observed trend can be fitted well by the expression

$$\lambda(T)=\frac{\lambda(T=0)}{\sqrt{1-\left(\frac{T}{T_c}\right)^4}}. \tag{4.3}$$

So far, we have assumed that magnetic field is completely expelled, by supercurrents, in the surface of the superconductor. This is what happens in *type-I superconductors*, but there exists, instead, *type-II superconductors* in which magnetic field can somehow access the inside of the material.

For the type-I material in absence of demagnetization effects, the superconductivity breaks down above a critical value for the field H_c. For $H>H_c$, the external field completely penetrates the sample and the magnetization of the sample vanishes. For $H<H_c$, the material is superconducting and its magnetization exactly compensates the external field such that the inner of the material is field-free.

There exists, however, type-II superconductors. In this second case, two are the critical magnetic fields to be considered: the lower critical field H_{c1} and upper one H_{c2}. Below H_{c1} the material behaves exactly as a type-I superconductor. In Fig. 4.1 we show the H, T phase diagrams for the different cases of type-I and type-II superconductors. The magnetic fluxes begin to penetrate into the superconductor in a quantized form as soon as the applied field exceeds H_{c1} so that the superconductor is said to be in a mixed or Abrikosov state. When the applied field exceeds the value H_{c2}, instead, superconductivity is destroyed and the material comes back to its normal conducting state.

The sense of the word "mixed" resides on the fact that the whole material is divided into normal and superconducting regions. Magnetic flux tubes can, for $H_{c1}<H<H_{c2}$,

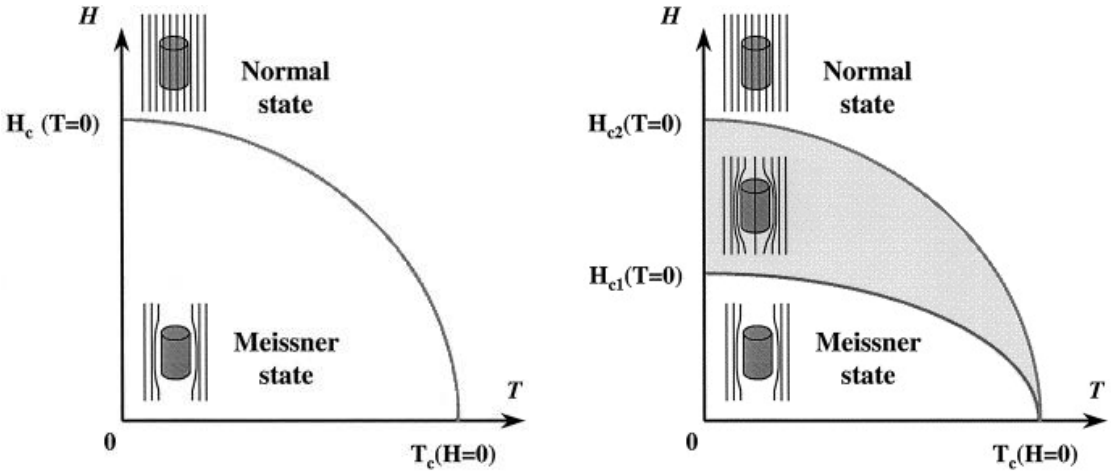

FIGURE 4.1: Phase diagrams for type-I and type-II superconductors (figures from [74]).

penetrate the material, but only in narrow flux tubes as shown in Fig. 4.2. This tubes are called *Abrikosov flux tubes* and their separation decreases with increasing external fields until the whole material is crossed by the field. The condition for the mixed state to be favored energetically is determined by the ratio of the London penetration length, to a new scale, the coherence length.

The coherence length, which is the second characteristic length scale of superconductivity appearing in the GL theory of superconductors, is a measure of the variation in space of the Cooper-pair (superelectron) density. The GL theory has been proposed as an extension of the London theory, based on the Landau theory for second order phase transitions, such that the condition of constant and uniform number density of superconducting carriers can be released. One of the assumptions behind GL theory is that the behavior of superelectrons can be described in terms of a *complex order parameter* $\psi = |\psi| e^{i\theta}$, which is a kind of "effective wave function" whose square amplitude is the superdensity $|\psi|^2 = n_s$. Moreover, it is assumed that the variation of free energy between normal (f_n) and superconducting (f_s) state, can be expanded in powers of the of the amplitude of the order parameter and of its gradient

$$f_s - f_n = \alpha |\psi|^2 + \frac{\beta}{2} |\psi|^4 + \gamma \left|\vec{\nabla}\psi\right|^2 + \dots . \tag{4.4}$$

The terms and phenomenological coefficients, α, β, γ, in this expansion are constrained by symmetry arguments and by the requirement of having a minimum for the free energy at some finite value for $|\psi|$. In a homogeneous superconductor and in absence of external magnetic field, the last term in Eq. (4.4) can be neglected and the two possibilities for the minima of free energy, see Fig. 4.3 are: $|\psi|^2 = 0$ for $\alpha > 0$, hence in the disordered normal state at $T > T_C$, and $|\psi|^2 = -\alpha/\beta$ for $\alpha < 0$, hence in the ordered superconductive phase at $T < T_C$.

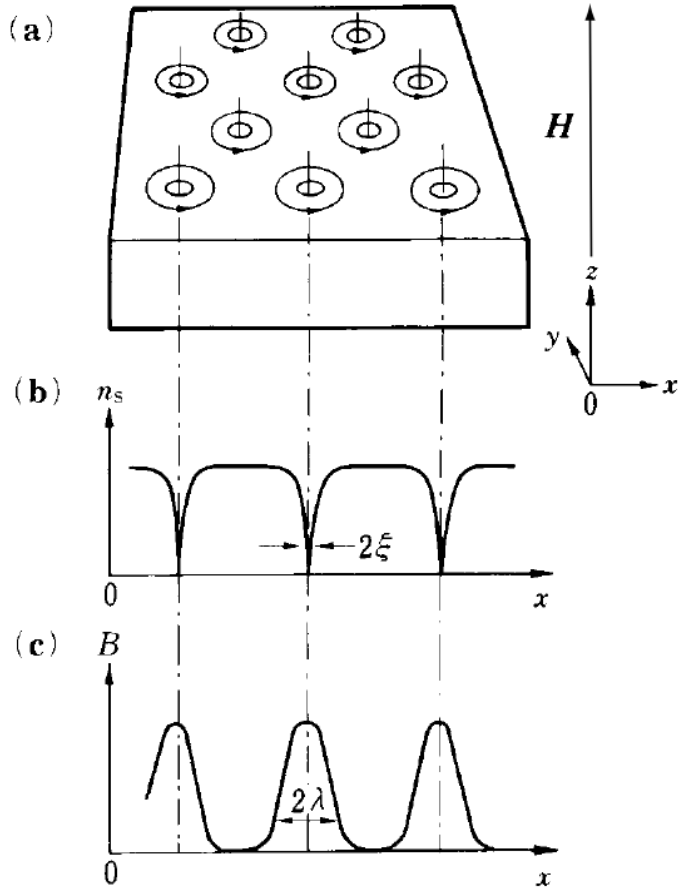

FIGURE 4.2: Schematic illustration of the mixed state in an ideal type-II superconductor. (a) Magnetic flux distribution penetrating into the superconductor. A circle with an arrow indicates the screening current flowing around a quantized flux line. The magnetic fluxes are distributed so as to form a close-packed regular triangular lattice. (b) Number density distribution of the superconducting electrons, where 2ξ represents the coherence length. (c) Magnetic flux density distribution, where 2λ represents the penetration depth. This illustration is taken from [75].

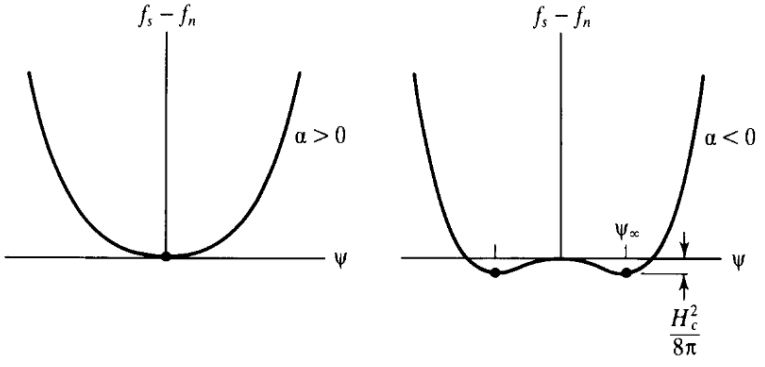

FIGURE 4.3: Ginzburg-Landau free-energy functions for $T > T_C$ $(\alpha > 0)$ and for $T < T_C$ $(\alpha < 0)$. Heavy dots indicate equilibrium positions. This illustration is taken from [68].

Following this kind of reasoning, it emerges that, for $\alpha < 0$, $f_s < f_n$ and the change of sign in α at $T = T_C$ (suggesting the validity of the expansion $\alpha(T) = \alpha_0 (T - T_C)$, with

$\alpha_0 > 0$) unveils a discontinuity in the specific heat that tells us the transition is at least second order.

The GL equations are derived, instead, for the case in which an external magnetic field is applied. The free energy expansion then takes the form

$$f_s - f_n = \alpha |\psi|^2 + \frac{\beta}{2} |\psi|^4 + \frac{1}{2m_s} \left| \left(-i\vec{\nabla} - e_s \vec{A} \right) \psi \right|^2 + \frac{\vec{B}^2}{2} .. \tag{4.5}$$

Through a minimization procedure of the free energy $\delta (f_s - f_n) = 0$ with respect to variations in the complex order parameter ψ, rather than in the vector potential $\vec{A}$, the two GL equations turn out to be

$$\alpha\psi + \beta |\psi|^2 \psi + \frac{1}{2m_s} \left(-i\vec{\nabla} - q_s \vec{A} \right)^2 \psi = 0 \tag{4.6}$$

$$\vec{J}_s = \frac{q_s}{2im_s} \left(\psi^* \vec{\nabla} \psi - \psi \vec{\nabla} \psi^* \right) - \frac{q_s^2}{m_s} |\psi|^2 \vec{A}. \tag{4.7}$$

The coherence length emerges from the first GL equation under the condition $\vec{A} = 0$

$$\xi^2 \vec{\nabla}^2 \tilde{\psi} + \tilde{\psi} - \tilde{\psi} \left| \tilde{\psi} \right|^2 = 0, \text{ with } \xi (T) = \frac{1}{\sqrt{2m_s |\alpha (T)|}}, \tag{4.8}$$

where $\tilde{\psi} = \psi / |\psi_0|$, with $|\psi_0|^2 = -\alpha/\beta$ ($\alpha < 0$). It measures the scale of distance of the variations of the order parameter in the superconductor.

Also the *London penetration depth* can be obtained within the GL theory since in the limit of weak applied field, by computing the curl of J_s the London equation is recovered with

$$\lambda (T) = \sqrt{\frac{m_s \beta}{q_s^2 |\alpha (T)|}}. \tag{4.9}$$

Both the length scales we have just introduced, $\lambda (T)$ and $\xi (T)$, are T-dependent quantities diverging towards the critical temperature as $(1 - T/T_C)^{-1/2}$, so that their ratio, i.e. the so-called *Ginzburg Landau parameter* $\kappa = \lambda / \xi$ is a T-independent quantity. Such a quantity characterizes the type of superconductivity according to the criterion:

$$\kappa < \frac{1}{\sqrt{2}} \longleftrightarrow \text{type I superconductors}$$
$$\kappa > \frac{1}{\sqrt{2}} \longleftrightarrow \text{type II superconductors}$$

for $\kappa \simeq \frac{1}{\sqrt{2}}$ the superconductor is in a mixed state consisting of the Meissner and mixed phase at the same time. The criterion is derived considering an infinite superconductive medium embedded in a uniform external field B^{ext}. Above a given threshold for B^{ext}

the medium becomes a normal conductor and $|\psi|^2 = 0$. One can imagine to gradually decrease the applied field until the nucleation of superconducting regions starts to occur. Then $|\psi| \simeq 0$ allows the linearization of the first GL equation (it takes the form of a Schrödinger equation for a particle subject to harmonic potential) to be solved for the highest possible field at which superconductivity appears. The critical field turns out to be

$$B_{c2} = \frac{2m_s\,|\alpha|}{|e_s|}, \tag{4.10}$$

and can be compared to the thermodynamic critical field

$$B_c = \sqrt{\frac{\alpha^2}{\beta}}, \tag{4.11}$$

defined as the maximum applied field from the relation $f_n - f_s = {}^{B_c^2}/_2$. By use of equations Eq. (4.8) and Eq. (4.9) one gets

$$B_{c2} = \frac{\kappa}{\sqrt{2}} B_c. \tag{4.12}$$

Finally, the linearization of GL equations is admitted also slightly below B_{c2}. Abrikosov wrote a general solution for the first GL equation also taking into account periodicity in a plane perpendicular to $\vec{B}$, hence predicting that the flux tubes formed in type-II superconductors are arranged in a regular array, with each tube carrying one quantized unit of magnetic flux $\phi_0 = {}^{hc}/_{2e}$, in CGS units, called fluxoid [76].

4.2 Aspects of dual superconductivity

To move to the dual analog of superconductivity and its connection to the description of the confinement mechanism in QCD, the superconductive behavior observed for solids has to be set within a field-theoretical context. It has been observed that, from a field-theoretical point of view, one can describe a phenomenon with the characteristics shown by the superconductivity phase transition as a Higgs phenomenon corresponding to a spontaneous symmetry breaking.

Moreover, the BCS theory assumes that the attractive force between electrons, that arises thanks to the electron-phonon interaction, determines the production of bound electron pairs (Cooper pairs) in which the individual electrons carry opposite spin. Then the fundamental state of these pairs can be seen as particles with zero spin and $2e$ charge and, in the theoretical background of the Higgs mechanism, can be seen as the analog of the excitations of an Higgs field.

This interpretation was pursued by 't Hooft who showed how, in QED (gauge group $U(1)$), the transition from a superconductive to a normal phase may be described as a spontaneous breaking of the gauge symmetry. Also for the case of QCD it is speculated that the vacuum can be described in terms of a Landau-Ginzburg model of a dual superconductor, also called dual Abelian Higgs model, and that a spontaneous symmetry breaking is involved in the deconfining phase transition.

Let us then explain the meaning of the adjective "dual" referred to superconductivity. A dual superconductor is a superconductor in which the roles of the electric and magnetic fields are exchanged. Whereas, in usual superconductors, electric charges are condensed in the form of Cooper pairs, in a dual superconductor, the condensed charges are the magnetic ones. A similar exchange in the roles of the field makes it natural to express the Lagrangian of the model in terms of the *dual* field tensor $\tilde{F}^{\mu\nu}$, which is obtained by the exchange

$$\vec{E} \to \vec{H}, \qquad \vec{H} \to -\vec{E}, \tag{4.13}$$

of the electric and magnetic fields.

On a qualitative ground, in a static quark-antiquark configuration in which the particles are separated by a distance R a static chromoelectric field is generated whose lines connecting the two charged particles cannot spread in space as if they would do in a non-superconducting medium. On the contrary, as the $q\bar{q}$ pair is embedded in a dual superconductor the chromoelectric field lines are compressed in a thin flux tube connecting the two sources by means of the dual Meissner effect. As already mentioned, the geometry of the flux tube ensures that the energy increases linearly with R creating a linearly confining potential between the quark and the antiquark.

The main goal in this work is to investigate the formation of chromoelectric flux tubes in the case of an $SU(3)$ pure gauge field theory, and analyze how some of their properties are affected by changes in temperature towards and above the critical value at which the deconfinement phase transition is expected to take place. This aim is pursued by studying the shape of chromoelectric longitudinal field in the transverse directions and then fit this shape with adequate functions based both on the London and on the Ginzburg-Landau description of superconductivity (in both cases tube-like structures arise as a solution of the equations relating electric, magnetic fields and the current in the superconductive medium).

Up to now, one of the things that has been discovered about flux tubes is that they are almost completely formed by the longitudinal chromoelectric field E_l, which is constant along the tube axis and decreases rapidly in the transverse direction that we denote by x_t. As for the transverse shape of E_l, many proposals were advanced over the years

about the function according to which a good fit could be obtained. In this work, we take into consideration two of these proposals.

The fact that the formation of the chromoelectric flux tubes can be interpreted as dual Meissner effect and the chromoelectric field distribution should resemble the dual version of the Abrikosov vortex field distribution led to the proposal [60–64] to fit the transverse shape of the longitudinal chromoelectric field according to

$$E_l\left(x_t\right) = \frac{\Phi}{2\pi}\mu^2 K_0\left(\mu x_t\right), \qquad x_t > 0. \tag{4.14}$$

In Eq. (4.14) K_0 is the modified Bessel function of order zero, Φ is the external flux and μ is the inverse of the London penetration length. The condition for $\lambda = {}^1\!/\!_\mu$ under which Eq. (4.14) holds, is that $\lambda \gg \xi$, where ξ is the above mentioned coherence length in the superconductivity theory that, within the dual superconductor model, measures the coherence of the magnetic monopole condensate. We deduce that a fit with Eq. (4.14) can be applied if we are dealing with a type-II dual superconductor. However, some lattice studies, e.g. [57], indicated that the vacuum behaves like an effective dual superconductor with $\kappa \sim 1$, hence belonging to the borderline between a type-I and type-II superconductor nearly invalidating the use of Eq. (4.14).

As a second possibility, in Ref. [77] it has been suggested a different fitting function by exploiting the results in Ref. [78]. There, from the assumption of a simple variational model for the magnitude of the normalized order parameter of an isolated vortex, analytic expressions for magnetic field and supercurrent density are derived, that solve the Ampere's law and the Ginzburg-Landau equations. By dual analogy

$$E_l\left(x_t\right) = \frac{\Phi}{2\pi}\frac{\mu^2}{\alpha}\frac{K_0\left[\left(\mu^2 x_t^2 + \alpha^2\right)^{1/2}\right]}{K_1\left[\alpha\right]}, \tag{4.15}$$

where μ has the same meaning as before and $\alpha = \xi_\nu/\lambda$ is the ratio of the penetration length to the variational core radius parameter. Realistic values of the fields in this second case are yielded also near the flux tube axis. Eq. (4.15) is equivalent to

$$E_l(x_t) = \frac{\phi}{2\pi}\frac{\mu^2}{\alpha}\frac{K_0[(\mu^2 x_t^2 + \alpha^2)^{1/2}]}{K_1[\alpha]}\,, \qquad \mu = \frac{1}{\lambda}\,, \quad \frac{1}{\alpha} = \frac{\lambda}{\xi_v}\,. \tag{4.16}$$

By fitting Eq. (4.16) to $E_l(x_t)$ data, one can extract both the penetration length λ and λ/ξ_v. The Ginzburg-Landau κ parameter can then be obtained by

$$\kappa = \frac{\lambda}{\xi} = \frac{\sqrt{2}}{\alpha}\left[1 - K_0^2(\alpha)/K_1^2(\alpha)\right]^{1/2}\,, \tag{4.17}$$

and, the coherence length ξ can be deduced. It has been shown in [79] that the two possible fitting functions for $E_l(x_t)$ can be traced back under different assumptions to either the London model or the Ginzburg-Landau theory for the ordinary superconductivity.

4.3 Observables and simulation setup

The spatial distribution of color fields produced by a pair of static sources, in $SU(3)$ pure gauge theory vacuum at zero and nonzero temperature has to be analyzed. We will only consider static sources living in the fundamental representation of $SU(3)$, for instance a quark and an antiquark. To measure the field, the correlation of a plaquette U_P with two Polyakov loops will be used, as a natural modification of the connected correlation of a plaquette with a Wilson loop, that has already been used in studies on the zero-temperature behavior of flux tubes. The most suitable lattice operator for the detection of flux tubes is given, in particular, by a connected correlation between the above-mentioned pairs of objects, in which the connection is realized by means of a Schwinger line L. A simplified structure for the used operators is shown in Fig. 4.4.

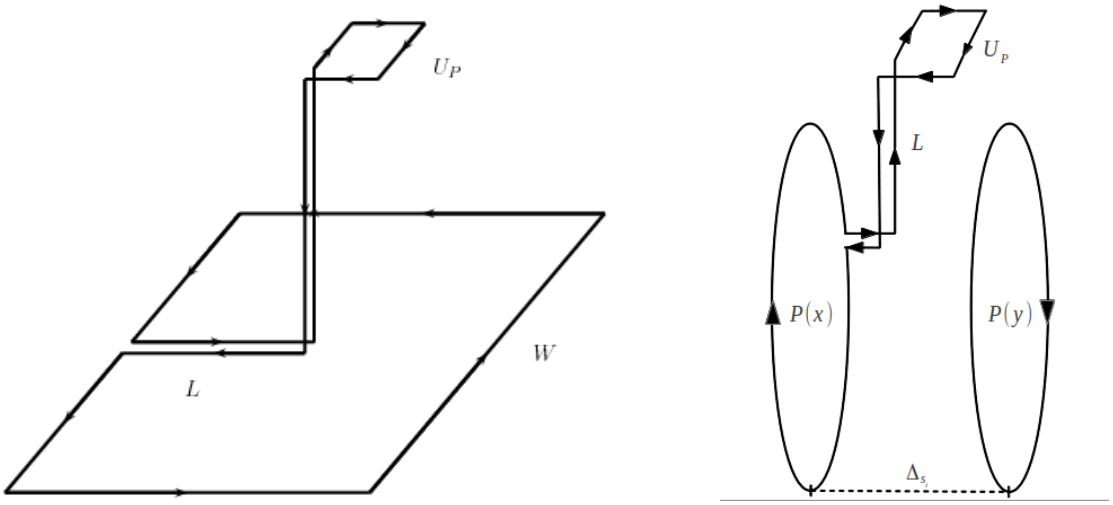

FIGURE 4.4: From the left to the right: the connected correlator between the plaquette U_P and the Wilson loop and the correlator between two Polyakov loops, one of which connected to a plaquette U_P. Connections are realized by Schwinger lines. The subtraction in Eq. (4.18) and Eq. (4.19) is not explicitly drawn.

The reason for the connection via Schwinger lines lies in the fact that the corresponding disconnected expressions are sensitive to the squared field and are much noisier.

It can, instead, be shown that the lattice connected correlators

$$\rho_W^{conn} = \frac{\left\langle \mathrm{tr}\left(WLU_PL^\dagger\right)\right\rangle}{\left\langle \mathrm{tr}\left(W\right)\right\rangle} - \frac{1}{N}\frac{\left\langle \mathrm{tr}\left(W\right)\mathrm{tr}\left(U_P\right)\right\rangle}{\left\langle \mathrm{tr}\left(W\right)\right\rangle}, \quad T=0 \tag{4.18}$$

$$\rho_P^{conn} = \frac{\left\langle \mathrm{tr}\left(P\left(n\right)LU_PL^\dagger\right)\mathrm{tr}P\left(y\right)\right\rangle}{\left\langle \mathrm{tr}\left(P\left(n\right)\right)\mathrm{tr}\left(P\left(y\right)\right)\right\rangle} - \frac{1}{N}\frac{\left\langle \mathrm{tr}\left(P\left(n\right)\right)\mathrm{tr}\left(P\left(y\right)\right)\mathrm{tr}\left(U_P\right)\right\rangle}{\left\langle \mathrm{tr}\left(P\left(n\right)\right)\mathrm{tr}\left(P\left(y\right)\right)\right\rangle}, \quad T\neq 0, \tag{4.19}$$

by measuring the fields rather than their squares [56], fluctuate less and seem to be the natural operators for studying flux tubes. In the above formulas N is the number of colors, while $U_P = U_{\mu\nu}(n)$ is the plaquette in the (μ,ν) plane, connected to the Wilson loop W, or to the Polyakov loop P, by a Schwinger line L.

The linearity of ρ_W^{conn} and ρ_P^{conn} in the field, in the $SU(3)$ case holds up to terms of order a^2 in the lattice spacing[2]. The linear term in $F_{\mu\nu}$, then, dictates the dominant behavior of our correlators in the continuum limit. This becomes clear if one exploits the exponential map connecting any element of a Lie group to a vector in the corresponding Lie algebra. One simply has to expand the expressions for $\tilde{W} = L^\dagger W L$ and U_P as follows

$$\begin{aligned}
\mathrm{tr}\left\{\tilde{W}\left[U_P - \mathrm{tr}\left(\frac{U_P}{3}\right)\mathbb{1}\right]\right\} &= \mathrm{tr}\left\{\tilde{W}\left[e^{iga^2F^a_{\mu\nu}T^a} - \frac{1}{3}\mathrm{tr}\left(e^{iga^2F^a_{\mu\nu}T^a}\right)\mathbb{1}\right]\right\} \\
&\simeq \mathrm{tr}\left\{\tilde{W}\left[\mathbb{1} + iga^2F^a_{\mu\nu}T^a - \frac{g^2a^4}{2}F^a_{\mu\nu}T^aF^b_{\mu\nu}T^b + \right.\right. \\
&\left.\left. - \frac{1}{3}\mathrm{tr}\left(\mathbb{1} + iga^2F^a_{\mu\nu}T^a - \frac{g^2a^4}{2}F^a_{\mu\nu}T^aF^b_{\mu\nu}T^b\right)\right]\right\} = \\
&= \mathrm{tr}\left\{e^{in^aT^a}\left[iga^2F^a_{\mu\nu}T^a + \mathcal{O}\left(a^4\right)\right]\right\}.
\end{aligned} \tag{4.20}$$

A few remarks are in order, about the linearity of our lattice observable in the components of the field strength tensor. Those components are elements of the $\mathcal{L}SU(3)$ algebra, hence 8-vectors in color space, while our connected correlator is a gauge invariant quantity that, as such, is not sensitive to the underlying color structure of the field in the sense that it cannot single out and probe any given color component in the field structure. The Wilson/Polyakov loop connected to the plaquette is, indeed, the source of a color field which points, in average, onto an unknown direction (in color space) given by the loop itself (there is no preferred direction). What we measure is the average projection of the color field onto that direction, which is what has been indicated by n^a in Eq. (4.20). The color indices of the Schwinger lines are contracted with the loop which is the source of the field and realize the color parallel transport between the source loop and the plaquette position.

[2] In $SU(2)$, the linearity in the field is easier to show and holds in general. There, indeed, the plaquette can be written as a linear combination of the identity and the Pauli matrices σ^i: $U_P = U_P^0 + i\sigma^i U_P^i$. It becomes then clear that the quantity $\rho_W^{conn} = \left\langle \mathrm{tr}\left(WLi\sigma^iU_P^iL^\dagger\right)\right\rangle / \left\langle \mathrm{tr}(W)\right\rangle$, changes its sign under the transformation $U_P \to U_P^\dagger$.

Taken in mind the above considerations on the linearity, a symbolic expression for the naive continuum limit of the connected correlator in Eq. (4.19) is

$$\rho_W^{\text{conn}} \overset{a\to 0}{\longrightarrow} a^2 g \left[\left\langle n^a F^a_{\mu\nu} \right\rangle_{q\bar{q}} \right], \tag{4.21}$$

where $\langle \quad \rangle_{q\bar{q}}$ denotes the average of the field projection in the presence of a static $q\bar{q}$ pair and $\beta = {}^{2N}/_{g^2}$ is the coupling constant. The components of the field strength tensor can, then, be extracted as

$$F^a_{\mu\nu}(x)\, n^a = \sqrt{\frac{\beta}{2N}} \rho_W^{conn}(x)\,. \tag{4.22}$$

The same can be said about the ρ_P^{conn} correlator.

A numerical check of the linearity in the field of ρ_P^{conn} in the scaling region was also accomplished, by connecting the source loop to either the plaquette or its hermitian conjugate and comparing the measured field in the two cases. The result of such a test is shown in Fig. 4.5. As a last comment on the physical interpretation ρ_P^{conn}, we mention the analytical results in [80], where, through the derivation of the analog of the Gauss law for QCD, a prescription on how to calculate the field strength as a gauge invariant quantity in lattice simulation is given, that leads to Eq. (4.18).

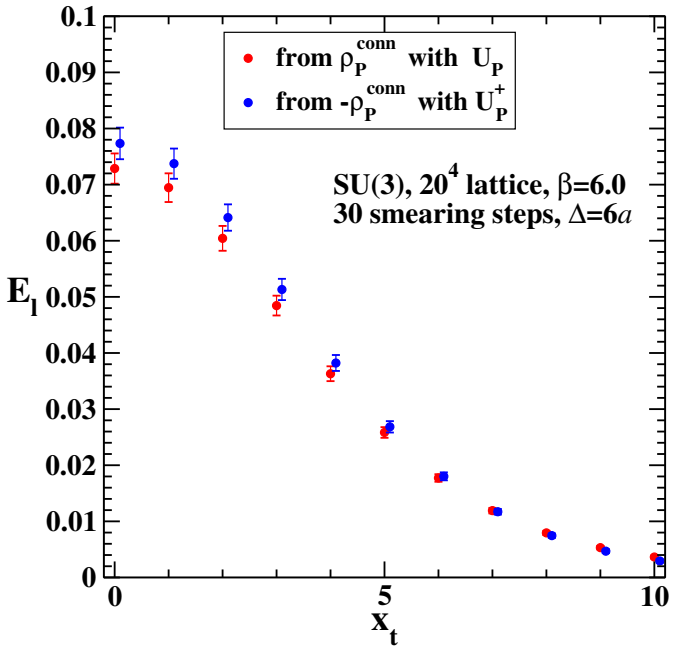

FIGURE 4.5: Longitudinal chromoelectric field for the two different orientations of the plaquette entering the definition of the connected correlator given in Eq. (4.19).

The way to probe the color field distribution of the flux tube and, in particular, the spatial dependence of color fields, in a direction that is perpendicular to the axis of the

flux tube joining the quark and anti-quark, is by varying the position and the orientation of the plaquette with respect to the loop.

Our final aim is to extend previous studies of the structure of flux tubes performed at zero temperature to the case of $SU(3)$ pure gauge theory at finite temperatures. The reason is that the nonperturbative investigation of flux tubes generated by static color sources at finite temperature is directly relevant to clarify the formation of $c\bar{c}$ and $b\bar{b}$ bound states in heavy ion collisions at high energies. To pursue this goal, the connected correlator in Eq. (4.19) has to be employed rather than the correlator involving the Wilson loop.

Moreover a smoothing procedure is necessary in order to enhance the signal-to-noise ratio through a suppression of lattice artifacts at the scale of the cutoff. At $T \neq 0$, an important restriction on how to implement smoothing is that thermal fluctuations must be preserved. To achieve this result, smearing techniques [36, 37] have been used. The way smearing is implemented can, indeed, be easily specialized to links different directions. Hence, a single HYP smearing step is realized on links in the temporal direction (which is the relevant direction for thermal fluctuations), while tens of space-only (3D) APE smearing steps are realized in the spatial directions.

The strategy is to preliminarily check that results at $T = 0$, employing $\rho_P^{conn}(x)$ and smearing, are consistent with previous studies obtained with Wilson loops and cooling [77].

4.4 Flux tubes studies within the MILC software

Investigations in lattice QCD are computationally intensive tasks: they require an as efficient as possible numerical implementation. In some cases the results of the efforts spent, within the lattice community, in making numerical computations more and more efficient have been made available. Quoting its manual, "The MILC Code is a body of high performance research software written in C for doing $SU(3)$ lattice gauge theory on several different (MIMD) parallel computers in current use. In scalar mode, it runs on a variety of workstations making it extremely versatile for both production and exploratory applications". It is developed by the MIMD Lattice Computation (MILC) collaboration.

Admittedly, pure gauge is not the most intensive theory to be simulated, but in view of future developments and in order to exploit parallelization to speed up simulations, the choice has been made, to implement all measurements described in Sec. 4.3 within the MILC Code. Therefore, while the zero-temperature results shown in this work have been

obtained through a serial fortran code, the finite-temperature study is entirely carried out by use of a MILC Code application, which has been written on purpose.

The MILC "pure_gauge" application simulates the unimproved pure gauge theory, using microcanonical over-relaxed and quasi-heat bath algorithms. By admission of the same MILC manual, "not much is measured" within this application, except for plaquette and Polyakov loop measurements, possibly in a chosen gauge, or without gauge fixing. However, "pure_gauge" application is the most suited ground for the implementation of flux tube measurements. A new application, called "flux_tubes", was then created. It shares all the updating algorithms with the pure gauge application, but no gauge fixing is available, since it is not needed for our purpose, while APE and HYP smearing have been made available and many different targets were created for flux-tube measurements. The list of all targets is the following:

- *su3_ora_wilson* implements Wilson connected correlator and isotropic ($4D$ APE) smearing (suited for $T = 0$ studies);
- *su3_ora_wilson_anisotropic_smearing* implements Wilson connected correlator and anisotropic ($3D$ APE) smearing (suited for $T \neq 0$ studies in the chromomagnetic sector);
- *su3_ora_polyakov* implements Polyakov connected correlator and isotropic ($4D$ APE) smearing (suited for $T = 0$ studies);
- *su3_ora_polyakov_nonzeroT* implements Polyakov connected correlator and anisotropic ($3D$ APE and temporal HYP) smearing (suited for $T \neq 0$ studies).

All of the targets use overrelaxed/quasi heat bath algorithm for configurations updating.

4.4.1 Aspects of the implementation

The code we used in this work has three main duties: it generates and, step by step, updates the configuration of fields over all links in the lattice, it iteratively smears the gauge configuration and alternates to smearing the computation of the observable values, which are the output we need for our statistical analysis.

As for the first above mentioned duty, Cabibbo-Marinari heat bath algorithm and over-relaxation algorithm in a ratio of 1 : 4 steps are used. Thermalization is achieved by avoiding the use, for the measuring process, of a sequence of 10K configurations until the system has lost memory of the starting configuration. Ten decorrelation updating steps are also realized between two subsequent measurements.

As already mentioned, the smearing procedure is implemented differently, depending on the specific target being run.

In the construction, on the lattice, of the connected correlators (see Fig. 4.4) the lattice symmetry is always exploited to build as many copies of the correlator as possible, for each smeared configuration. At finite temperature ($N_T \ll N_S$), the temporal direction is fixed as the one around which the Polyakov loops in Eq. (4.19) wind around. $P(x)$ and $P(y)$ are separated by a distance, denoted as Δ_{S_i} in Fig. 4.4, in any of the three spatial directions (1,2,3), for instance 1. The Schwinger line L is then displaced in that direction until it reaches the center between the two loops. To allow measurements of the field at finite distances from the axis connecting the two loops in transverse direction 1, the Scwhwinger line must be lengthened in any of the remaining two spatial directions, say 2. The maximum displacement considered in this direction was of $10a$. The field has sometimes been measured also at non-integer distances from the axis, by extending the Schwinger line in the last available spatial direction, that is 3 (over a distance of $1, 2a$). Any permutation of (1,2,3) is considered to increase statistics. Moreover, when the Schwinger line is extended to the third (and possibly fourth) direction, we average over positive or negative displacements on that direction, exploiting, in this way, the cylindrical symmetry of the flux tube. Until now we have considered the length of the Schwinger line that tells us at what distance we are measuring the field. What is the component of the field strength tensor that we are measuring depends, instead, on the orientation of the plaquette connected to the Schwinger lines.

Analogous considerations can be made in the zero-temperature, $N_T = N_S$ case, unless that the symmetry of the lattice is extended to the fourth direction, can be exploited to produce a bigger number of copies of our correlators.

As for our studies in the chromomagnetic sector, we have less freedom in the possible orientations of the Wilson connected correlator in Eq. (4.18) since the correlator is built in the spatial sublattice with links in the temporal direction excluded from the construction.

4.5 Flux tubes in $SU(3)$ at zero temperature

What follows is based on [81, 82].

Numerical simulations were performed on 20^4 lattices using the Wilson action with periodic boundary conditions and the Cabibbo-Marinari algorithm [29] combined with overrelaxation on $SU(2)$ subgroups to update the configurations. We considered Polyakov lines separated by $\Delta = 4a, 6a, 8a$ (where a is the lattice spacing) for four different values

of the gauge coupling β in the range $5.9 \div 6.1$. In order to reduce the autocorrelation time, measurements were taken after 10 updatings. The error analysis was performed by the jackknife method over bins at different blocking levels. To reduce statistical errors we employed the isotropic (4D) APE smearing procedure [36], with smearing parameter $\epsilon = 0.5$. It was checked that numerical results are stable, within the statistical uncertainties, under small variations of the parameter ϵ.

Results confirm that the flux tube is almost completely formed by the longitudinal chromoelectric field E_l, which is constant along the flux axis and decreases rapidly in the transverse direction x_t. Measurements are realized at the middle point (labeled by $x_t = 0$) of the line connecting the static color sources and at various distances $x_t > 0$ from this point along one of the transverse spatial directions until $x_t = {}^{N_S}/_2$. To check rotational invariance, also points calculated at noninteger distances were considered at $\beta = 6.0$. Data were fitted to Eq. (4.16). In Fig. 4.9 the transverse distribution of the longitudinal chromoelectric field is displayed. The full line is the curve fitting the data. Eq. (4.16) appears to be able to reproduce accurately the transverse distribution of the longitudinal chromoelectric field, noninteger measurements included, but an attempt to restrict the fit only to points at integer distances yielded consistent values for the fit parameters, with a sensible reduction of the reduced chi-square, χ^2_r.

To save CPU time, the strategy was, then, to measure the connected correlator, Eq. (4.19), for integer transverse distances only at $\beta = 5.9,\ 6.0,\ 6.05,\ 6.1$. To reduce statistical fluctuations in gauge field configurations we performed measurements after several smearing steps. For each smearing, we fitted our data for the transverse shape of the longitudinal chromoelectric field to Eq. (4.16). As a result, we obtained the fit parameters for different smearing steps. This allowed us to check the dependence of these parameters on the number of smearing steps. In fact, we found well defined plateaux in the extracted parameter values versus the smearing steps. Table 4.1 reports the values of the fit parameters for smearing steps ranging from 16 up to 50. The parameters refer to the fit of the field strength tensor, corresponding to the connected correlator Eq. (4.19) at $\beta = 6.0$ and $\Delta = 6a$.

Note that the parameters ϕ, μ and ξ_v were obtained by the fitting procedure, while the Ginzburg-Landau parameter κ is evaluated by means of Eq. (4.17). We looked also for contamination effects on the longitudinal chromoelectric field due to the presence of the static color sources. To do this, we varied the distance Δ between the Polyakov lines: we found that the fitting parameters μ and λ/ξ_v for $\Delta = 4a$ were systematically higher than for $\Delta = 6a, 8a$. On the other hand, we obtained parameters consistent within the statistical uncertainties for the distances $\Delta = 6a$ and $8a$ (see Fig. 4.8).

TABLE 4.1: Summary of the fit values at $\beta = 6.0$ for $\Delta = 6a$. The last column gives the reduced chi-square.

Smearing	ϕ	μ	λ/ξ_v	κ	χ^2_r
16	6.191(141)	0.621(79)	0.309(95)	0.213(91)	0.018
18	6.218(125)	0.622(76)	0.287(82)	0.192(77)	0.011
20	6.227(109)	0.617(68)	0.277(72)	0.183(66)	0.010
22	6.222(98)	0.608(61)	0.271(64)	0.178(58)	0.010
24	6.207(88)	0.597(55)	0.269(58)	0.176(53)	0.011
26	6.184(81)	0.587(50)	0.269(54)	0.175(49)	0.011
28	6.155(75)	0.576(47)	0.269(51)	0.176(46)	0.011
30	6.122(70)	0.566(44)	0.270(48)	0.176(44)	0.010
32	6.087(66)	0.557(41)	0.271(46)	0.177(42)	0.009
34	6.049(63)	0.549(39)	0.271(45)	0.178(41)	0.008
36	6.011(60)	0.541(37)	0.272(43)	0.179(40)	0.007
38	5.973(58)	0.534(36)	0.273(42)	0.179(39)	0.005
40	5.935(56)	0.527(35)	0.274(42)	0.180(38)	0.004
42	5.897(54)	0.521(34)	0.274(41)	0.180(37)	0.003
44	5.859(53)	0.515(33)	0.275(40)	0.181(37)	0.003
46	5.822(51)	0.510(32)	0.275(40)	0.181(37)	0.002
48	5.786(50)	0.505(31)	0.276(39)	0.182(36)	0.002
50	5.751(49)	0.500(31)	0.277(39)	0.182(36)	0.001

Since for $\Delta = 8a$ our estimate of the fitting parameters was affected by large statistical errors, we focused on the distance $\Delta = 6a$ as a good compromise between the absence of spurious contamination effects due to the static color sources and a reasonable signal-to-noise ratio.

In Fig. 4.6 we display the fitting parameters ϕ, μ and λ/ξ_v for different values of gauge coupling β and smearing step. We see, at least for $\beta \geq 6.0$, that our estimate for the fitting parameters seems to be reliable and independent of the number of smearing steps. The same holds also for the Ginzburg-Landau parameter κ as obtained from Eq. (4.17). As for $\beta = 5.9$, we observe a slower approach of the fitting parameters to a plateau, although this effects overcomes the statistical uncertainties only in the case of the parameter ϕ. A possible reason for this phenomenon could be the presence of lattice artifacts which need a larger number of smearing steps to be washed out and spoil also the continuum scaling, as will be confirmed in what follows.

Within our approach the shape of the longitudinal chromoelectric field is fully characterized by the London penetration depth, λ, and the coherence length, ξ. Thus, in view of phenomenological applications in hadron physics, it is important to estimate these lengths in physical units. Firstly, we need to study the scaling of the plateau values of $a\mu$ with the string tension. For this purpose, we expressed these values of $a\mu$ in units of

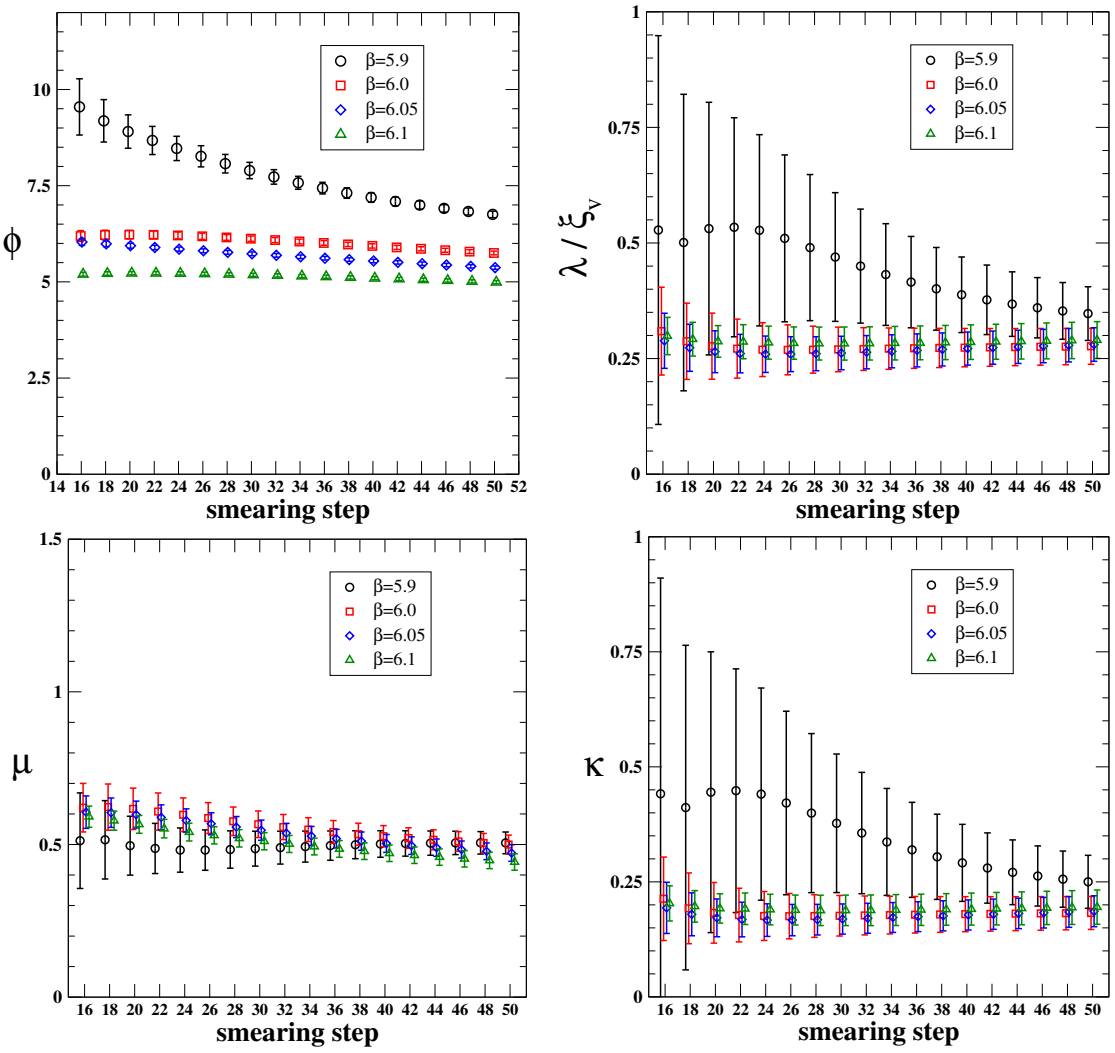

FIGURE 4.6: ϕ, λ/ξ_v, μ and κ versus the smearing step for $\Delta = 6a$. In the last three figures data have been slightly shifted along the horizontal axis for the sake of readability.

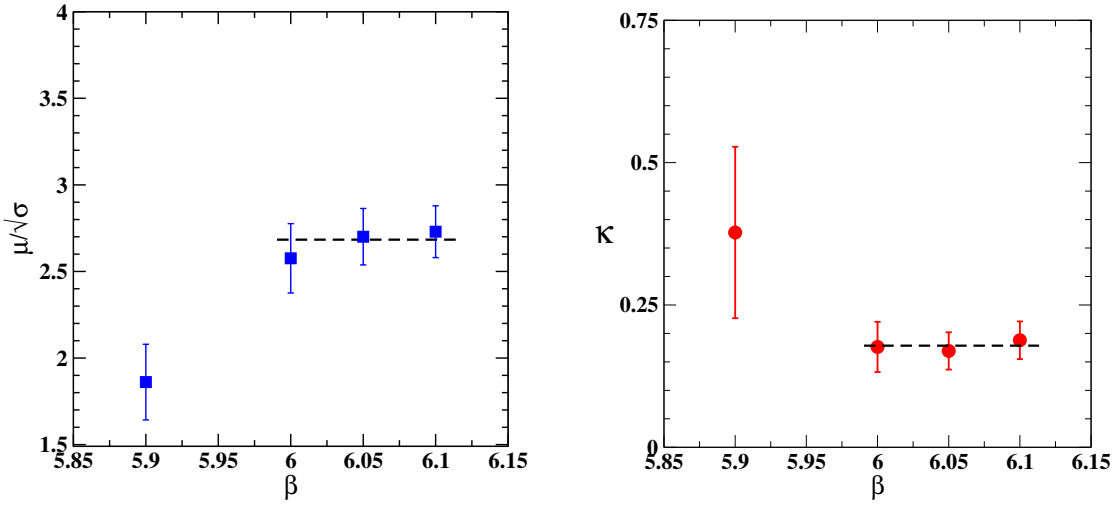

FIGURE 4.7: (Left) $\mu/\sqrt{\sigma}$ versus β. (Right) κ versus β. In both cases $\Delta = 6a$.

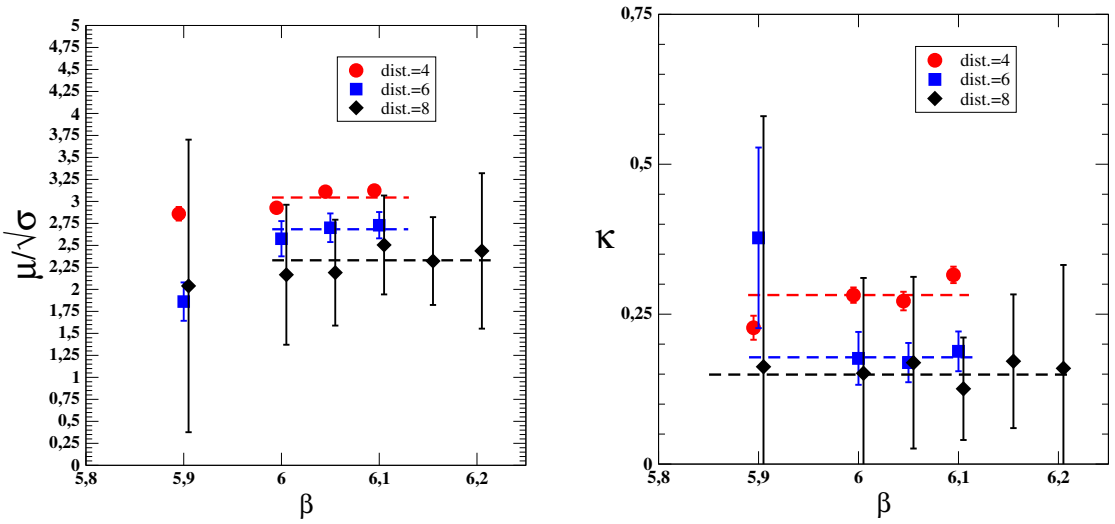

FIGURE 4.8: Distance effects on the scaling of $\mu/\sqrt{\sigma}$ and κ with β for $\Delta = 4, 6, 8a$.

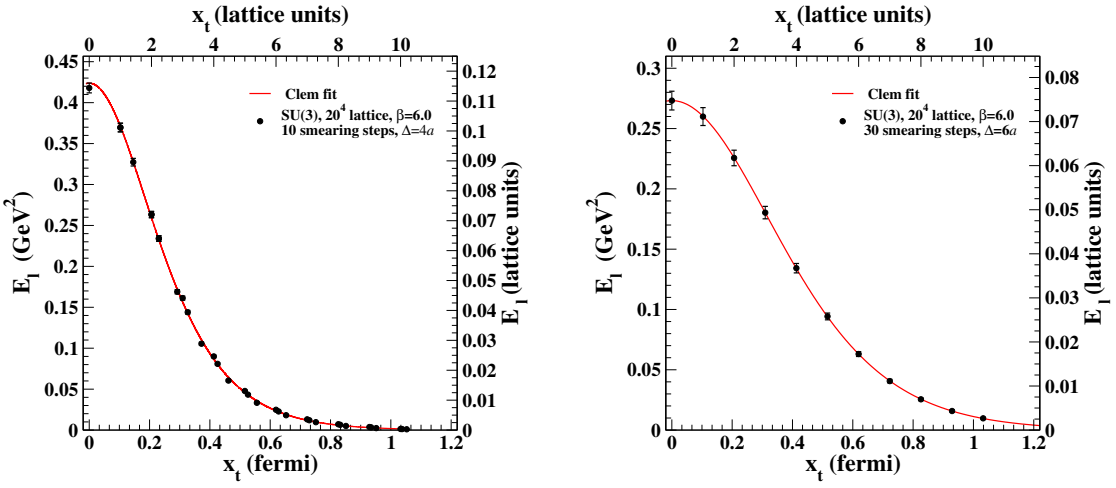

FIGURE 4.9: (Left) Longitudinal chromoelectric field E_l versus x_t , in lattice units and in physical units, for $\beta = 6.0$, $\Delta = 4a$ and after 10 smearing steps (Intermediate distances are included). (Right) The same for $\beta = 6.0$, $\Delta = 6a$ and after 30 smearing steps. The full line is the best fit using Eq. (4.16)

$\sqrt{\sigma}$, using the parameterization [83]:

$$\begin{aligned} \sqrt{\sigma}(g) &= f_{\mathrm{SU(3)}}(g^2)[1 + 0.2731\,\hat{a}^2(g) \\ &- 0.01545\,\hat{a}^4(g) + 0.01975\,\hat{a}^6(g)]/0.01364\,, \end{aligned} \tag{4.23}$$

$$\hat{a}(g) = \frac{f_{\mathrm{SU(3)}}(g^2)}{f_{\mathrm{SU(3)}}(g^2(\beta = 6))}\,,\ \beta = \frac{6}{g^2}\,,\quad 5.6 \leq \beta \leq 6.5\,,$$

where

$$f_{\mathrm{SU(3)}}(g^2) = \left(b_0 g^2\right)^{-b_1/2b_0^2} \exp\left(-\frac{1}{2b_0 g^2}\right)\,, \tag{4.24}$$

$$b_0 = \frac{11}{(4\pi)^2}\ ,\ b_1 = \frac{102}{(4\pi)^4}\,.$$

In Fig. 4.7 (Left) we show the ratio $\mu/\sqrt{\sigma}$ for different values of the gauge coupling. We see that for $\beta \geq 6.0$, μ scales according to the string tension. Fitting the data in the scaling window with a constant we get

$$\frac{\mu}{\sqrt{\sigma}} = 2.684(97) \; . \tag{4.25}$$

Likewise, the dimensionless Ginzburg-Landau parameter κ scales in the same interval of β (see Fig. 4.7 (Right)). Again, fitting with a constant gives

$$\kappa \; = \; 0.178(21) \; . \tag{4.26}$$

Our determinations, Eq. (4.25)) and Eq. (4.26), are in good agreement with the values reported in [77], namely

$$\frac{\mu}{\sqrt{\sigma}} = 2.799(38) \; , \quad \kappa = 0.243(88) \; , \tag{4.27}$$

obtained using the connected correlator built with the Wilson loop, Eq. (4.18).

Assuming the standard value for the string tension, $\sqrt{\sigma} = 420$ MeV, from Eq. (4.25) we get

$$\lambda \; = \; \frac{1}{\mu} \; = \; 0.1750(63) \text{ fm} \; . \tag{4.28}$$

Combining Eq. (4.28) and Eq. (4.26) we readily obtain

$$\xi \; = \; 0.983(121) \text{ fm} \; . \tag{4.29}$$

Finally, it is interesting to display the transverse structure of the longitudinal chromoelectric field produced by a static quark-antiquark pair in physical units, see Fig. 4.9.

4.6 Flux tubes in $SU(3)$ at nonzero temperature

What follows is based on [84, 85].

Our zero-temperature study has revealed how the peculiar tube-like shape of the chromoelectric field between a static quark-antiquark pair can be nicely described within the dual superconductor scenario for the QCD confining vacuum.

What follows concerns, instead, our investigations on the way growing temperature affects the tube-like shape and, in particular, on the fate of chromoelectric flux tubes across the deconfinement transition.

Again the study calls for the measurement of the Polyakov connected correlator, with some novelties on how the smoothing of configurations is accomplished, due to the necessity of preserving thermal fluctuations.

Also in this case simulations were performed using the Wilson action with periodic boundary conditions and the Cabibbo-Marinari algorithm [29] combined with overrelaxation on $SU(2)$ subgroups to update the configurations.

Lattice sizes were chosen in a way to investigate a sufficiently wide range of temperatures around the deconfinement one ($T_C = 260$ MeV), while staying within the range of validity of the parameterization [83] (see Sec. 4.5), which we use to fix the scale. In particular, we performed numerical simulation at finite temperatures on lattices with temporal extension ranging from $N_T = 6$ up to $N_T = 12$ and spatial size N_S, with aspect ratio $N_S/N_T \geq 4$. Simulated temperatures lie in the range $0.8T_C \div 1.5T_C$ according to:

$$T = \frac{1}{a(\beta)\, N_T} \,. \tag{4.30}$$

In order to reduce the autocorrelation time, measurements were taken after 10 updatings. The error analysis was performed by the jackknife method over bins at different blocking levels. To reduce statistical errors we employed a single HYP smearing step over links in the temporal directions and several steps of anisotropic ($3D$) APE smearing procedure [36], with smearing parameter $\epsilon = 0.67$, over links in the spatial directions.

Measurements are realized at the middle point (labeled by $x_t = 0$) of the line connecting the static color sources, and at various distances $x_t > 0$ from this point along one of the transverse spatial directions until $x_t = 10a$. Only integer distances were considered in this case.

All field components were measured, but results confirm that, even at finite temperature, the flux tube is almost completely formed by the longitudinal chromoelectric field E_l, which is constant along the flux axis and decreases rapidly in the transverse direction x_t.

For each smearing, we fitted our data for the transverse shape of the longitudinal chromoelectric field to Eq. (4.16). As a result, we obtained the fit parameters for different smearing steps.

Smearing plays a crucial role in the extraction of our physical signal, and a criterion has to be determined in order to have our measurements maximally amplified at different β, T, Δ. Since the effect of smearing consists into an increase in the intensity of the measured field at each fixed distance, we realized that the plateau, that is always found

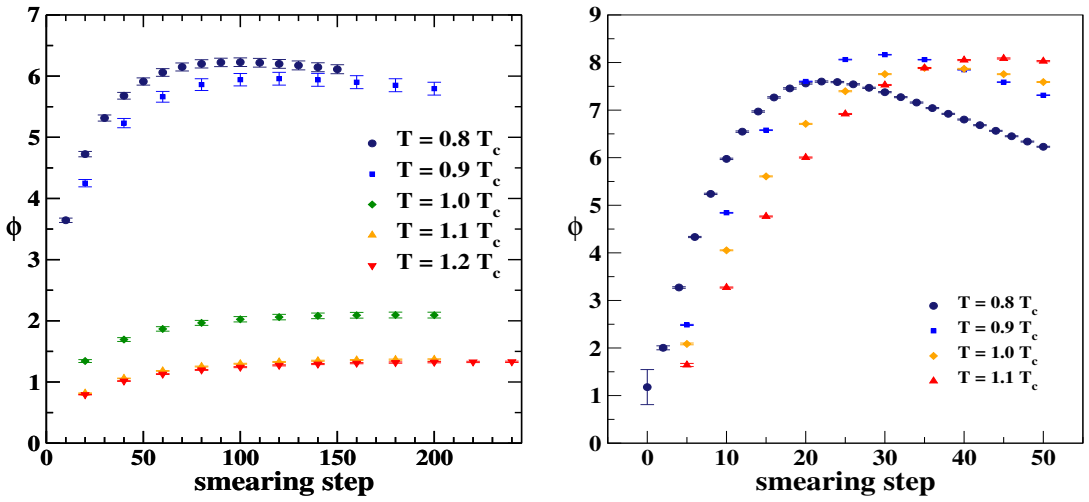

FIGURE 4.10: ϕ *vs* smearing for measurements of the Polyakov (Left) and Wilson (Right) connected correlator at $T \neq 0$, on a $40^3 \times 10$ lattice.

in the ϕ versus smearing behavior and that is shown in Fig. 4.10, is a good hint that the signal has reached its maximum before the physical signal gets spoiled by an excess of smearing.

A scaling analysis was performed, at least for $T = 0.8T_C$, to check that the coupling corresponding to that fixed temperature, for various N_T, lies within the scaling region.

The scaling analysis gets complicated with respect to the $T = 0$ case. The reason is that for $T \neq 0$ the changes in the coupling constant, to get to the continuum limit, have to be accomplished at fixed temperature, which implies considering multiple N_T. Changes in N_T, on the other hand, imply big steps in β that affects appreciably the physical distance between the two sources, if one insists on keeping fixed that distance in lattice units [3]. Under small changes in the physical distance, as in the $T = 0$ case, only the parameter ϕ appeared to be affected and this indicated a change in the intensity of the field while its profile was left unchanged.

What we have found, and that confirms our previous findings, is that Δ has to be chosen in a way that for all considered couplings (for instance, to keep $T = 0.8T_C$ we had to consider $\beta = 6.050, 6.170, 6.370$ respectively for $N_T = 10, 12, 16$) the distance in physical units has to be beyond half a fermi. Our initial difficulty in getting to the scaling window was again due to distortion effects brought about by the proximity of color sources: they got nearer and nearer, while increasing the coupling, until they eventually were less than ~ 0.5 fm apart, that is below the onset of the linear behavior in the static potential. This deeply affected the quality of our fits and produced sensible changes in all fit parameters.

[3] In the zero temperature study, the physical distance between the quark and the antiquark, due to changes in the coupling, varied by around 10% at fixed distance in lattice units.

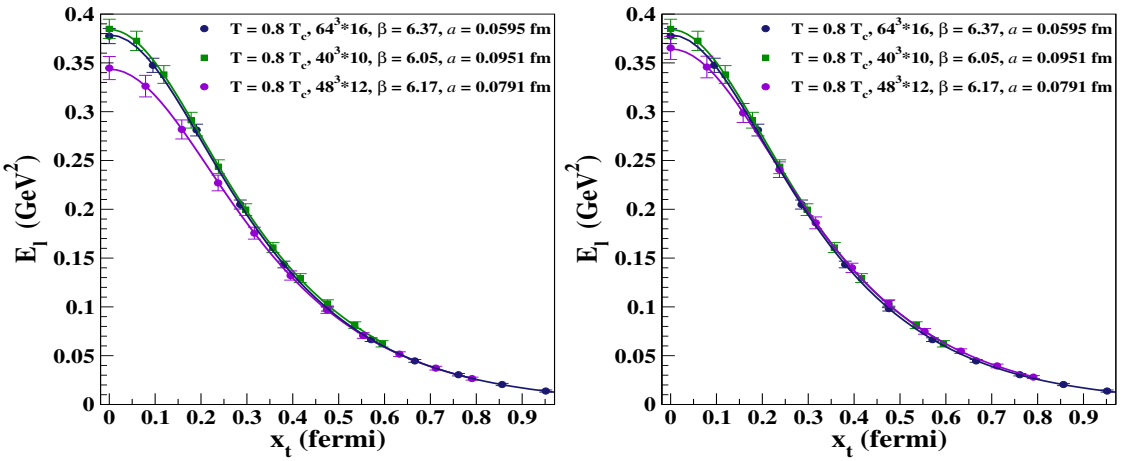

FIGURE 4.11: (Left) Longitudinal chromoelectric field E_l versus x_t , in physical units, for $\beta = 6.050, 6.170, 6.370$, $\Delta = 8a, 10a, 12a$ respectively, and after 100,140,180 smearing steps respectively. (Right) The same but with the field values at $\beta = 6.170$ rescaled by the factor $\phi_{avg}/\phi_{\beta=6.170}$.

Once understood the "distance effect", being clear that the highest coupling requires the biggest distance in lattice units, there are two possibilities: either we fix the distance in lattice units to the one corresponding to the highest β, or one requires the physical distance between the sources to be approximately constant. We did both. Within the first approach, the scaling holds for the physical parameters $\mu/\sqrt{\sigma}$ and κ (exactly as shown at $T = 0$), but the second approach has the advantage that less statistics is needed for smaller couplings (since Δ is decreased and the signal is increased consistently) and the achievement of the continuum limit can be shown already at the level of the measured field.

Then, at $T = 0.8T_C$, we considered Polyakov lines separated by $\Delta = 8a, 10a, 12a$ for gauge couplings $\beta = 6.050, 6.170, 6.370$, respectively. Scaling appears to be achieved already at $\beta = 6.050$ with the field at $\beta = 6.170$ not overlapping with the others just because the physical distance in that case is slightly bigger. However, both $\mu/\sqrt{\sigma}$ and κ display a nice scaling behavior and it is enough to multiply the field by the ratio between the average ϕ from the other two sets and the ϕ value at $\beta = 6.170$ in order to get a very nice overlap of all field profiles. This fact is a further argument in favor of the above analysis of the "distance effect".

Having selected the gauge coupling region were there is indication of continuum scaling, we focused on the temperature dependence of the longitudinal chromoelectric field. We measured the connected correlator Eq. (4.19) on $40^3 \times 10$ lattices for physical temperatures ranging from $0.8\,T_c$ up to $1.2\,T_c$. We chose the distance between the two Polyakov lines such that $\Delta > 0.7$ fm. In Table 4.2 we summarize the simulation setup and the corresponding best-fit values of the parameters.

TABLE 4.2: Simulation parameters for the lattice $N_S \times N_T = 40^3 \times 10$, fitted values of the parameters, and reduced chi-square χ^2.

β	Δ [fm]	T/T_C	ϕ	μ	ξ_v	χ^2_r
6.050	0.761	0.8	6.201(68)	0.382(13)	3.117(191)	0.02
6.125	0.761	0.9	5.941(101)	0.337(20)	3.652(360)	0.01
6.200	0.756	1.0	2.061(45)	0.328(22)	3.312(389)	0.01
6.265	0.757	1.1	1.359(9)	0.344(7)	4.286(131)	0.06
6.325	0.760	1.2	1.324(11)	0.332(8)	4.248(142)	0.06

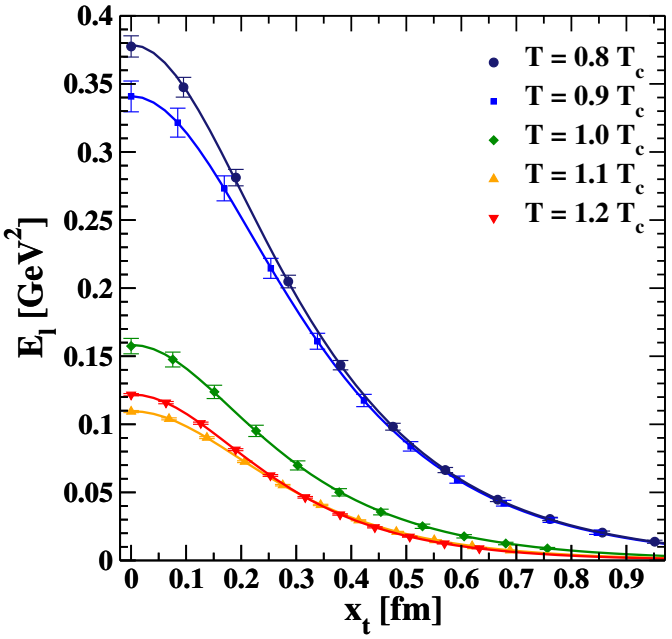

FIGURE 4.12: Behavior of the longitudinal chromoelectric field at a fixed lattice size $40^3 \times 10$ and various gauge couplings in the scaling region *vs* the transverse distance.

In Fig. 4.12 we display the transverse distribution of the longitudinal chromoelectric field for the different temperatures used in the present study. From Fig. 4.12 we infer that, as the temperature is increased towards and above the deconfinement temperature T_c, the strength of the flux-tube chromoelectric field decreases very quickly, while the size of the flux tube does not seem to vary appreciably. This behavior suggest that, by increasing the temperature above the critical temperature, the flux tube is evaporating while almost preserving his shape.

This scenario with flux-tube evaporation above T_c has no correspondence in ordinary type-II superconductivity, where instead the transition to the phase with normal conductivity is characterized by a divergent fattening of flux tubes as the transition temperature is approached from below. To better characterize this point, it is fundamental to inquire on the temperature dependence of both the penetration depth and coherence

length, since within our approach the shape of the longitudinal chromoelectric field is fully characterized by the London penetration depth and the coherence length.

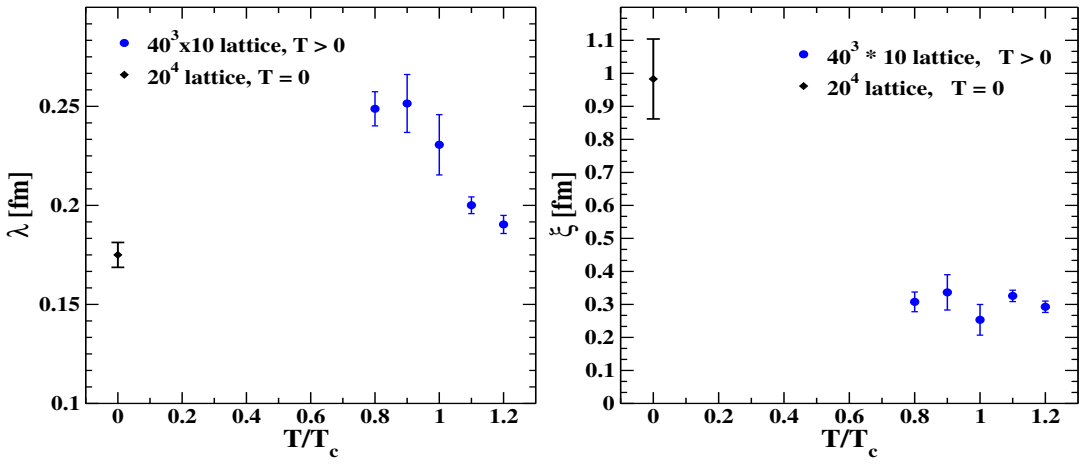

FIGURE 4.13: (Left) London penetration depth λ *vs* T/T_c. The $\lambda_{T=0} = 0.1750(63)$ value is included. (Right) Coherence length ξ *vs* T/T_c. The $\xi_{T=0} = 0.983(121)$ value is included.

The penetration depth and the coherence length, in physical units, versus the reduced temperature T/T_c are displayed in Fig. 4.13. We also report the values of these length at zero temperature obtained previously on 20^4 lattices [81]. As concern the London penetration length, Fig. 4.13 shows that this length seems to slightly increases with respect to the zero-temperature values for temperatures $T < T_c$, and then it decreases above the critical temperature. However, the overall variation of λ is rather modest. So that, we can safely affirm that the London penetration length is almost temperature independent. On the other hand, at finite temperatures the coherence length suffers a rather drastic reduction with respect to the zero-temperature value. After that, we see from Fig. 4.13 that ξ is almost constant across the deconfinement temperature. In any case, these results indicate clearly that the flux tube survives even after the color deconfinement transition.

4.7 Flux tubes in $SU(3)$ at nonzero temperature in the magnetic sector

In this Section we would like to investigate the structure of QCD in the high temperature regime [86, 87]. At high temperatures, through dimensional reduction, QCD can be reformulated as an effective 3D theory with the scale of the effective couplings given in terms of the temperature. However, the QCD effective theory is quite complicated even at high temperatures since straightforward perturbation theory does not work due to the presence of infrared singularities in the magnetic sector. These nonperturbative effects

will manifest themselves in correlation functions for the spatial components of gauge fields. In fact, it is known since long time that gauge invariant correlation functions for spatial components of the gauge fields, the spatial Wilson loops, obey an area law behavior in the high temperature phase with a nonzero spatial string tension σ_s [88, 89].

An analysis of the temperature dependence of the spatial string tension thus yields information on the importance of the non-static sector for long-distance properties of high temperature QCD. It turns out that, for temperatures larger than $2T_c$ the spatial string tension is consistent with the behavior:

$$\sqrt{\sigma_s} \;=\; \gamma\, g(T)\, T\;, \tag{4.31}$$

where $g(T)$ is the temperature dependent coupling constant running according to the two-loop β-function, and γ is a constant; $\gamma = 0.586 \pm 0.045$ for $SU(3)$ [89], and $\gamma = 0.369 \pm 0.015$ for $SU(2)$ [88].

We see, thus, that for a better understanding of the nonperturbative structure of QCD at high temperature it is fundamental to arrive at a quantitative description of the properties of the spatial string tension. To this end, we considered the connected correlator build with gauge links belonging to the spatial sub-lattice. Obviously, in this case the field strength tensor Eq. (4.18) corresponds to the chromomagnetic field. As in the previous study, we performed simulations on $40^3 \times 10$ lattices for physical temperatures ranging from $0.8T_c$ up to $1.5T_c$. We chose Wilson loops such that $\Delta > 0.7$ fm where, now, Δ is the length of the Wilson loop (see Table 4.3 for the summary of our simulation setup).

TABLE 4.3: Simulation parameters for the lattice $N_S \times N_T = 40^3 \times 10$, fitted values of the parameters, and reduced chi-square χ^2.

β	Δ [fm]	T/T_C	ϕ	μ	ξ_v	χ^2_r
6.050	0.761	0.8	7.600(14)	0.653(5)	3.313(6)	1.52
6.125	0.761	0.9	8.164(7)	0.593(3)	5.978(38)	2.90
6.200	0.756	1.0	7.887(11)	0.544(4)	6.413(76)	1.27
6.265	0.757	1.1	8.085(12)	0.498(6)	7.572(117)	0.45
6.490	0.759	1.5	9.475(80)	0.393(23)	10.793(721)	0.01

Remarkably, we found that even in this case the chromomagnetic flux tube is built from the longitudinal chromomagnetic field only. Moreover, the longitudinal chromomagnetic field profile in the transverse directions is accounted for by Eq. (4.15). In fact, in Table 4.3 we report the values of the fitted parameters together with reduced chi-square. The transverse profiles of the longitudinal chromomagnetic field for different temperatures are displayed in Fig. 4.14. Unlike the longitudinal chromoelectric field, we see

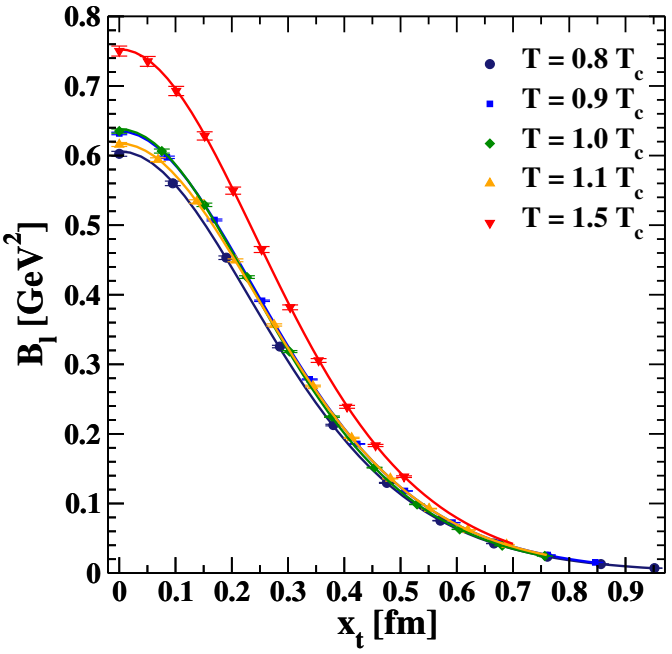

FIGURE 4.14: Transverse profile of the longitudinal chromomagnetic field *vs* the transverse distance across the deconfinement temperature.

that the strength of the longitudinal chromomagnetic field and the size of the flux tube increase with the temperature. Moreover, it turns out that the temperature behavior of the chromomagnetic flux tube is consistent with the observed increase of the spatial string tension. In fact, we evaluated the spatial string tension reconstructed from the profile of the chromomagnetic field according to Ref. [77] and found results which are in agreement with the direct, standard determination from spatial Wilson loops, Eq. (4.31) for $SU(3)$, as reported in Ref. [89].

4.8 Summary and outlook

The confinement phenomenon and the deconfinement transition have been addressed, in this work, within the dual superconductor scenario. In such a context confinement is characterized by the existence and properties of the flux tubes generated by the interaction of static sources in the QCD vacuum.

In its first part, the purpose of our research was just to confirm the validity of dual superconductivity at $T = 0$. The relevance of such a test depends on the fact that the Wilson connected correlator used in previous studies was substituted by the Polyakov connected correlator as well as the cooling procedure was replaced by smearing. Those two changes were essential aiming at finite temperature studies, but, before proceeding

to the $T \neq 0$ case, it was our duty to ensure the agreement of the two approaches at $T = 0$. As shown in Sec. 4.5, the agreement was found and results were published in [81].

As a further remark, we observe that what we called "penetration length" could match the "intrinsic width" of the flux tube as defined in Ref. [90], where the adopted probe observable was the disconnected correlator of two Polyakov lines and a plaquette.

Our result is also in good agreement with studies performed with the connected correlator with Wilson loop, and confirm that the $SU(3)$ vacuum behaves as a type-I dual superconductor. This conclusion is shared with Ref. [91], where the non-Abelian dual Meissner effect is investigated within the so-called "restricted field dominance". Finally, we observe that our estimate of the London penetration length is in good agreement with the recent determination in Ref. [92], obtained using correlators of plaquette and Wilson loop not connected by the Schwinger line, thus leading to the (more noisy) squared chromoelectric and chromomagnetic fields.

Afterwards, we turned our attention to the nonzero temperature case. Here, the final purpose was to check the temperature dependence of the London penetration depth and coherence lenght and the survival of flux tubes structures beyond the critical temperature at which deconfinement is expected to happen in $SU(3)$ pure gauge theory. It is not obvious, indeed, how far does the dual superconductor analogy holds.

There are both phenomenological and theoretical hints suggesting that flux-tube structures should survive the deconfinement temperature.

On a phenomenological and experimental ground it is known that the dissociation of quarkonia $(c\bar{c}, b\bar{b})$ states takes place at temperatures beyond the critical one depending on the binding energy, hence typical radii, of these hadrons. For instance, the typical binding radii of the ground states of J/ψ and Υ are $r_Q \simeq 0.1 - 0.2$ fm. We know that Debye charge screening radius r_D in QGP decreases strongly with the temperature above T_C causing a striking decrease of the range of strong interactions, but it is only for $r_D \ll r_Q$, possibly also far beyond T_C, that the two heavy quarks stop interacting and the bound state melts.

Furthermore, a new picture for finite $T - \mu$ QCD phase diagram, based on a competition between electrically and magnetically charged quasiparticles has been proposed recently [93], from which a different scenario for confinement follows. In the proposed phase diagram, a "magnetically dominated", low-temperature region and an "electrically dominated", high-temperature one are identified and separated by an equilibrium region at intermediate $T - \mu$ depending on the coupling strength of both electric and magnetic interactions. It is the "magnetically dominated" region at low-T (and low-μ) that can, in turn, be subdivided into a "confining part", in which electric field is confined into

quantized flux tubes surrounded by the condensate of magnetic quasiparticles (forming t'Hooft-Mandelstamm "dual superconductor"), and a "postconfinement" region at $T > T_C$, but below the equilibrium temperature, in which electric quasiparticles are still strongly coupled and connected by the electric flux tubes.

Remarkably, in the present study we found that also at finite temperatures the flux tube is formed by the longitudinal chromoelectric field only. Moreover, we found that the flux tube structure survives to the deconfinement transition. However, the behavior of the flux-tube chromoelectric field across the deconfinement transition does not match the dual version of the effective Ginzburg-Landau description of ordinary type-II superconductors. In particular, the Ginzburg-Landau parameter κ is seen to be $\kappa \ll 1$ at zero temperature, while $\kappa \simeq 1$ near the deconfinement critical temperature. Indeed, we found that as the temperature is increased towards and above the deconfinement temperature T_c, the amplitude of the field inside the flux tube gets smaller, while the shape of the flux tube does not vary appreciably across the deconfinement temperature leading to a scenario which resembles an evaporation of the flux tube.

We, also, investigated the chromomagnetic sector which is relevant for the QCD effective theory at high temperatures. We focused on the chromomagnetic flux tube which is responsible for the nonzero spatial string tension. Even in the chromomagnetic sector we found that the flux tube is built mainly from the longitudinal chromomagnetic field. Our results showed that the strength and the size of the chromomagnetic flux tube increase with the temperature, consistently with the temperature behavior of the spatial string tension. Our findings, then, confirm the importance of long-range chromomagnetic correlations in high-temperature QCD.

Finally, it is worthwhile to stress that our results could have important phenomenological applications in hadron physics. In particular, we believe that our findings are relevant to clarify the nature of the initial state of the quark-gluon plasma in heavy-ion collisions. However, before attempting phenomenological applications, it is important to extend the present study to full QCD, i.e. to $SU(3)$ lattice gauge theory with improved gauge action and dynamical quarks with masses at (almost) the physical point.

Therefore, a new MILC application was created. Our measurements will be performed in QCD with $N_f = 2 + 1$ staggered fermions. The adopted discretization is the HISQ/tree action as implemented in the MILC code. It will be also possible to investigate flux tubes on a line of constant physics by appropriate tuning of the couplings. At the time of writing the targets created for the new application are:

- *su3_rhmc_hisq_wilson* implements Wilson connected correlator and isotropic ($4D$ APE) smearing (suited for $T = 0$ studies);

- *su3_rhmc_hisq_wilson_hyp* implements Wilson connected correlator and anisotropic ($3D$ APE and temporal HYP) smearing (suited for $T = 0$ studies);
- *su3_rhmc_hisq_wilson_anisotropic_smearing* implements Wilson connected correlator and anisotropic ($3D$ APE) smearing (suited for $T \neq 0$ studies in the chromomagnetic sector);
- *su3_rhmc_hisq_polyakov* implements Polyakov connected correlator and isotropic ($4D$ APE) smearing (suited for $T = 0$ studies);
- *su3_rhmc_hisq_polyakov_nonzeroT* implements Polyakov connected correlator and anisotropic ($3D$ APE and temporal HYP) smearing (suited for $T \neq 0$ studies).

Chapter 5

Numerical study of the Roberge-Weiss transition

The Roberge-Weiss (RW) transition at imaginary chemical potential, in $N_f = 2$ flavors QCD with Wilson fermions, with particular reference to the nature of the *RW endpoint*, will be the subject of the present chapter.

What makes studies in the (unphysical) imaginary chemical potential region interesting, and physically relevant, is the fact that they can be used to constrain the QCD phase diagram at zero and (real) finite chemical potential μ, which is useful to clarify, for instance, the currently unknown nature of the phase transition in the two flavor chiral limit at zero chemical potential and the existence of a critical endpoint in the $\mu - T$ phase diagram of QCD. The nonzero real μ region is, indeed, not directly accessible to lattice QCD studies because of the *sign problem* already introduced in Chap. 2. At imaginary chemical potential, instead, there is no sign problem preventing the investigation of the phase structure via lattice simulations.

Previous studies using both staggered and Wilson fermions, revealed that the RW endpoint, that is the point at which the center RW transition changes from first order to crossover, depends in a non-trivial way on the masses of the quarks included in the model: for high and low masses, it is a triple point at the intersection with the deconfinement and chiral transitions lines, respectively. For intermediate mass values, instead, it is found to be a second order endpoint. The two different mass regions are separated by two values of mass for which the RW endpoint is a tricritical point.

As a meaningful extension of a previous study on the critical RW endpoint for $N_f = 2$ Wilson fermion QCD, on $N_T = 4$ lattices [94], the same analysis at $N_T = 6$, hence on finer lattices, has been carried out. The obtained results will be described in Sec. 6.4,

after a general discussion on the phase diagram of QCD at imaginary chemical potential in Sec. 5.1, and the description of the measured observables and the simulation setup in Sec. 5.2.

What follows is mainly based on [95, 96].

5.1 QCD phase diagram at imaginary chemical potential

As already discussed in Sec. 2.1.2, the QCD phase diagram in the $T - \mu_i$ plane is characterized by the RW symmetry of the QCD partition function in a way that, in addition to the transition lines corresponding to the chiral/deconfinement transition, phase transitions between adjacent $Z(3)$ sectors take place, in correspondence to the critical values for the imaginary chemical potential given by $\mu_I^c/T = (2k+1)\pi/3$, with $k \in \mathbb{Z}$ (the so called Roberge-Weiss transitions). Such periodic transitions are first order phase transitions at high temperature until they become crossovers at low temperatures, where the RW periodicity in the QCD action is smoothly realized [9]. The first order lines end in a critical endpoint, which is what we call "RW endpoint".

As it has been numerically clarified, the analytic continuation to imaginary chemical potential of the thermal deconfinement/chiral transition line characterizing the real-μ phase structure, meets the RW endpoint of the RW transition lines. Furthermore, what characterizes the QCD phase structure at nonzero imaginary chemical potential is its dependence on the value of the masses of the quarks included in the theory. In the present case, dependence is on the mass $m_{u,d}$ of the up and down quarks, that are considered degenerate.

What is, by symmetry, mass-independent is the fact that a true phase transition takes place at the RW endpoint. This is because, at critical values for the imaginary potential μ_I^c, the system possesses an exact center symmetry, which undergoes spontaneous breaking while the temperature grows and the system selects one, out of two equivalent, specific center sector. Still, the nature of such a genuine transition is not fixed by symmetry and is found to depend on the quark masses. One has to think about a 3D phase diagram having T, μ_i and $m_{u,d}$ on its axes, to have a clearer qualitative picture, at least for the $N_f = 2$ case.

The transition at the RW endpoint can either be a second order transition in the universality class of the 3D Ising model, or a first order phase transition as it is in the quenched (infinite quark mass) limit. In this latter case, the RW endpoint is a triple point at the intersection of three first order critical lines. Of the two further critical lines, beyond the RW critical line, the one extending towards the $\mu_i = 0$ axis is interpreted as the

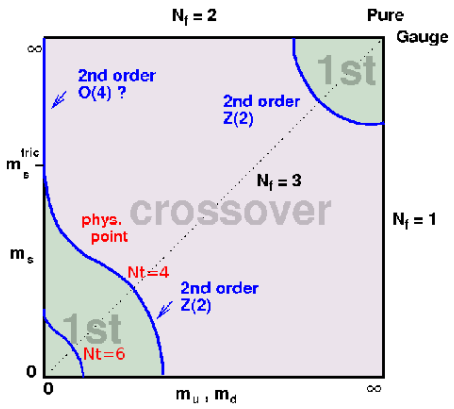

FIGURE 5.1: Schematic phase diagram for $N_f = 2 + 1$ QCD in the $m_s - m_{u,d}$ plane at $\mu = 0$. On finer lattices, the chiral critical line moves towards smaller quark masses shrinking the first order region at the bottom left corner. This figure is taken from [97].

analytic continuation, to imaginary chemical potential, of the physical transition line, in agreement with the expectation that this last meets the RW line on its endpoint.

At lower masses for the two light quarks (as shown in the Columbia plot in Fig. 5.1), at least for finite m_s values, the $\mu = 0$ transition becomes a crossover passing through the second order line. In the analytic continuation to imaginary chemical potential, there must then be a second order endpoint separating the crossover region from the, above mentioned, first order critical line. It is such endpoint, that approaches the RW endpoint while quark masses are varied. Said in other words, the first order line departing from the RW endpoint has a second order critical endpoint, whose vicinity to the $\mu = 0$ axis depends on the quark masses.

In such a scenario there exists a mass value at which the RW endpoint becomes a tricritical point. This marks the endpoint of the line of triple points in the mass direction. The corresponding phase structure in the $T - \mu_i$ plane can be schematically represented as in Fig. 5.2 for the region of high masses, and, according to previous findings, the same phase structure is realized starting from the chiral limit of zero masses and increasing them.

That this is really the case, at least for finite lattice spacing, has been confirmed by recent studies carried out both for $\mathrm{N_f} = 2$ [94, 98] and $\mathrm{N_f} = 3$ (degenerate) [99] quark flavors. Two tricritical quark masses separating the first order regime from the second order one, have been identified.

Plotting the nature of the RW endpoint in a $T - m_{u,d}$ plane, one would then have two lines of triple points outside the range $[m_{light}^{\mathrm{tric}}, m_{heavy}^{\mathrm{tric}}]$, whose edges are the two tricritical masses $m_{light}^{\mathrm{tric}}$ and $m_{heavy}^{\mathrm{tric}}$, and a line of a second order critical endpoints inside that range.

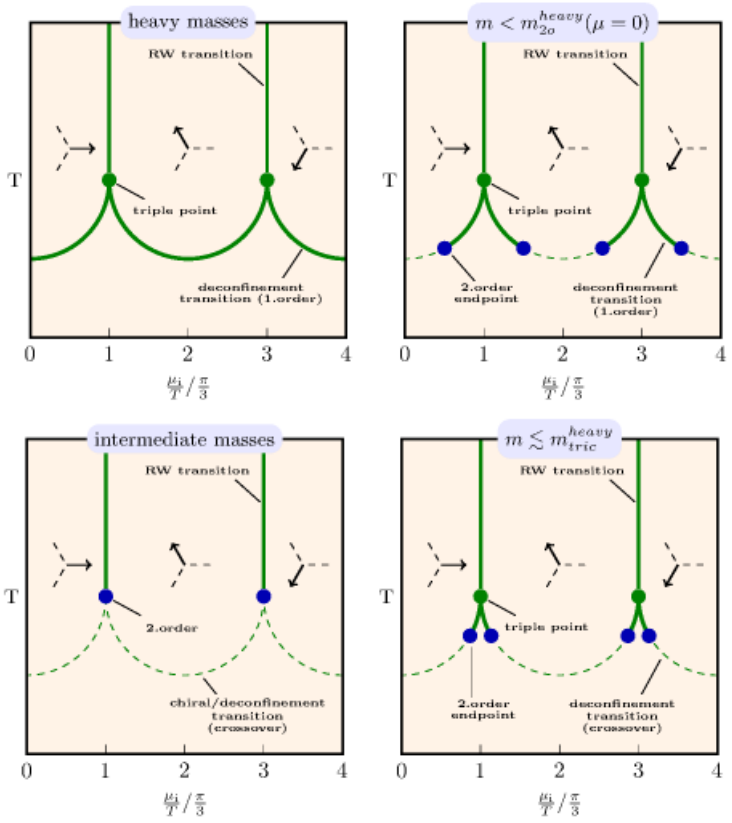

FIGURE 5.2: QCD phase diagram in the $T-\mu_I$ plane. The solid vertical lines represent the RW transitions at the edge center $Z(3)$ sectors characterized by a fixed phase in the Polyakov loop. The dots at the end of RW critical lines, are the RW endpoints and can be triple points, tricritical points or second-order critical endpoints. The dashed lines represent the chiral/deconfinement transition and the way their nature is changed by the quark mass value, which is decreased clockwise from the top left corner. This figure is taken from [94].

It is appropriate to reaffirm here, that the presence of the low-mass critical point in the $T - m_{u,d}$ plane at $\mu = 0$ and for $N_f = 2$ has not been clarified yet and that both the masses and the number of considered flavors play a role in determining the order of the chiral/deconfinement transition. However, within the just described scenario, it has been conjectured [100] that the nature of the transition at $\mu = 0$, as a function of the quark masses, may depend just on the nature of the RW endpoint, being first order only when the first order line departing from the RW triple endpoint is able to reach the $\mu = 0$ axis.

The just described phase structure can be nicely depicted, see Fig. 5.4 (Left), in a 3D plot having $m_{u,d}, m_s$ and $(\mu/T)^2$ as axis, so that for $(\mu/T)^2 = 0$ we simply have the Columbia plot, but the effect of non-vanishing imaginary chemical is displayed with the $Z(2)$ second order critical lines ($\mu = 0$) spanning critical surfaces that end in tricritical lines at $(\mu/T)^2 = -(\pi/3)^2$.

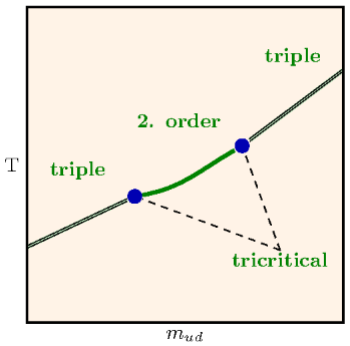

FIGURE 5.3: QCD phase diagram in the $T - m_{u,d}$ plane at a fixed critical imaginary chemical potential $\mu_I = \mu_I^c$. This figure is taken from [94].

Moreover, it is worth remarking that the position of the tricritical points, as identified in the studies at imaginary chemical potential, changes as the continuum limit is approached. According to previous findings, the two tricritical points are both expected to shift towards lower masses, as one approaches the continuum limit [97], in agreement also with what indicated, for the $\mu = 0$ case in Fig. 5.1 and as depicted in Fig. 5.4 (Right).

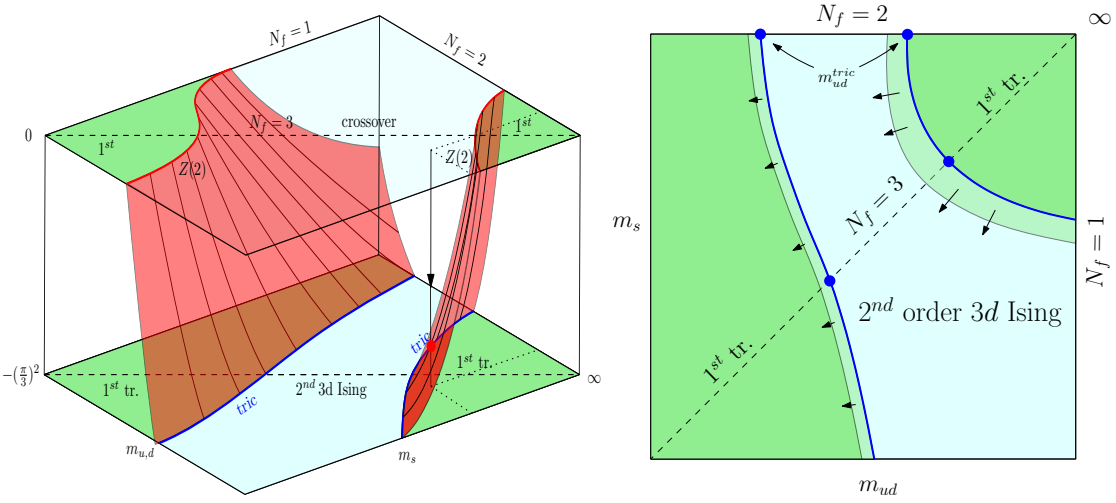

FIGURE 5.4: (Left) 3D $m_{u,d} - m_s - (\mu/T)^2$ phase diagram. (Right) Bottom plane of the same phase diagram where the expected shift, in the continuum limit, of the tricritical lines at μ_I^c/T towards lower masses is displayed. This figures are taken from [95].

5.2 Observables and simulation setup

The QCD grand canonical partition function with $N_f = 2$ mass-degenerate quarks at imaginary chemical potential μ_I, once the integration over the fermionic dof has been

performed, is given by

$$Z(T,\mu_I) = \int \mathcal{D}U e^{-S_G[U]} \left(\det D[U,\mu_I]\right)^2 , \tag{5.1}$$

where $S_G[U]$ is the gauge part of the action and $D[U,\mu_I]$ is the fermion matrix. In the present study the standard Wilson gauge action,

$$S_G[U] = \beta \sum_n \sum_{\mu<\nu} \Big(1 - \frac{1}{3}\mathrm{Re}\,\mathrm{Tr}\, U_{\mu\nu}(n)\Big) , \tag{5.2}$$

where $U_{\mu\nu}(n)$ is the elementary plaquette and $\beta = {}^{2N_c}/_{g^2}$ with $N_c = 3$, has been used along with the the standard Wilson discretization of dynamical fermions, whose fermion matrix is given by

$$\begin{aligned} D_{n,m} &= \delta_{n,m} - \kappa \sum_{i=\pm1}^{\pm3} \Big[(1-\gamma_i)\, U_i(n)\, \delta_{n+\hat{i},m}\Big] \\ &- \kappa\Big\{(1-\gamma_0)e^{+a\mu} U_0(n)\delta_{n+\hat{0},m} + (1+\gamma_0)e^{-a\mu} U_0^\dagger(m)\delta_{n-\hat{0},m}\Big\} . \end{aligned} \tag{5.3}$$

In the last equation n and m refer to lattice sites, $\hat{i}$ and $\hat{0}$ are unit vectors on the lattice and a is the lattice spacing. Moreover, $\gamma_{-i} \equiv -\gamma_i$ and $U_{-i}(n) \equiv U_i^\dagger(n-\hat{i})$. The quark mass $m_{u,d}$ is contained in the expression for the hopping parameter κ via

$$\kappa = \frac{1}{2(a\, m_{u,d} + 4)} . \tag{5.4}$$

The observable used to distinguish between the $Z(3)$ center sectors is the phase of the Polyakov loop L. In particular, the shifted phase $\phi = \varphi - \mu_I/T$ of the Polyakov loop is an order parameter to distinguish between the low-T (disordered) phase and the high-T (ordered) phase. Furthermore, choosing $\mu_I/T = \pi \pm 2\pi k,\ k \in \mathbb{Z}$ as it is done in this study, it is the imaginary part of the Polyakov loop itself, that can be used as order parameter.

Given that the temperature on the lattice varies with a and N_T according to

$$T = \frac{1}{a(\beta)\, N_T} , \tag{5.5}$$

we set $a\mu_I = \pi/6$ for $N_T = 6$.

It is now clear that the main observable of interest in this study is the order parameter for the transition under investigation that, as already stated, is the imaginary part of the spatially averaged Polyakov loop: L_{Im}. It is worth remarking, however, that also

	Crossover	1^{st} triple	Tricritical	$3D$ Ising
B_4	3	1.5	2	1.604
ν	–	1/3	1/2	0.6301(4)
γ	–	1	1	1.2372(5)

TABLE 5.1: Critical values of ν, γ and $B_4 \equiv B_4(X)$ for some universality classes [101].

the spatially averaged square norm of the Polyakov loop, $\|L\|$, as an order parameter for the thermal phase transition, has been measured and taken into account .

The nature of the Roberge-Weiss endpoint is, however, only clarified downstream a finite size scaling analysis, which is needed, since only in the thermodynamic limit $V \to \infty$ true nonanalytic phase transitions can occur. This is the reason why the distribution of the order parameter as well as all its relevant cumulants, around the critical coupling β_c, are measured on a set of different spatial lattice sizes N_S.

The finite size scaling analysis is, in particular, applied to the susceptibility of the order parameter. For a generic observable X, it is defined as

$$\chi(X) \equiv N_S^3 \big\langle (X - \langle X \rangle)^2 \big\rangle \, . \tag{5.6}$$

Around the critical coupling β_c, $\chi(X)$ is expected to scale according to

$$\chi = N_S^{\gamma/\nu} f\left(\frac{\beta - \beta_c}{\beta_c} N_S^{1/\nu} \right) \, , \tag{5.7}$$

where f a universal scaling function and γ and ν are the critical exponents, whose value depends on the universality class of the transition, again according to Table 5.1.

This means that, with the critical exponents γ and ν and the critical coupling fixed to the correct values, in plots of $\chi/N_S^{\gamma/\nu}$ *vs* $t\, N_S^{1/\nu}$, sets of data at different N_S should collapse onto each other.

As another observable, relevant for the location and identification of the transition, the Binder cumulant [102] of the order parameter has been considered. For a generic observable X, the Binder cumulant is defined as

$$B_4(X) \equiv \frac{\big\langle (X - \langle X \rangle)^4 \big\rangle}{\big\langle (X - \langle X \rangle)^2 \big\rangle^2} \, , \tag{5.8}$$

In the thermodynamic limit $V \to \infty$, the Binder cumulant is a step function and takes different values depending on the nature of the phase transition (see Table 5.1). At finite

volume, instead, the Binder cumulant becomes a smooth function whose slope increases with N_S. In the vicinity of the critical coupling β_c, moreover, the Binder cumulant shows a scaling behavior, becoming a function of $(\beta - \beta_c)N_S^{1/\nu}$ only. As already seen for the susceptibility, once again, in a plot of the Binder cumulant B_4 *vs* $(\beta - \beta_c)N_S^{1/\nu}$, if the critical exponents, as well as the critical coupling, are set to the correct values, sets of data at different N_S collapse onto each other. Notice that, in this case, the N_S dependence appears in the scaling variable only.

Moreover, in the Taylor expansion of the Binder around $\beta = \beta_c$, the leading finite-size corrections are given by

$$B_4(\beta, N_S) = B_4(\beta_c, \infty) + a_1\,(\beta - \beta_c)N_S^{1/\nu} + a_2\,((\beta - \beta_c)N_S^{1/\nu})^2 + \dots\ . \tag{5.9}$$

Toward the thermodynamic limit, the intersection of Binder cumulants for different N_S gives β_c and the critical exponent ν takes its universal value, unveiling the type of transition according to Table 5.1.

We observe that, at the critical value $\mu_I = \pi\,T$, the Binder cumulant is close to 3 (1) for low (high) temperatures.

Following the same strategy as in [94], the distribution of the order parameter along with all the relevant cumulants, around the critical coupling β_c, are measured on a set of different κ values. Once identified the critical coupling from the crossing point of Binder cumulants of $L_{\rm Im}$ at various lattice sizes, or from the peak of the susceptibility of $\|L\|$, a first hint on the order of the transition is obtained by looking at the susceptibility and Binder collapse plots. The actual value of the critical exponent ν is, however, finally extracted out of a fitting procedure applied to the Binder cumulant by using Eq. (5.9). Afterwards, the location of the tricritical κ values is identified by looking at the behavior of ν while κ is varied.

Simulations have been performed at the fixed temporal lattice extent $N_T = 6$ ($a\mu_I = \pi/6$) and for 3-4 different N_S, for 9 values of the bare quark masses between $\kappa = 0.1$ and $\kappa = 0.165$. A minimal aspect ratio of almost 3 has been kept in the choice of N_S. An adequate number of couplings β around the critical one have been considered and for each β 40k up to 500k standard (unit length) HMC [34] trajectories have been collected (and on each of them the relevant observables have been measured) after at least 5k trajectories of thermalization. In each run the acceptance rate was tuned to $\sim$75%. The statistics for each κ, N_S, β has been accumulated almost always in 4 different Markov chains and this allowed us to judge, based on the overlap in the determinations

of observables for each single chain, weather our sample was wide enough. Ferrenberg-Swendsen reweighting [103] was used as a smoothing tool for our data or/and to add some new β to our sets.

All numerical simulations have been performed by use of the *publicly available* OpenCLbased code CL^{2}QCD [104][1], optimized to run efficiently on GPUs.

5.3 Results

According to the just outlined strategy a first hint on the order of the transition can be obtained by the collapse plots produced, for the susceptibility of the norm of the Polyakov loop, $\|L\|$, and for the Binder cumulant of L_{Im}, measured at fixed mass, and various couplings and spatial volumes, for all considered masses. This analysis requires an as precise as possible determination of the critical coupling to be extracted, respectively, by the susceptibility peaks, or by the crossing of the Binder cumulant for various lattice sizes.

Although large statistical errors and the similarity in the ratio γ/ν of critical exponents for tricritical and 3D Ising (second order) universality classes can make the collapse plot analysis inconclusive, it is usually accurate enough, especially for the Binder cumulant, to discriminate at least between first and second order phase transitions. Examples of collapse plots are given in Fig. 5.5 and Fig. 5.6.

In the thermodynamic limit a plot of ν *vs* κ, in presence of two tricritical points $m^{\mathrm{tric}}_{light}, m^{\mathrm{tric}}_{heavy}$ ($\nu = 0.5$), would be a rectangular function ($\nu = 0.6301$ for $m^{\mathrm{tric}}_{light} < m < m^{\mathrm{tric}}_{heavy}$, $\nu = 0.3$ for $m < m^{\mathrm{tric}}_{light}$ and $m > m^{\mathrm{tric}}_{heavy}$). However, at finite lattice volume, the rectangular profile is smoothed out and ν can take any value in between the universal ones.

That is why, beyond the qualitative picture provided by the collapse plot analysis, a quantitative determination of the critical indices calls for a different kind of analysis: the fit of the Binder cumulant data according to Eq. (5.9) is adequate in this sense, since it provides both the critical coupling and the ν exponent as a fits parameters, together with an estimate of the value of the Binder cumulant at the critical coupling in the thermodynamic limit $B_4(\beta_c, \infty)$.

Again in Fig. 5.7 an example of such analysis is given.

[1] Which is now available at github.com/CL2QCD

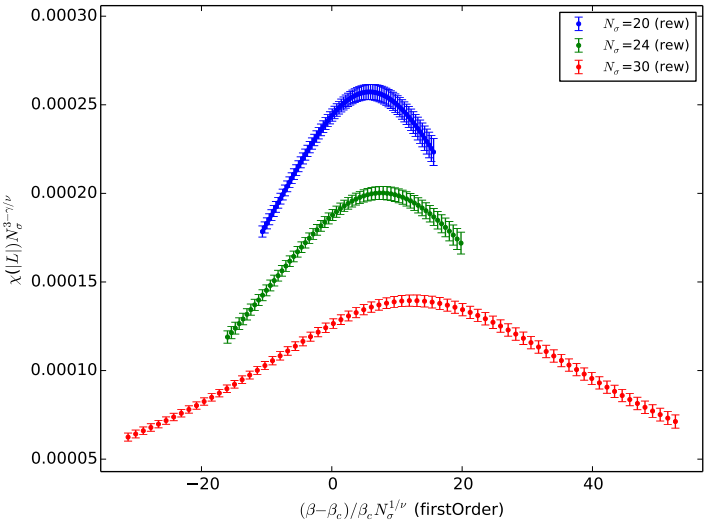

(A) First order coefficient $\nu = 1/3$.

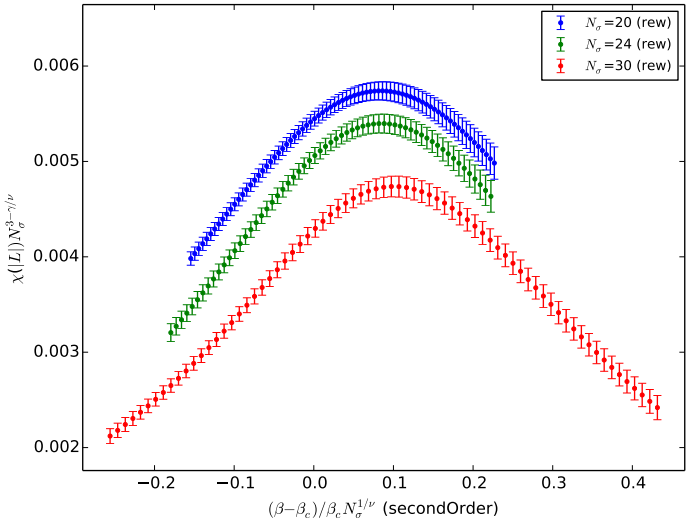

(B) Second order coefficient $\nu = 0.6301$.

FIGURE 5.5: Example of collapse plots of the susceptibility of the square norm of the Polyakov loop, for $\kappa = 0.13$.

In agreement with what found in previous studies both with staggered fermions [99] and with Wilson fermions [94], also here it has been found that large finite volume corrections push $B_4(\beta_c, \infty)$ to slightly higher values, than the universal one.

However, the application of the described fitting procedure to all the simulated κ values allows us to draw the ν *vs* κ plot from which the approximate position of the tricritical κ values can be inferred. Such result is shown in Fig. 5.8.

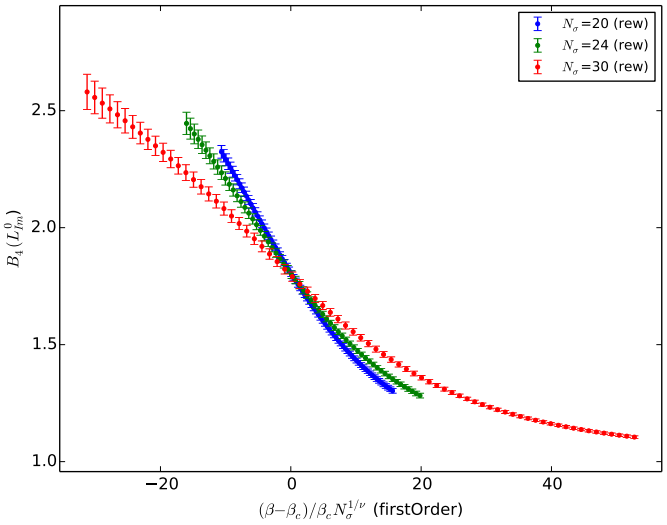

(A) First order coefficient $\nu = 1/3$.

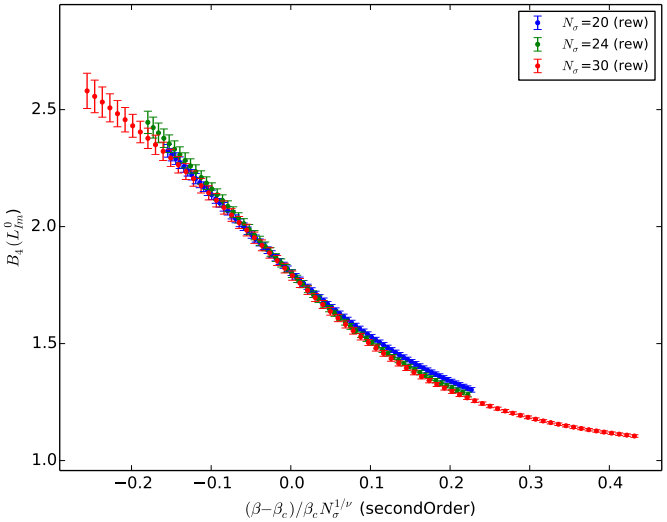

(B) Second order coefficient $\nu = 0.6301$.

FIGURE 5.6: Example of collapse plots of the Binder cumulant of the imaginary part of the Polyakov loop, for $\kappa = 0.13$.

In this study, up to current results, the tricritical κ values are found to be

$$\kappa_{\text{heavy}}^{\text{tric}} = 0.110(10) \qquad \text{and} \qquad \kappa_{\text{light}}^{\text{tric}} = 0.1625(25)\,, \tag{5.10}$$

The error on the $\kappa_{\text{light}}^{\text{tric}}$ is estimated so that the range around the best estimate extends within κ values for which the critical index ν was clearly indicating a first order, rather than second order, phase transition. For what concerns $\kappa_{\text{heavy}}^{\text{tric}}$, for one of the simulated masses, the extracted ν was compatible within one standard deviation with the one characterizing the tricritical universality class. We have used that κ for our best estimate

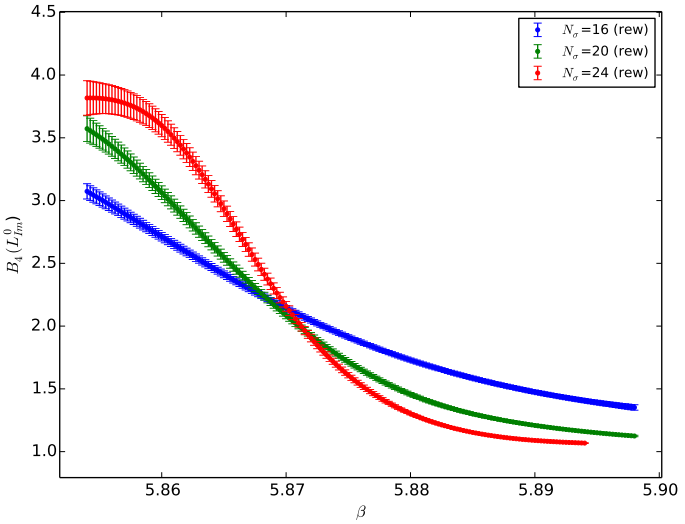

FIGURE 5.7: Plot of the Binder cumulant of the imaginary part of the Polyakov loop, for $\kappa = 0.1$ and $N_S = 16, 20, 24$. The multibranch fit according to the linear part of the fit ansatz in Eq. (5.9) for $\beta_c = 5.8698$ gives: $\nu = 0.4285 \pm 0.0313$, $B_4(\beta_c, \infty) = 2.1406 \pm 0.0270$, $a_1 = -0.0885 \pm 0.0435$ with reduced chi-square $\chi^2_r = 1.034745$ and quality $Q = 41.51\%$. The β ranges, at fixed N_S for which the fit is realized are chosen to be as overlapping with each other as possible and as symmetric as possible around the β_c.

and the quoted error coincides with the resolution in κ at which the simulations where performed.

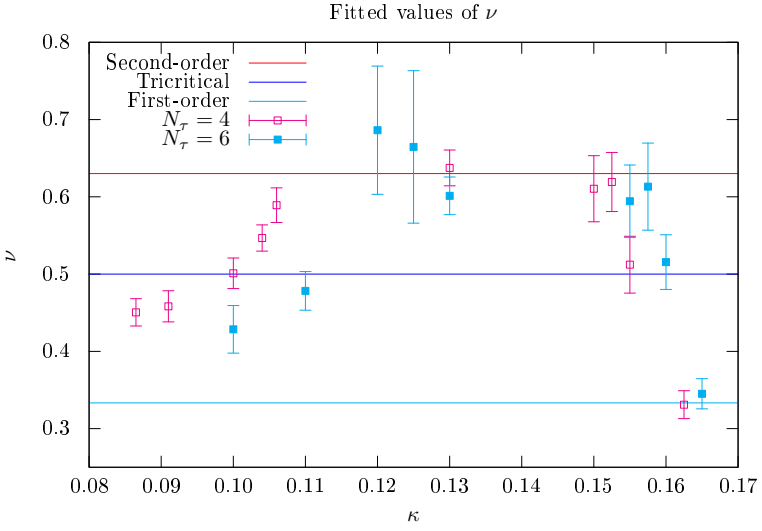

FIGURE 5.8: Critical exponent ν as function of κ. The horizontal lines are the critical values of ν for the relevant universality classes. This plot comes from Ref. [95] and includes data from Ref. [94] obtained on $N_T = 4$ lattices.

5.4 Summary and outlook

This work is placed in the context of the research line investigating the peculiar phase structure observed for QCD (here, in particular, $N_f = 2$ QCD) at imaginary values of the quark chemical potential and, precisely, at the critical values $\mu_I^c/T = (2k+1)\pi/N_c$, with $N_c = 3$ and $k \in \mathbb{Z}$, of such potential. Many previous studies in this direction were carried out using the staggered discretization for fermions. In the present work, the study made in [94], employing Wilson, rather than staggered, fermions, is repeated on a finer lattice (N_τ=6, instead of N_τ=4).

It is a meaningful extension since a continuum scaling analysis is needed to verify the reliability, beyond cut-off effects, of the scenario with first order RW endpoint both for heavy and light quarks. The final aim is then to take a step forward toward the possibility of extrapolating finite lattice size results to the continuum limit. It is however, not the last step in that direction: the lattice spacing will have to be further reduced, and more and more expensive simulations will be required, in order to get fully quantitative predictions.

Costs will grow, not only because of the growing lattice size, but also because of the already observed shift in the position of the tricritical points, toward smaller masses.

As for the current investigation, it is being extended by an estimation of the pion mass m_π at the light tricritical point. Such a measurement is needed to quantify the mass shift of the light tricritical point, with respect to previous findings.

Chapter 6

Numerical study of 2D $U(N)$ and $SU(N)$ spin models

In what follows we are going to deal with 2D $U(N)$ and $SU(N)$ spin models and with manifestations in these models of *Berezinskii-Kosterlitz-Thouless* (BKT) phase transitions. As already stated in Chap. 1, BKT transitions can take place, in some low dimensionality systems, despite a symmetry breaking in those systems is forbidden by the energetics of the system itself. Their main characteristic is an essential singularity in the thermodynamic potential, while its derivatives of whatever order are continuous. The mechanism behind such an infinite order transition is understood to be the unbinding of topological objects [105–107].

It is, in particular, argued that 2D $SU(N)$ spin models may posses two BKT phase transitions with an intermediate phase resembling the massless low-temperature phase of the 2D XY model. This expectation is justified by Berezinskii-like calculations of the two-point correlation function in $SU(N)$ spin models and, for $U(N)$, by the symmetry argument that the corresponding action has a $U(1)$ global symmetry which cannot be broken spontaneously in two dimensions. The problem of identifying BKT transitions and their universality character in spin models can be faced both analytically via, for instance, Kosterlitz-Thouless RG techniques and numerically via Monte Carlo simulations of such spin models. We were concerned with the latter case. Analytical prediction were taken as input for a purely numerical investigation.

Moreover, the motivation for studying 2D spin models is at least twofold: beyond being interesting on their own as models of magnetism, there is a direct match between transitions in 2D spin model with global symmetry group G and deconfinement phase transition in 3D Lattice Gauge Theory (LGT) with periodic boundary conditions and gauge group G. It was indeed conjectured by Svetitsky and Yaffe in 1982 [108] that if

continuous phase transitions are met in the former, then the deconfinement transition in the latter will belong to the same universality class of the order/disorder transition in the corresponding spin model.

The first two sections in this chapter, Sec. 6.1 and Sec. 6.2, will be devoted to clarify why one looks for BKT-type transitions in 2D spin models and what are the main characteristics of such transitions. The numerical setup and the observables measured in our numerical investigations are discussed in Sec. 6.3. Sec. 6.4 contains our results on evidences for BKT phase transitions both in $U(2)$ and in $SU(N)$ ($N = 5, 8$) spin models and our conclusions are drawn in Sec. 6.5.

What follows is mainly based on [109].

6.1 2D models

The ultimate goal in our investigations about spin models is to establish their phase diagram identifying all possible phases and the nature of transitions among them. The degrees of freedom and the interactions (hence the symmetry) of our spin models being the same, still the existence and nature of phase transitions in that model depends on its dimensionality. That is where the concepts of *lower critical dimensionality* and *upper critical dimensionality* come from. To be more specific the *upper critical dimensionality* is the number of dimensions of the models beyond which the mean field theory gives a correct description of the critical phenomena for that system. We are however more interested in the *lower critical dimensionality* that defines the lowest possible dimension for a given model to show a long-range order phase at nonzero finite temperature. As the spatial dimensionality d of a spin model decreases, the energetic of that system changes favoring the entropy over the energy in the free energy cost of introducing more disorder in the model. The reason is simply that the number of neighbor degrees of freedom involved in the interaction is reduced, with the dimensionality weakening the effect of the interaction itself. The *lower critical dimensionality* depends not only on the interactions in the partition function for the system (and in what follows we only consider models of short range interactions), but also on whether the degrees of freedom and symmetries are discrete or continuous. In the former case, the so called *Peierls argument* can be used to determine the *lower critical dimensionality*, in the latter case the *Mermin-Wagner theorem* applies.

As an example of applications of the Peierls argument, we can consider the 1D Ising model and the free energy cost, given the fully aligned ground state of the system, of introducing a kink configuration that breaks only one bond in the chain and gives the

lowest excited state. To such flip it corresponds a finite positive variation in the energy of the system due to the broken bond at the domain wall. On the other hand we can have as many kink configurations as possible positions for the domain wall, i.e. $N-1$ in a system of N spins: the corresponding variation in entropy is $k\ln(N-1)$ so that for sufficiently large N and all $T \neq 0$ we have $\Delta F < 0$ and any disordered excited state is energetically favored. The long-range ordered state is easily destroyed at any arbitrarily small temperature.

Analogous considerations on the stability of a state with a spontaneous magnetization, can be made for the 2D Ising model. In this case, however, the energy cost corresponding to the creation of a domain of flipped spins starting from the fully aligned ground state amounts to $\Delta E = 2JL$, where J is the coupling of the nearest-neighbor interaction and L is the perimeter of the flipped domain. Again, to estimate the entropy variation, one has to consider the many possible positions and shapes of the flipped domains. For this we can think of the domain-contour formation as a non-backtracking random walk in which, to each step it corresponds a number $\mu < 3$ (the contour as to be a closed polygon in the end) of possible choices of direction. The corresponding variation of the free energy is then $\Delta F = L(2J - kT\mu)$. Even though, for sufficiently low temperatures, the ordered phase is stable against the formation of domains of flipped spins of whatever perimeter, there is a critical temperature, precisely $T_c \simeq 2.269J/k$, above which the disordered phase becomes energetically favored.

While for the Ising model the *lower critical dimensionality* is $d_l = 1$, for most system characterized by a continuous symmetry the fluctuations that brings the system into a disordered phase are more severe because the order parameter can change its direction more easily with little cost in free energy and one finds $d_l = 2$. This is the result of the already mentioned *Mermin-Wagner theorem*. In terms of domain walls formation, an heuristic argument can also be given. In this case we can think about the formation of a domain of size l, but with the involved spin having a distance $\mathcal{O}(l)$ over which to relax in a way that the spins near the centre of the domain point in the opposite direction from those away from the centre. Being continuous, the relative angle between neighboring spins will be $\mathcal{O}(1/l)$, the energy density will be quadratic in the relative angle $\mathcal{O}(1/l^2)$ and the whole volume of the domain $\mathcal{O}(l^d)$ has to be taken into account (instead of $\mathcal{O}(l^{d-1})$ as in the discrete case). As a result, the entropic effects are dominant for $d \leq 2$. The long-range order of system with continuous degrees of freedom and symmetries such as the XY model is, hence, absent at finite temperature in $d = 2$.

BKT transition in 2D XY model

The 2D XY model, also known as planar Heisenberg model, is a model of two-component classical spins (S_x, S_y) normalized to unit length $S_x^2 + S_y^2 = 1$. Nearest-neighbor interactions between the spins are encoded in the partition function of the model, which is given by

$$Z = \int \prod_i \frac{d\theta_i}{2\pi} \exp\Big[\beta \sum_{\langle ij \rangle} \cos(\theta_i - \theta_j)\Big], \tag{6.1}$$

where $\beta = 1/(k_B T)$ and spin variables are described by angles defined modulo 2π. The interaction is ferromagnetic: it favors configurations of equal θ_i's. The corresponding global rotational symmetry is $O(2)$, or $U(1)$ in terms of the θ_i's variables that are continuous and can be all translated of the same amount $\theta_i \to \theta_i + \alpha$ leaving the model invariant. According to the arguments given in the previous section, the XY model in two dimensions, because of its continuous degrees of freedom and symmetry, does not display macroscopic spontaneous magnetization (long-range order) at any finite temperature. However, the XY model in two dimensions undergoes the peculiar BKT phase transition at a finite nonzero critical temperature. The main characteristics of such a transitions are that:

- There is no spontaneous symmetry breaking;
- There is no non-analyticity neither in the free energy nor in any of its derivatives;
- Correlation length shows an *essential singularity* in the vicinity of the critical point where it diverges exponentially.

From low(high)-temperature expansions it can be observed that, in the high-temperature phase, correlation function falls off exponentially in the distance between any two spins. On the other hand, a low-temperature phase exists in which the use of a spin-wave (Gaussian) approximation unveils a power-law decay for correlation functions with distance, which is reminiscent of what happens at the critical point of an ordinary Landau-type phase transition, just as if every temperature below a critical one was critical on its own. It is then said that although the model does not display long-range order at any finite nonzero temperature, it does show a *quasi-long-range order* over a finite temperature range $0 < T < T_c$.

To be more specific, in the low-temperature phase of the model, the absence of significant thermal fluctuations and the ferromagnetic nature of the interaction suggest that $\theta_i - \theta_j$ is small enough to approximate the cosine in Eq. (6.1) to second order. Moreover our interest in the large-scale behavior of the system allows us to switch to the continuum,

where the effective Hamiltonian of our system, reads

$$H \approx -\beta \sum_{\langle ij \rangle} \Big(1 - \frac{1}{2}(\theta_i - \theta_j)^2\Big) \approx -\frac{\beta}{2} \int d\mathbf{r} (\nabla\theta)^{\mathbf{2}} \tag{6.2}$$

in the already mentioned spin-wave approximation, where the periodicity in the, now continuous, angular variables θ is irrelevant. It is obtained that the spin configurations which are stable under the spin wave approximation are the ones satisfying the Laplace equation of motion $\nabla^2\theta(\mathbf{r}) = \mathbf{0}$, hence in particular, the uniformly rotated state within given boundary conditions. The correlation function in this approximation is found to decay according to a power law

$$\Big\langle e^{i(\theta(\mathbf{r})-\theta(\mathbf{0}))} \Big\rangle = \Big\langle \cos\Big(\theta(\mathbf{r}) - \theta(\mathbf{0})\Big) \Big\rangle \approx r^{1/2\pi\beta}, \tag{6.3}$$

with a non-universal exponent depending explicitly on the temperature.

In the high-T regime, instead, the correlation function behaves as

$$\Big\langle e^{i(\theta(\mathbf{r})-\theta(\mathbf{0}))} \Big\rangle \approx e^{-|n|\ln\beta}. \tag{6.4}$$

Consistently with the observation of such a disordered high-T phase, it must happen that the angle variables vary in a more pronounced way, with growing temperature, and the spin-wave approximation breaks. In this sense, one observes that the Laplace equation also admits topological vortex solutions that are singular in the continuum and cannot be taken into account within the spin-wave approximation. These vortex configuration are able at a critical temperature value to destroy the quasi-long-range order of the model.

To see this, one considers a vortex spin configuration of winding number $q = 1$, i.e. satisfying $\oint \nabla\theta \cdot d\mathbf{l} = \mathbf{2}\pi$. A plausibility argument by Kosterlitz and Thouless suggests that vortices can drive the phase transition with the ground state of the model for $T > T_c$ being a vortex condensate. The argument is based on the evaluation of the energy variation corresponding to a vortex configuration with respect to the ground state configuration, which is

$$\Delta E \simeq \pi \ln\left(\frac{R}{a}\right), \tag{6.5}$$

where R is the linear size of the 2D system, while a is the lattice spacing. Thus the vortex energy has a divergence in the limits $a \to 0$ and $R \to \infty$. Now the free energy variation induced by the presence of a vortex can be estimated knowing that the entropy is just the logarithm of the multiplicity of available vortex configurations, i.e. the number of

sites of the system. Therefore,

$$\Delta F = (\pi - 2\beta)\ln\left(\frac{R}{a}\right). \tag{6.6}$$

There exist, hence, a critical temperature value $T_c = \pi/2k_B$ for which $\Delta F = 0$ and for any $T \geq T_c$, as a consequence, the vortex formation is energetically favored. It is just the competition between the logarithmic dependence on the system size of both the energy and entropy, that makes possible a vortex unbinding transition. The nature and mechanism behind such a peculiar phase transition, already discussed by Berezinskii, was identified by Kosterlitz and Thouless in 1973 [105–107]. The Kosterlitz-Thouless picture predicts power-law decay of the spin-spin correlation function at low-T when the only relevant configurations are spin waves and bound states of vortex-antivortex pairs that affecting spins only over small regions hence leaving the system ordered until, at $T = T_c$, the size of the vortex-antivortex bound diverges. Beyond T_c the ground state is a vortex condensate, the model is disordered and the spin-spin correlation functions falls off exponentially.

6.2 BKT phase transitions in non-Abelian spin models

The interaction in a model of non-Abelian spins defined onto a 2D lattice Λ is described by the partition function

$$Z(\beta, N) \;=\; \int \prod_x dW(x) \exp\left[\beta \sum_{x,n} \mathrm{Re}\mathrm{Tr}W(x)\mathrm{Tr}W^{\dagger}(x+e_n)\right], \tag{6.7}$$

where $x = (x_1, x_2) \in \Lambda$, $n = 1, 2$ and e_n is a unit vector in n-th direction. The matrices $W(x)$ are elements of either $U(N)$ or $SU(N)$ group and we suppose that the trace in the Boltzmann weight is taken in the fundamental representation and is normalized by $1/N$. Then, in the diagonal representation for $W(x)$ the action for both $U(N)$ and $SU(N)$ has the form

$$\mathrm{Re}\mathrm{Tr}W(x)\mathrm{Tr}W^{\dagger}(x+e_n) \;=\; \frac{1}{N^2}\sum_{i,j=1}^{N} \cos\left[\omega_i(x) - \omega_j(x+e_n)\right]. \tag{6.8}$$

The invariant measure for $U(N)$ is given by

$$\int dW \;=\; \int_0^{2\pi} D(\omega)D^{\star}(\omega) \prod_{k=1}^{N} d\omega_k \,, \tag{6.9}$$

where

$$D(\omega) \;=\; \prod_{k<l} \left(e^{i\omega_k} - e^{i\omega_l}\right) \;. \tag{6.10}$$

The $SU(N)$ measure coincides with $U(N)$ one up to additional constraint

$$\prod_{k=1}^{N} \exp[i\omega_k] = 1 \;, \tag{6.11}$$

which is implemented into the partition function Eq. (6.7) with the help of the periodic delta-function

$$\sum_{n=-\infty}^{\infty} \exp\left[in \sum_{k=1}^{N} \omega_k\right] \;. \tag{6.12}$$

Due to this constraint, the $SU(N)$ model is invariant only under global discrete shift $\omega_k(x) \to \omega_k(x) + \frac{2\pi n}{N}$ for all k and x. This is just global symmetry under transformations in the center of the $SU(N)$ group which is constituted by $Z(N)$ transformations.

The partition function Eq. (6.7) can be regarded as the simplest effective model for the Polyakov loops which can be derived in the strong coupling region of $3D$ $SU(N)$ LGT at finite temperature. The full effective model is more complicated including summation over all representations, but the expectation is that if there is a BKT-type phase transition at large N it should manifest itself even in this simple model.

Hints on the existence in the introduced models of BKT phase transitions are to be found in the behavior of the two-point correlation function given by

$$\Gamma_N(\beta, R) \;=\; \frac{1}{N^2} \sum_{i,j=1}^{N} \cos\left[\omega_i(0) - \omega_j(R)\right] \;, \tag{6.13}$$

respectively in the weak and strong coupling regime. When β is sufficiently small one can use the conventional strong coupling expansion to demonstrate the exponential decay of the correlation function.

To compute the correlation function at large β one has to adapt an argument by Berezinskii [106]. In the context of $SU(N)$ model this means applying two approximations. First, we replace the cosine function in the Boltzmann weight by its Taylor expansion since, when β grows system becomes more and more ordered. Second, the invariant measure $D(\omega)D^{\star}(\omega)$ is treated as a smooth function. Calculations lead to the identification of two possible cases:

- $\beta \ll N^2$ in which case only small n_x matter in the overall sum. Then we can estimate $\Gamma_N(\beta, R)$ by calculating the $n_x = 0$ component of the sum,

$$\Gamma_N(\beta \ll N^2, R) \;=\; \frac{1}{Z}\;\exp\left[-\frac{1}{2\beta}\,(2G(0) - 2G(R) - 1)\right] \sim R^{-\frac{1}{2\pi\beta}}\;. \qquad (6.14)$$

  Thus, in this case correlation functions decays with a power law.

- $\beta \gg N^2$. In this case we may replace summation over n_x by integration. Using the Poisson summation formula and neglecting exponentially small terms one finds

$$\Gamma_N(\beta \gg N^2, R) \sim \;\frac{1}{Z}\exp\left[\frac{1}{2\beta}\right]\;. \qquad (6.15)$$

  As is seen, in this case the correlation function remains constant at large distances what is clear signal of the spontaneous symmetry breaking.

Thus, similar to $2D$ $Z(N)$ vector Potts models, $SU(N)$ spin models should possess an intermediate phase when $1 \ll \beta \ll N^2$ which is characterized by the power-like decay of the correlation function.

To get to the actually simulated model, a dual formulation of the spin model corresponding to the partition function in Eq. (6.7) has been built and the partition function of the dual model has then been found to be equivalent, for the specific case of a $U(2)$ spin model, to

$$Z(\beta, N=2) \;=\; \int_0^{2\pi} \prod_x \frac{d\omega(x)}{2\pi} \int_0^1 \prod_x (1-t^2(x))^{1/2}\, dt(x)$$
$$\exp\left[\beta \sum_{x,n}\; t(x)t(x+e_n)\cos(\omega(x) - \omega(x+e_n))\right]\;. \qquad (6.16)$$

written on the original lattice. This is the partition function we have considered and implemented for our investigations of the $U(2)$ spin model, where $t(x)$ variables are $SU(2)$ characters restricted to positive values, i.e. real numbers in the range $[0, 1]$ (and it can be numerically verified that extending the range to $[-1, 1]$ while keeping $\omega(x)$ variables "frozen" the features of $SU(2)$ spin models are reproduced), while $\omega(x)$ variables are angular variables in $[0, 2\pi]$ (and it can be numerically verified that our model reproduce a $U(1)$ spin model for "frozen" $t(x)$ variables).

For what concerns investigations of $SU(N)$ spin models with N as large as 5 and 8, the starting point has been again Eq. (6.7). However a further interaction term has been included in a way that we have investigated $SU(N)$ model with both fundamental and "adjoint spins" in the space of two independent coupling constants. Once defined the

"adjoint" $SU(N)$ spin as

$$U(x) = \mathrm{Tr}W(x)\mathrm{Tr}W^{\dagger}(x) = \sum_{i,j=1}^{N} \cos(\omega_i(x) - \omega_j(x)), \tag{6.17}$$

which is $Z(N)$ invariant, the interaction term in adjoint representation reads

$$\lambda \sum_{x,n} U(x)U(x+e_n) \tag{6.18}$$

and has to be included in the Boltzmann factor in Eq. (6.7). The role of this interaction term, is to enhance the tunnelling between $Z(N)$ center sectors. The full partition function in this case is

$$Z(\beta, N) \;=\; \int \prod_x dW(x) \exp\left[\beta \sum_{x,n} \mathrm{ReTr}W(x)\mathrm{Tr}W^{\dagger}(x+e_n) + \right. \\ \left. + \lambda \sum_{x,n} U(x)U(x+e_n)\right] . \tag{6.19}$$

6.3 Observables and simulation setup

2D $U(2)$ spin models

To study the existence and nature of phase transitions in our $U(2)$ spin model, a code has been written which implements a cluster algorithm for the update of $\omega(x)$ variables and a heatbath algorithm for the update of $t(x)$ variables. The model is studied on a square $L \times L$ lattice Λ with periodic BC. Simulations were carried on for many different lattice sizes, $L = 16, 32, 64, 96, 128, 160, 192, 256, 384, 512, 768, 1024$, in order to allow for a finite size scaling (FSS) investigation of the identified transitions. The exponential divergence of the correlation length in a BKT transition implies a very slow, logarithmic convergence to the thermodynamic limit in the vicinity of the transition. As a consequence, very large volumes are required in order to enter the scaling region and safely extract critical indices. The partition function for this model is given in Eq. (6.16). For each run we have ensured thermalization by discarding 50k configurations and then produced 10^6 configurations with measurements taken after 10 updating steps. The resolution in β of our simulation is of 0.005. The observables we have considered are:

- Complex magnetization $M_L = |M_L|e^{i\psi}$ defined as

$$M_L = \frac{1}{L^2} \sum_{x \in \Lambda} s(x) = \frac{1}{L^2} \sum_{x \in \Lambda} t(x) e^{i\omega(x)} \tag{6.20}$$

- Magnetic susceptibility

$$\chi_L^{(M_L)} = L^2\Big(\langle M_L^2 \rangle - \langle M_L \rangle^2 \Big) \tag{6.21}$$

- Binder cumulant

$$U_L^{(M_L)} = 1 - \frac{\langle |M_L|^4 \rangle}{3\langle |M_L|^2 \rangle^2}, \qquad \text{or} \qquad B_4^{M_L} = \frac{\langle |M_L|^4 \rangle}{\langle |M_L|^2 \rangle^2} \tag{6.22}$$

- Second-moment correlation length defined as

$$\xi_2 = \frac{1}{2\sin(\pi/L)} \Big(\frac{\chi}{F} - 1 \Big)^{1/2}, \tag{6.23}$$

  where $\chi = \frac{1}{L^2} \sum_x s(x)$, and

$$F = \frac{1}{L^2} \sum_{x,y} \langle s(x) s(y) \rangle \cos\Big(\frac{2\pi(y_1 - x_1)}{L} \Big) \tag{6.24}$$

  is the Fourier transform of the correlation function at the smallest non-vanishing momentum.

The statistical analysis of our data, for each of the above listed observables, has been accomplished by use of the jackknife method over bins at different blocking levels.

2D $SU(N)$ spin models: $N = 5, 8$

To study the existence and nature of phase transitions in $SU(N)$ spin model with $N = 5, 8$ a code has been written which implements both a cluster and a Metropolis algorithm for the update of $\omega_i(x)$. The cluster updates have to be alternated with Metropolis updates to achieve ergodicity, because the cluster algorithm would sample the center group $Z(N)$ only.

The model is studied on a square $L \times L$ lattice Λ with periodic BC. Simulations were carried on for many different lattice sizes, $L = 16, 32, 64, 96, 128$. For each run we have ensured thermalization by discarding 20k configurations and then produced $10 - 20$k configurations with measurements taken after 10 updating steps. The resolution in β of our simulation ranges from 0.1 to 0.5. The partition function for this model is given in Eq. (6.19).

The aim, in this second investigation of non-Abelian spin models, is simply that of checking whether BKT transitions can take place in such models. The observables we have considered are:

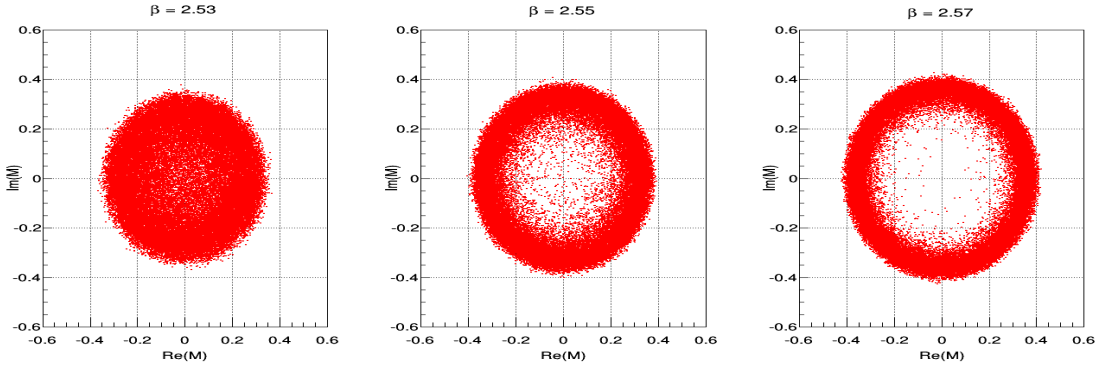

FIGURE 6.1: Scatter plots of the complex magnetization M_L at $\beta = 2.53, 2.55, 2.57$ in $U(2)$ on a 256^2 lattice.

- Complex magnetization $M_L = |M_L|e^{i\psi}$ defined as

$$M_L = \frac{1}{NL^2} \sum_{x\in\Lambda} \sum_{i=1}^{N} e^{i\omega_i(x)}; \tag{6.25}$$

- Real part of the rotated magnetization $M_R = |M_L|\cos(N\psi)$;

- Magnetic susceptibilities of M_L and M_R

$$\chi^{(M_{L,R})} = L^2 \Big(\langle M_{L,R}^2 \rangle - \langle M_{L,R} \rangle^2 \Big). \tag{6.26}$$

The statistical analysis of our data for each of the above listed observables has been accomplished by use of the jackknife method over bins at different blocking levels.

6.4 Numerical evidences for a phase transition

2D $U(2)$ spin models

The main aim of our numerical investigations is to check the existence of a BKT transition to a massless phase in our $U(2)$ model. If a similar transition is found to happen, then one has to locate it as precisely as possible and to check its universality character.

A clear indication of the two-phase structure is provided by scatter plots of the complex magnetization M_L at different values of β and all considered lattice sizes. Increasing β we observe a transition from a disordered phase, characterized by a uniform distribution around zero, and a massless phase, characterized by a "ring distribution". Such observation is reported in Fig. 6.1 and Fig. 6.2, respectively for $L = 256$ and $L = 512$.

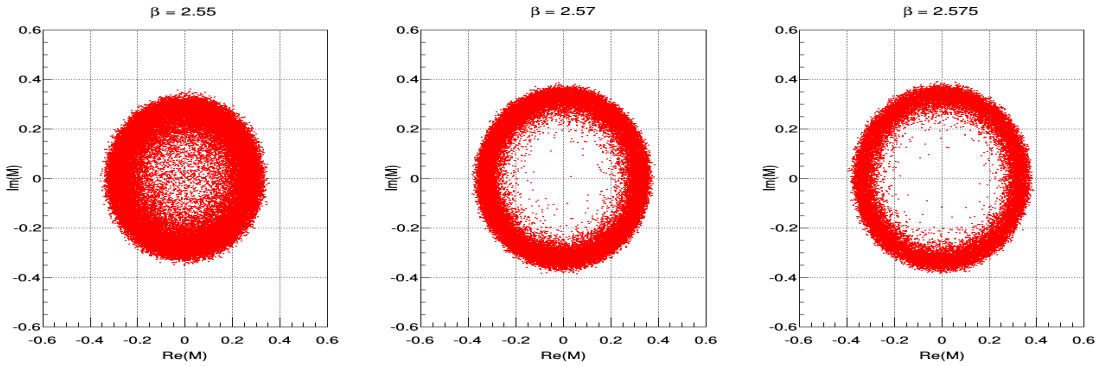

FIGURE 6.2: Scatter plots of the complex magnetization M_L at $\beta = 2.55, 2.57, 2.575$ in $U(2)$ on a 512^2 lattice.

The next step is the precise location of the phase transition, i.e. the identification of the critical coupling β_c. To accomplish this task, following [110, 111], we can make use of appropriate fit ansätze both for the second-moment correlation length and for the Binder cumulant *versus* the lattice size. The second-moment correlation length and the Binder cumulant in correspondence to a BKT transition are indeed found to be RG-invariant quantities and to take universal values that are known for the XY model [110, 111]. Also their FSS behavior has been studied within the 2D XY model providing us with the following ansätze:

- For the second-moment correlation length

$$\frac{\xi_2(\beta, L)}{L} = a(\beta) - \frac{b(\beta)}{\ln(L) + c(\beta)}, \tag{6.27}$$

  where $a_c = a(\beta_c) = 0.7506912\ldots$ and $b_c = b(\beta_c) = 0.212430\ldots$ at the critical point in XY model;

- For the Binder cumulant

$$B_4^{(M_L)}(\beta, L) = a(\beta) - \frac{b(\beta)}{\ln(L) + c(\beta)} + \frac{d(\beta)}{(\ln(L) + c(\beta))^2}, \tag{6.28}$$

  where $a_c = a(\beta_c) = 1.018192\ldots$ and $b_c = b(\beta_c) = 0.017922\ldots$ at the critical point in XY model, and also subleading logarithmic corrections are indicated since they are found to be important.

An example of the just discussed FSS behavior for the specific case of the second-moment correlation length is given in Fig. 6.3.

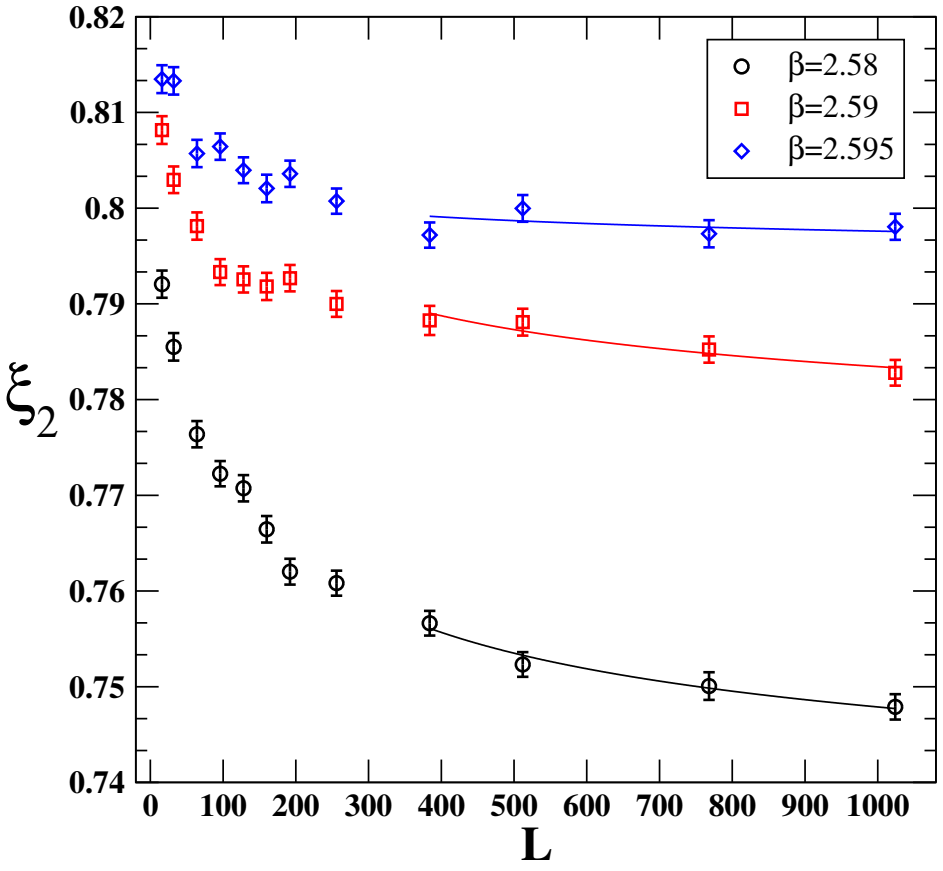

FIGURE 6.3: Second-moment correlation length ξ_2 as a function of the lattice size L, fitted to the universal ansatz $\xi_{2(\beta,L)}/L = a(\beta) - \frac{b(\beta)}{\ln(L)+c(\beta)}$. It is known that $\xi_2(\infty) = 0.7506912$.

To extract the critical point from the scaling of ξ_2 and $B_4^{(M_L)}$, with the lattice size L, the following methods are used:

- At each fixed value of β the fit of ξ_2 and $B_4^{(M_L)}$ data is performed, respectively via the ansatz in Eq. (6.27) or Eq. (6.28), fixing $b(\beta)$ to the known value b_c. An estimate of β_c is then given by the β-value at which $a(\beta) = a_c$;
- The same procedure as before, but fixing $a(\beta) = a_c$ and extracting β_c from the requirement that $b(\beta_c) = b_c$.

Our results are illustrated in Fig. 6.4 and Fig. 6.5, respectively for the second-moment correlation length and the Binder cumulant.

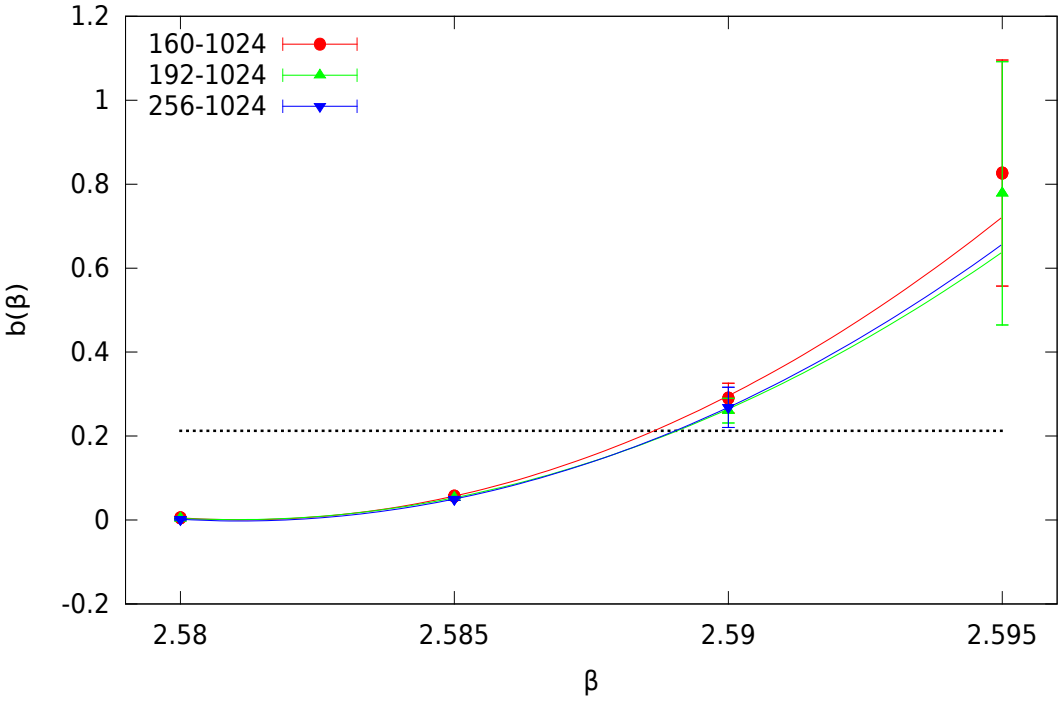

(A) Fit parameter $b(\beta)$ extracted from fits of ξ_2 via Eq. (6.27) fixing $a(\beta)$ to the known value $a_c = 0.7506912$. The horizontal red line marks the expected value b_c.

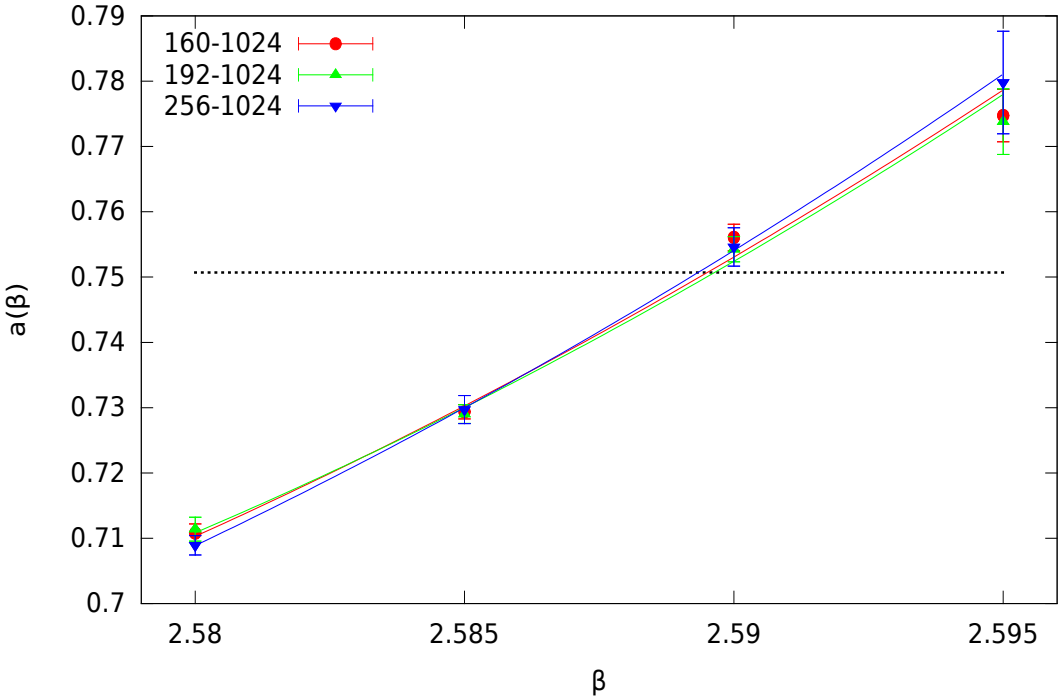

(B) Fit parameter $a(\beta)$ extracted from fits of ξ_2 via Eq. (6.27) fixing $b(\beta)$ to the known value $b_c = 0.2124300$

FIGURE 6.4: Determination of β_c from fits of the second-moment correlation length ξ_2 via Eq. (6.27). To be conservative one can quote $\beta_c = 2.59 \pm 0.005$. The horizontal red line marks the expected value a_c.

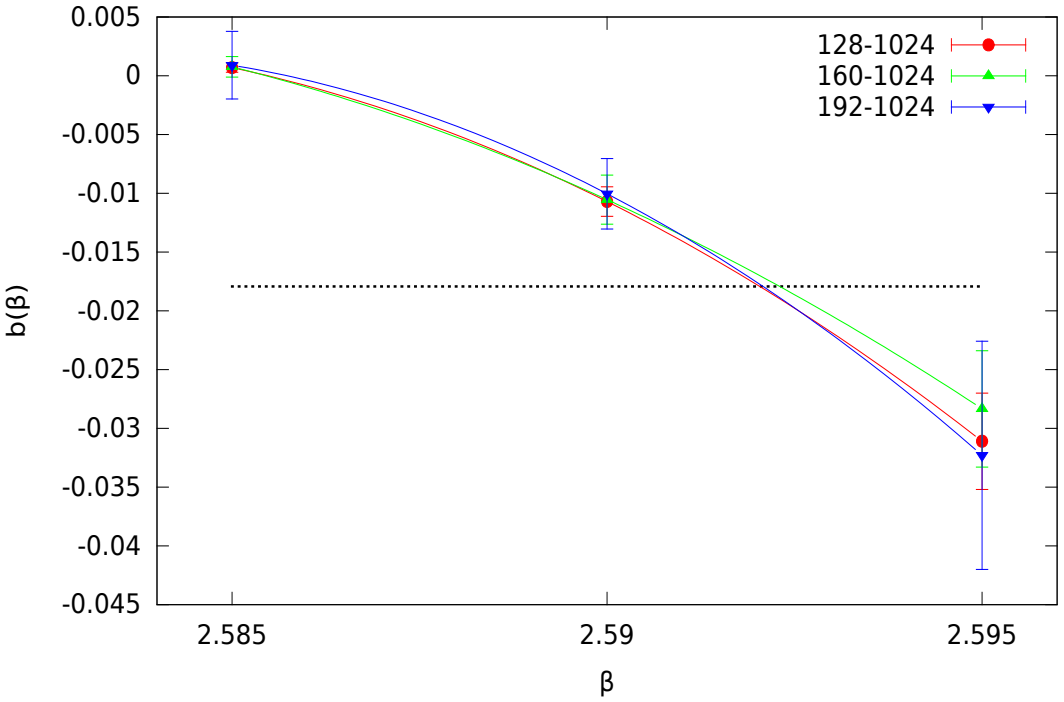

(A) Fit parameter $b(\beta)$ extracted from fits of ξ_2 via Eq. (6.28) fixing $a(\beta)$ to the known value $a_c = 1.018192$. The horizontal red line marks the expected value b_c.

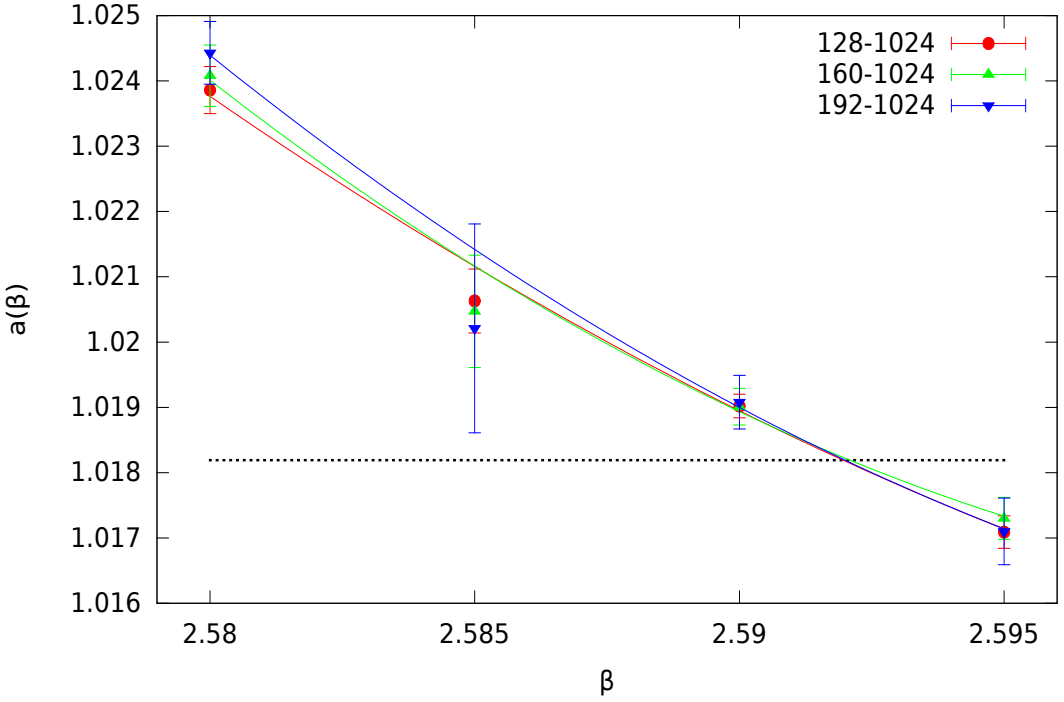

(B) Fit parameter $a(\beta)$ extracted from fits of ξ_2 via Eq. (6.28) fixing $b(\beta)$ to the known value $b_c = 0.017922$. The horizontal red line marks the expected value a_c.

FIGURE 6.5: Determination of β_c from fits of the second-moment correlation length ξ_2 via Eq. (6.28). To be conservative one can quote $\beta_c = 2.59 \pm 0.005$ also in this case.

TABLE 6.1: Fit parameters $a, -\beta/\nu, r$ obtained from fits of the magnetization via Eq. (6.29) realized over the size range $[L_{\min}, L_{\max} = 1024]$.

β_c	$L_{\min}$	a	$-\beta/\nu$	r	χ^2_r
2.59	64	0.71025 ± 0.00328	-0.12527 ± 0.00120	0.04307 ± 0.00659	1.20
2.59	96	0.70055 ± 0.00286	-0.12836 ± 0.00098	0.06119 ± 0.00556	0.35
2.59	128	0.70089 ± 0.00469	-0.12826 ± 0.00151	0.06055 ± 0.00879	0.42
2.59	160	0.70915 ± 0.00381	-0.12587 ± 0.00116	0.04596 ± 0.00690	0.15
2.59	192	0.70738 ± 0.00575	-0.12635 ± 0.00168	0.04900 ± 0.01018	0.18
2.59	256	0.70322 ± 0.01075	-0.12746 ± 0.00299	0.05600 ± 0.01854	0.24

TABLE 6.2: Fit parameters $a, \gamma/\nu$ obtained from fits of the magnetic susceptibility via Eq. (6.30) for $r = 0$, since including logarithmic corrections with r either free or fixed to $r = 0.125$ did not help improving our fits. Fit were realized over the size range $[L_{\min}, L_{\max} = 1024]$.

β_c	$L_{\min}$	a	γ/ν	χ^2_r
2.59	160	0.00293 ± 0.00010	1.73455 ± 0.00585	2.69
2.59	192	0.00282 ± 0.00010	1.74060 ± 0.00581	1.82
2.59	256	0.00273 ± 0.00013	1.74527 ± 0.00765	1.87
2.59	384	0.00249 ± 0.00005	1.75966 ± 0.00314	0.14
2.59	512	0.00241 ± 0.00003	1.76431 ± 0.00180	0.02

As a remark about the fitting procedure, one can observe that its stability, with respect to the volumes included in the fit, can be inspected by changing the range of lattice sizes included in the fit and by checking that the extracted fit parameters are compatible within errors once L is large enough. We have found that such a stability in the fits is achieved as soon as the lowest size considered in the fits is $L = 128 - 160$.

Once the critical coupling has been estimated, we are able to extract critical indices out of the FSS behavior at the critical coupling of[1]:

- The magnetization $|M_L|$ that is expected to satisfy the scaling law

$$|M_L| = aL^{-\beta/\nu}\ln^r L; \tag{6.29}$$

- The susceptibility $\chi_L^{(M_L)}$ that is expected to satisfy the scaling law

$$\chi_L^{(M_L)} = aL^{\gamma/\nu}\ln^r L; \tag{6.30}$$

Results are summarized in Table 6.1 and Table 6.2 for the case of magnetization and susceptibility respectively.

[1]The symbol β here denotes a critical index and not, as before, the coupling of the theory.

2D $SU(N)$ spin models: $N = 5, 8$

The main aim of this numerical investigations is to check the existence of a BKT transition to a massless phase in our $SU(N)$ model within a three-phase structure: from the disordered low-β phase, through a massless phase for $\beta_c^1 < \beta < \beta_c^2$, to an ordered high-$\beta$ phase. We did not try to neither to locate the transition, nor to check its universality character. What we have found is that the phase structure of our model significantly depend on the coupling λ of the interaction term.

A clear indication of the three-phase structure emerges from scatter plots of the complex magnetization M_L at different values of β and all considered lattice sizes only for $\lambda \geq 20$. Such observation is reported in Fig. 6.9 and Fig. 6.2. We observe how the nature and location(s) of the transition(s) is influenced by the intensity of the coupling corresponding to the interaction term in the adjoint representation:

- When the interaction term is switched off by setting $\lambda = 0$, no evidence for a three-phase structure or BKT transition is found. Only a strong, presumably first order, phase transition from a disordered to the ordered phase takes place at β as high as about 12;
- Also for nonzero coupling $\lambda < 20$ we were able to identify only two different phases with the value of the critical β-coupling β_c quickly decreasing;
- For $\lambda \geq 20$, however, a ring distribution of the ordinary magnetization M_L appears at intermediate β values, which is interpreted as the footprint for a BKT transition.

Beyond what scatter plots show us, further information about the nature of the observed transitions is provided by behaviors against β and for various fixed λ values, of the ordinary and rotated magnetization and their susceptibilities. A remark is in order about the necessity to introduce and measure the rotated magnetization [112]: what we need is a quantity that is sensitive to the difference in the magnetization distribution between the massless and ordered phase. However the two phases differ only for the angular structure of the complex magnetization, hence the susceptibility and even the Binder cumulant for the ordinary magnetization are not able to detect the massless-ordered transition. The rotated magnetization, instead, yields a finite value when there is a non-trivial angular structure, while it vanishes when ψ is isotropically distributed.

For what concerns the $SU(8)$ spin model, exactly the same kind of investigation was carried on and led to the results that also in that case a three-phase structure appears only for nonzero λ and, in particular starting from a $\lambda_{\min} \approx 64.00$ which is larger with respect to the $SU(5)$ case.

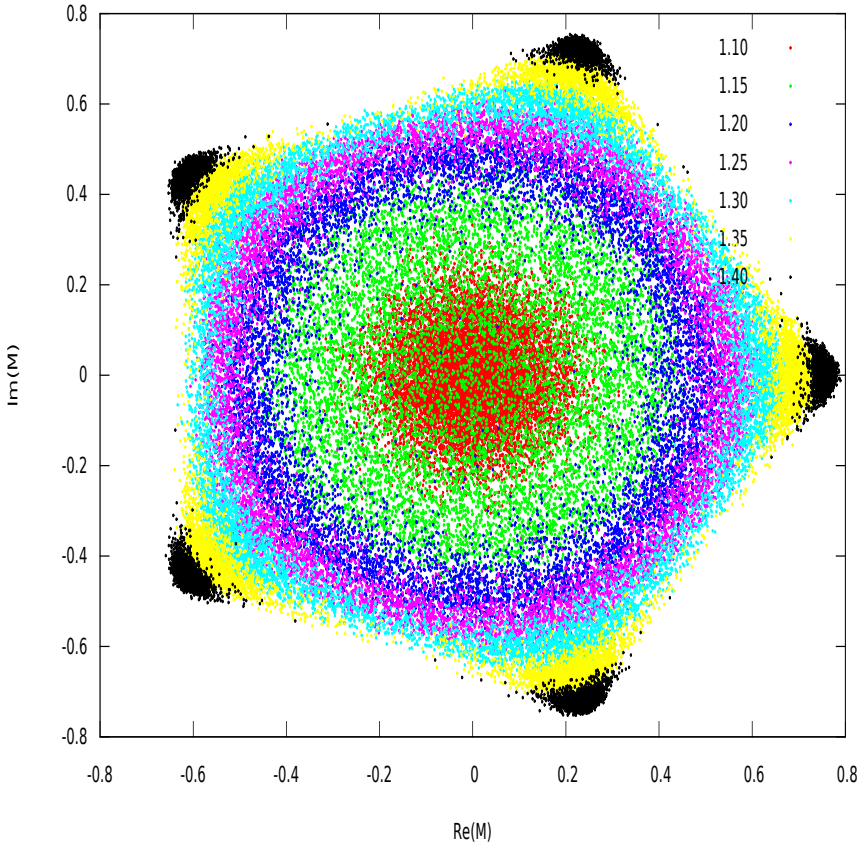

(A) $\lambda = 25.0$ and $\beta \in [1.10, 1.40]$ on a 128^2 lattice.

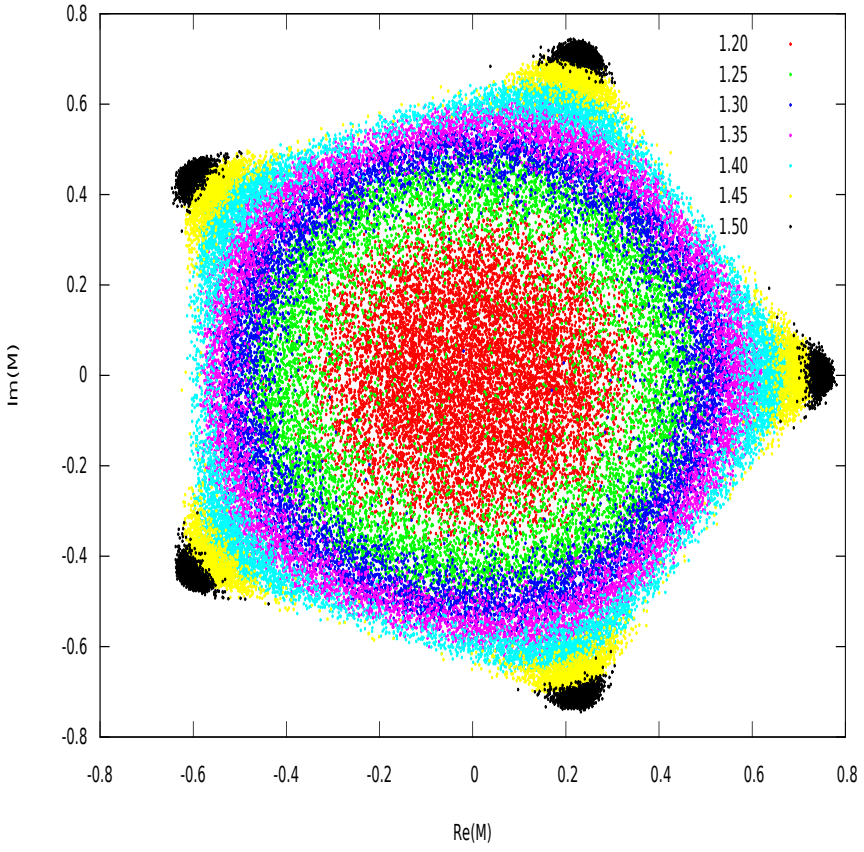

(B) $\lambda = 20.00$ and $\beta \in [1.20, 1.50]$ on a 128^2 lattice.

FIGURE 6.6: Scatter plots of the complex magnetization M_L in $SU(5)$.

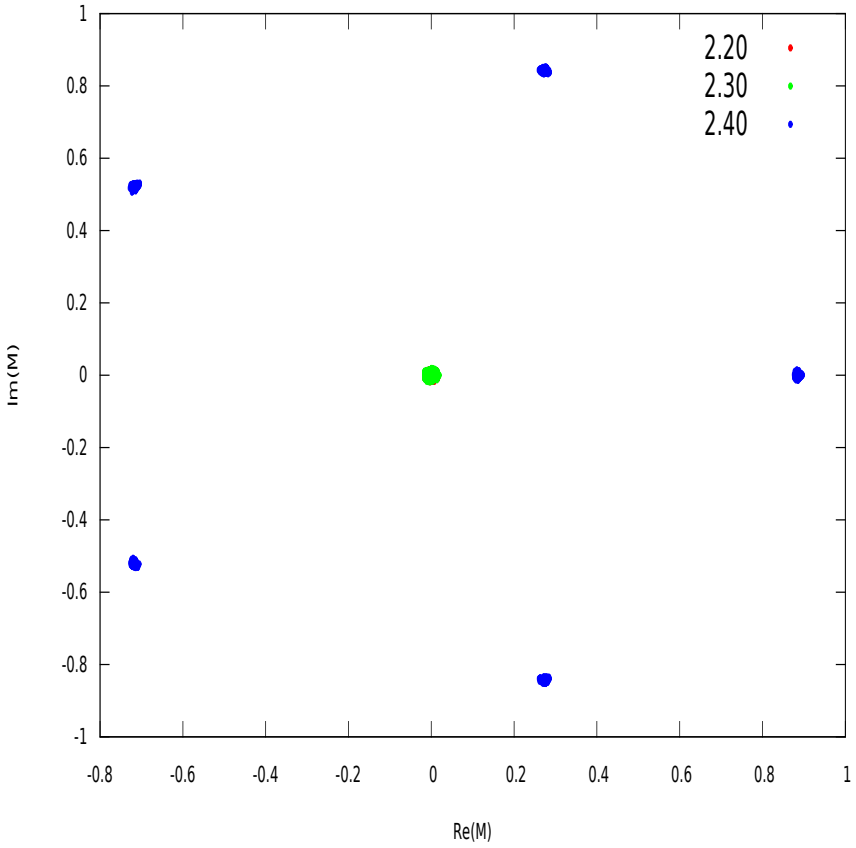

(A) $\lambda = 18.75$ and $\beta \in [2.20, 2.40]$ on a 32^2 lattice.

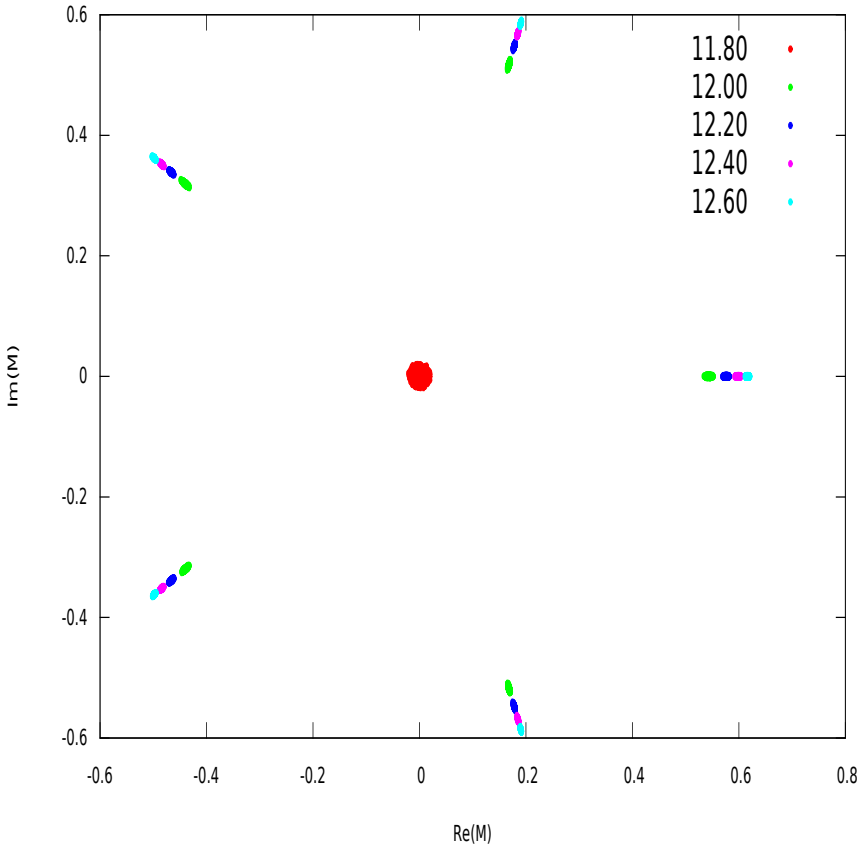

(B) $\lambda = 0.00$ and $\beta \in [11.80, 12.60]$ on a 128^2 lattice.

FIGURE 6.7: Scatter plots of the complex magnetization M_L in $SU(5)$.

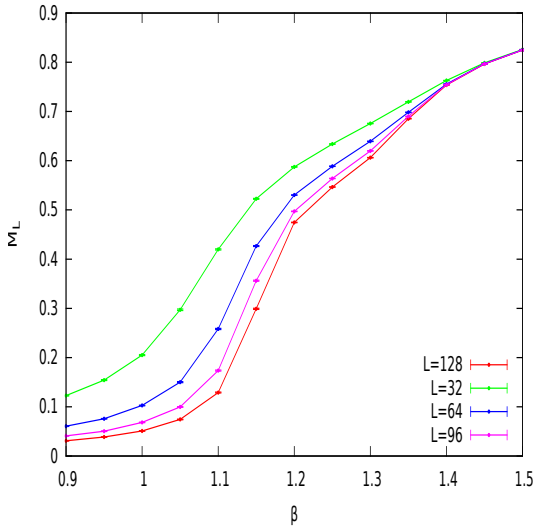

(A) $\lambda = 25.00$ and $\beta \in [0.90, 1.50]$ for $L = 32, 64, 96, 128$ lattice.

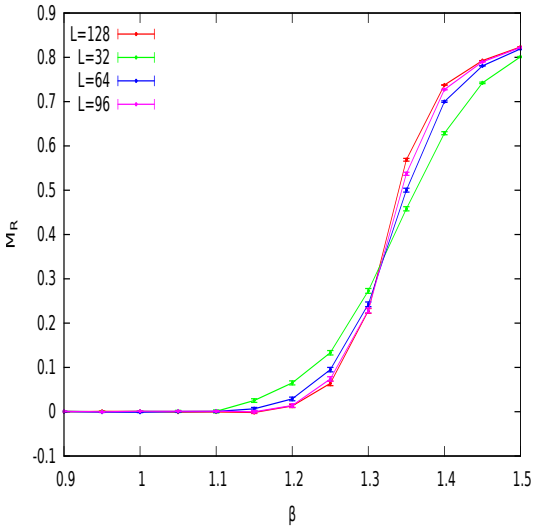

(B) $\lambda = 25.00$ and $\beta \in [0.90, 1.50]$ for $L = 32, 64, 96, 128$ lattice.

FIGURE 6.8: Plots of the complex magnetization M_L (Left) and the rotated magnetization M_R (Right) *versus* β in $SU(5)$.

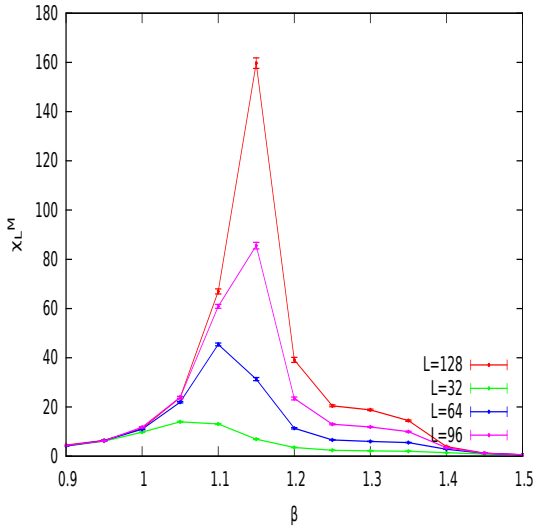

(A) $\lambda = 25.00$ and $\beta \in [0.90, 1.50]$ for $L = 32, 64, 96, 128$ lattice.

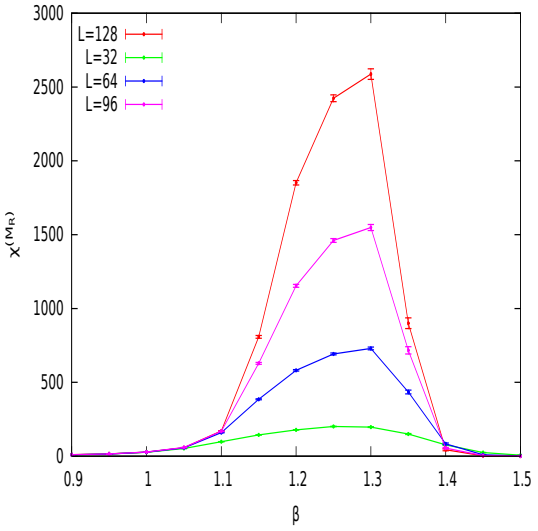

(B) $\lambda = 25.00$ and $\beta \in [0.90, 1.50]$ for $L = 32, 64, 96, 128$ lattice.

FIGURE 6.9: Plots of the susceptibility of complex magnetization $\chi^{(M_L)}$ (Left) and of the rotated magnetization $\chi^{(M_R)}$ (Right) *versus* β in $SU(5)$.

6.5 Summary and outlook

The just described investigation has been carried on with the final purpose of clarifying numerically the possibility for an infinite order BKT transition to take place in non-Abelian spin models. BKT transition have already been observed in a wide number of 2D Abelian spin models and 3D gauge theories. We have found clear evidence for such a transition in the $U(2)$ model, where the critical coupling has been approximately located at $\beta_c = 2.59$ and the critical indices η and β have been extracted from fits of the susceptibility and magnetization respectively to be

- $\eta = 0.24034 \pm 0.00314$;
- $\beta = -0.12746 \pm 0.00299$.

These values allow us to state that $U(2)$ spin models undergo BKT phase transitions in the universality class of the XY model, confirming the expectations coming from Kosterlitz-Thouless type RG analysis.

Our conclusions about the $SU(N)$ models are, instead, somehow preliminary in the sense that an interaction term in the adjoint representation, enhancing the role of the center $Z(N)$ of the $SU(N)$ group, had to be added and, currently, there is no compelling numerical evidence about the minimal λ values at which BKT transitions appear in these models. It would, indeed, be interesting to precisely locate λ_{min} and also investigate its dependence on N, hence on the size of the symmetry group. However, we were able to identify a three-phase structure both in $SU(5)$ and in $SU(8)$ spin models, in agreement, modulo the necessity of an extra interaction term, with the expectation that BKT transitions are to be found in $SU(N)$ models with nearest-neighbor interaction if N is sufficiently large. Clearly, the precise location of the critical coupling β at fixed λ, along with the extraction of the corresponding critical indices, would be the next step in this study, but it calls for simulations on much larger lattices.

Conclusions

In this work we have addressed numerically three main questions connected to as many phase transitions, which manifest themselves in the theory of strong interaction (deconfinement phase transition, Roberge-Weiss phase transition) and in 2D spin models characterized by non-Abelian symmetry groups (BKT phase transitions).

To conclude we briefly review our main results and the research perspectives of each investigation, but we refer to Secs. 4.8, 5.4, and 6.5 for more detailed summaries.

Our investigation on $SU(3)$ chromoelectric flux tubes (produced by the interaction of a quark-antiquark pair in the QCD vacuum) has, first of all, confirmed the validity of the dual superconductor model in the description of the confinement phenomenon at zero temperature. Our final aim was, however, to shed light on the fate of flux tubes across the deconfinement transition. In this respect, our results show that, despite a sensible drop in the intensity of the field, flux tubes do survive, and their shape is preserved, even in the deconfined phase. These findings suggest that the dual analogy with superconductivity, which is the basis of the dual superconductor model, cannot be pushed so far. It is reassuring, however, that there have been proposed alternative scenarios, predicting the existence of flux tubes in a "postconfinement" region, which is also expected on a phenomenological and experimental ground. The dedicated code written to accomplish the just described analysis, as an application within the MILC code for $SU(3)$ lattice gauge theory, lend itself to a meaningful future extension of our study to the case of full QCD, i.e. to $SU(3)$ lattice gauge theory with improved gauge action and dynamical quarks. Such an investigation could be relevant to clarify the formation of heavy mesons bound states in heavy-ion collisions at high energies.

The nature of the deconfinement/chiral transition, in QCD with $N_f = 2$ flavors of degenerate quarks, at imaginary chemical potential and, in particular, at the Roberge-Weiss endpoint, where the first-order critical lines of the Roberge-Weiss transition meet the continuation of the deconfinement/chiral transition lines at zero chemical potential, was the main focus of the second investigation described in this work. Results show that the order of the transition changes from first (triple) in the limit of infinite masses,

to second order at intermediate masses, to first order again in the limit of zero masses. Two tricritical masses were identified as in previous studies. This investigation represents indeed a step towards the continuum limit of recent analogous analysis and it is currently in progress.

Coming to our investigation on 2D spin models, where spins are traces of elements of non-Abelian groups $U(2)$ and $SU(N)$ with $N = 5, 8$ and nearest-neighbor interactions are considered, we were aiming at checking the existence of an infinite order BKT phase transition. Against the general belief that there are no such phase transitions in these models at any finite values of the coupling constants, we have found that $U(2)$ spin models do exhibit a BKT phase transition. Remarkably we have also found that the BKT phase transition observed in $U(2)$ spin models belongs to the universality class of 2D XY model. Furthermore also $SU(N)$ models are found to exhibit BKT phase transitions if an appropriate interaction term is included in the partition function for the system. The identification of the universality class for these phase transitions, as well as the determination of the minimal coupling (of the interaction term) allowing for BKT phase transitions call for future and more in-depth investigations.

Bibliography

[1] S. Elitzur (Dec 1975). "Impossibility of spontaneously breaking local symmetries". *Phys. Rev. D* 12:3978–3982 (cited in section 1.1).

[2] H. Nishimori and G. Ortiz (2010). *Elements of Phase Transitions and Critical Phenomena*. Oxford Graduate Texts. OUP Oxford (cited in section 1.2).

[3] J. Cardy (1996). *Scaling and Renormalization in Statistical Physics*. Cambridge Lecture Notes in Physics. Cambridge University Press .

[4] G. Mussardo (2009). *Statistical Field Theory: An Introduction to Exactly Solved Models in Statistical Physics*. Oxford Graduate Texts. OUP Oxford (cited in section 1.2).

[5] C.-N. Yang and R. L. Mills (1954). "Conservation of Isotopic Spin and Isotopic Gauge Invariance". *Phys. Rev.* 96:191–195 (cited in section 2.1).

[6] H. Rothe (2005). *Lattice Gauge Theories: An Introduction*. Lattice Gauge Theories: An Introduction. World Scientific (cited in sections 2.1.1, 2.2, and 3.1).

[7] L. D. McLerran and B. Svetitsky (1981). "Quark Liberation at High Temperature: A Monte Carlo Study of SU(2) Gauge Theory". *Phys. Rev.* D24:450 (cited in section 2.1.1).

[8] B. Svetitsky and L. G. Yaffe (1982). "Critical Behavior at Finite Temperature Confinement Transitions". *Nucl. Phys.* B210:423 (cited in sections 2.1.1 and 2.1.1).

[9] A. Roberge and N. Weiss (1986). "Gauge Theories With Imaginary Chemical Potential and the Phases of QCD". *Nucl. Phys.* B275:734 (cited in sections 2.1.2, 2.1.2, and 5.1).

[10] G. 't Hooft. *The Renormalization procedure for Yang-Mills Fields*. PhD thesis Utrecht U. (1972) (cited in section 2.1.3).

[11] H. D. Politzer (1973). "Reliable Perturbative Results for Strong Interactions?". *Phys. Rev. Lett.* 30:1346–1349 .

[12] D. J. Gross and F. Wilczek (1973). "Ultraviolet Behavior of Nonabelian Gauge Theories". *Phys. Rev. Lett.* 30:1343–1346 (cited in section 2.1.3).

[13] C. Gattringer and C. Lang (2009). *Quantum Chromodynamics on the Lattice: An Introductory Presentation*. Lecture Notes in Physics. Springer (cited in sections 2.2, 3.1, and 3.3).

[14] I. Montvay and G. Münster (1997). *Quantum Fields on a Lattice*. Cambridge Monographs on Mathematical Physics. Cambridge University Press (cited in sections 2.2, 3.1, and 3.3).

[15] K. G. Wilson (1974). "Confinement of Quarks". *Phys. Rev.* D10:2445–2459 (cited in section 2.2.1).

[16] C. Borgs and E. Seiler (1983). "Lattice Yang-Mills Theory at Nonzero Temperature and the Confinement Problem". *Commun. Math. Phys.* 91:329 (cited in section 2.2.1).

[17] P. Hasenfratz and F. Karsch (1983). "Chemical Potential on the Lattice". *Phys. Lett.* B125:308 (cited in section 2.2.4).

[18] H. Satz (2010). "The Thermodynamics of Quarks and Gluons". *Lect. Notes Phys.* 785:1–21 (cited in section 2.3).

[19] R. Hagedorn (1965). "Statistical thermodynamics of strong interactions at high-energies". *Nuovo Cim. Suppl.* 3:147–186 (cited in section 2.3).

[20] Y. Aoki, Z. Fodor, S. D. Katz, and K. K. Szabo (2006). "The QCD transition temperature: Results with physical masses in the continuum limit". *Phys. Lett.* B643:46–54 (cited in section 2.3).

[21] E. Newman and G. Barkema (1999). *Monte Carlo Methods in Statistical Physics*. Clarendon Press (cited in sections 3.1 and 3.3).

[22] D. Landau and K. Binder (2005). *A Guide to Monte Carlo Simulations in Statistical Physics*. Cambridge University Press .

[23] G. Fishman (2013). *Monte Carlo: Concepts, Algorithms, and Applications*. Springer Series in Operations Research and Financial Engineering. Springer New York .

[24] A. Kennedy and B. Pendleton (1985). "Improved Heat Bath Method for Monte Carlo Calculations in Lattice Gauge Theories". *Phys.Lett.* B156:393–399 .

[25] M. Creutz, L. Jacobs, and C. Rebbi (1983). "Monte Carlo Computations in Lattice Gauge Theories". *Phys.Rept.* 95:201 (cited in section 3.1).

[26] N. Metropolis, A. W. Rosenbluth, M. N. Rosenbluth, A. H. Teller, and E. Teller (1953). "Equation of state calculations by fast computing machines". *J. Chem. Phys.* 21:1087–1092 (cited in section 3.1.1).

[27] R. Petronzio and E. Vicari (1990). "An Overrelaxed Monte Carlo algorithm for SU(3) lattice gauge theories". *Phys. Lett.* B248:159–162 (cited in section 3.1.2).

[28] J. Von Neumann (1951). "13. Various Techniques Used in Connection With Random Digits" (cited in section 3.1.3).

[29] N. Cabibbo and E. Marinari (1982). "A New Method for Updating SU(N) Matrices in Computer Simulations of Gauge Theories". *Phys. Lett.* B119:387–390 (cited in sections 3.1.3, 4.5, and 4.6).

[30] D. J. E. Callaway and A. Rahman (1983). "Lattice Gauge Theory in Microcanonical Ensemble". *Phys. Rev.* D28:1506 (cited in section 3.1.4).

[31] J. Polonyi and H. W. Wyld (1983). "Microcanonical Simulation of Fermionic Systems". *Phys. Rev. Lett.* 51:2257. [Erratum: Phys. Rev. Lett.52,401(1984)] (cited in section 3.1.4).

[32] D. H. Weingarten and D. N. Petcher (1981). "Monte Carlo Integration for Lattice Gauge Theories with Fermions". *Phys. Lett.* B99:333 (cited in section 3.1.4).

[33] T. Takaishi and P. de Forcrand (2006). "Testing and tuning new symplectic integrators for hybrid Monte Carlo algorithm in lattice QCD". *Phys. Rev.* E73:036706 (cited in section 3.1.4).

[34] S. Duane, A. D. Kennedy, B. J. Pendleton, and D. Roweth (1987). "Hybrid Monte Carlo". *Phys. Lett.* B195:216–222 (cited in sections 3.1.4 and 5.2).

[35] C. Urbach, K. Jansen, A. Shindler, and U. Wenger (2006). "HMC algorithm with multiple time scale integration and mass preconditioning". *Comput. Phys. Commun.* 174:87–98 (cited in section 3.1.4).

[36] M. Albanese et al. (1987). "Glueball Masses and String Tension in Lattice QCD". *Phys. Lett.* B192:163–169 (cited in sections 3.2.1, 4.3, 4.5, and 4.6).

[37] A. Hasenfratz and F. Knechtli (2001). "Flavor symmetry and the static potential with hypercubic blocking". *Phys. Rev.* D64:034504 (cited in sections 3.2.2 and 4.3).

[38] A. D. Sokal (1989). "Monte Carlo mehtods in statistical mechanics: Foundations and New Algorithms" (cited in section 3.3).

[39] S. Basak and A. K. De (1998). "Kramers equation algorithm with Kogut-Susskind fermions on lattice". *Phys. Lett.* B430:320–325 (cited in section 3.3).

[40] G. t Hooft and A. Zichichi. High energy physics. In *EPS International Conference, Palermo* page 455 (1975) (cited in section 4).

[41] S. Mandelstam (1976). "Vortices and Quark Confinement in Nonabelian Gauge Theories". *Phys. Rept.* 23:245–249 (cited in section 4).

[42] P. Goddard, J. Goldstone, C. Rebbi, and C. B. Thorn (1973). "Quantum dynamics of a massless relativistic string". *Nucl. Phys.* B56:109–135 (cited in section 4).

[43] M. Bander (1981). "Theories of Quark Confinement". *Phys. Rept.* 75:205 (cited in section 4).

[44] J. Greensite (2003). "The Confinement problem in lattice gauge theory". *Prog. Part. Nucl. Phys.* 51:1 (cited in section 4).

[45] N. Arasaki, S. Ejiri, S.-i. Kitahara, Y. Matsubara, and T. Suzuki (1997). "Monopole action and monopole condensation in SU(3) lattice QCD". *Phys. Lett.* B395:275–282 (cited in section 4).

[46] P. Cea and L. Cosmai (2000). "A Gauge invariant study of the monopole condensation in nonAbelian lattice gauge theories". *Phys. Rev.* D62:094510 .

[47] P. Cea and L. Cosmai (2001). "Abelian monopole and vortex condensation in lattice gauge theories". *JHEP* 11:064 .

[48] A. Di Giacomo, B. Lucini, L. Montesi, and G. Paffuti (2000). "Color confinement and dual superconductivity of the vacuum. 2.". *Phys. Rev.* D61:034504 .

[49] P. Cea, L. Cosmai, and M. D'Elia (2004). "The Deconfining phase transition in full QCD with two dynamical flavors". *JHEP* 02:018 .

[50] A. D'Alessandro, M. D'Elia, and E. V. Shuryak (2010). "Thermal Monopole Condensation and Confinement in finite temperature Yang-Mills Theories". *Phys. Rev.* D81:094501 (cited in section 4).

[51] M. Fukugita and T. Niuya (1983). "Distribution of Chromoelectric Flux in SU(2) Lattice Gauge Theory". *Phys. Lett.* B132:374 (cited in section 4).

[52] J. E. Kiskis and K. Sparks (1984). "Illustrated Study of Flux Patterns in SU(2) Lattice Gauge Theory". *Phys. Rev.* D30:1326 .

[53] J. W. Flower and S. W. Otto (1985). "The Field Distribution in SU(3) Lattice Gauge Theory". *Phys. Lett.* B160:128 .

[54] J. Wosiek and R. W. Haymaker (1987). "On the Space Structure of Confining Strings". *Phys. Rev.* D36:3297 .

[55] A. Di Giacomo, M. Maggiore, and S. Olejnik (1990). "Evidence for Flux Tubes From Cooled QCD Configurations". *Phys. Lett.* B236:199 .

[56] A. Di Giacomo, M. Maggiore, and S. Olejnik (1990). "Confinement and Chromoelectric Flux Tubes in Lattice QCD". *Nucl. Phys.* B347:441–460 (cited in section 4.3).

[57] V. Singh, D. A. Browne, and R. W. Haymaker (1993). "Structure of Abrikosov vortices in SU(2) lattice gauge theory". *Phys. Lett.* B306:115–119 (cited in section 4.2).

[58] P. Cea and L. Cosmai (1993). "Lattice investigation of dual superconductor mechanism of confinement". *Nucl. Phys. Proc. Suppl.* 30:572–575 .

[59] Y. Matsubara, S. Ejiri, and T. Suzuki (1994). "The (dual) Meissner effect in SU(2) and SU(3) QCD". *Nucl. Phys. Proc. Suppl.* 34:176–178 .

[60] P. Cea and L. Cosmai (1994). "Dual superconductor mechanism of confinement on the lattice". *Nuovo Cim.* A107:541–548 (cited in section 4.2).

[61] P. Cea and L. Cosmai (1994). "On The Meissner effect in SU(2) lattice gauge theory". *Nucl. Phys. Proc. Suppl.* 34:219–221 .

[62] P. Cea and L. Cosmai (1995). "Dual Meissner effect and string tension in SU(2) lattice gauge theory". *Phys. Lett.* B349:343–347 .

[63] P. Cea and L. Cosmai (1995). "London penetration length and string tension in SU(2) lattice gauge theory". *Nucl. Phys. Proc. Suppl.* 42:225–227 .

[64] P. Cea and L. Cosmai (1995). "Dual superconductivity in the SU(2) pure gauge vacuum: A Lattice study". *Phys. Rev.* D52:5152–5164 (cited in section 4.2).

[65] G. S. Bali, K. Schilling, and C. Schlichter (1995). "Observing long color flux tubes in SU(2) lattice gauge theory". *Phys. Rev.* D51:5165–5198 .

[66] R. W. Haymaker and T. Matsuki (2007). "Model independent approach to studies of the confining dual Abrikosov vortex in SU(2) lattice gauge theory". *Phys. Rev.* D75:014501 .

[67] A. D'Alessandro, M. D'Elia, and L. Tagliacozzo (2007). "Dual superconductivity and vacuum properties in Yang-Mills theories". *Nucl. Phys.* B774:168–181 (cited in section 4).

[68] M. Tinkham (2004). *Introduction to Superconductivity: Second Edition.* Dover Books on Physics. Dover Publications (cited in sections 4.1 and 4.3).

[69] S.-A. Zhou (1999). *Electrodynamics of Solids and Microwave Superconductivity*. A Wiley interscience publication. Wiley (cited in section 4.1).

[70] J. Bardeen, L. N. Cooper, and J. R. Schrieffer (1957). "Microscopic theory of superconductivity". *Phys. Rev.* 106:162 (cited in section 4.1).

[71] J. Bardeen, L. N. Cooper, and J. R. Schrieffer (1957). "Theory of superconductivity". *Phys. Rev.* 108:1175–1204 (cited in section 4.1).

[72] F. London and H. London (1935). "The Electromagnetic Equations of the Supraconductor". *Proceedings of the Royal Society of London A: Mathematical, Physical and Engineering Sciences* 149(866):71–88. ISSN 0080-4630 (cited in section 4.1).

[73] V. Ginzburg and L. Landau (1950). "On superconductivity theory". *Zhurnal Eksperimental'noi i Teoreticheskoi Fiziki* 20:1064 (cited in section 4.1).

[74] V. Moshchalkov (cited in section 4.1).

[75] A. Rose-Innes and E. Rhoderick (1978). *Introduction to superconductivity*. International series in solid state physics. Pergamon Press (cited in section 4.2).

[76] A. A. Abrikosov (1957). "On the Magnetic properties of superconductors of the second group". *Sov. Phys. JETP* 5:1174–1182. [Zh. Eksp. Teor. Fiz.32,1442(1957)] (cited in section 4.1).

[77] P. Cea, L. Cosmai, and A. Papa (2012). "Chromoelectric flux tubes and coherence length in QCD". *Phys. Rev.* D86:054501 (cited in sections 4.2, 4.3, 4.5, and 4.7).

[78] J. R. Clem (1975). "Simple model for the vortex core in a type ii superconductor". *Journal of low temperature physics* 18(5-6):427–434 (cited in section 4.2).

[79] P. Cea, L. Cosmai, F. Cuteri, and A. Papa (2013). "Flux tubes and coherence length in the SU(3) vacuum". *PoS* LATTICE2013:468 (cited in section 4.2).

[80] P. Skala, M. Faber, and M. Zach (1997). "Magnetic monopoles and the dual London equation in SU(3) lattice gauge theory". *Nucl. Phys.* B494:293–311 (cited in section 4.3).

[81] P. Cea, L. Cosmai, F. Cuteri, and A. Papa (2014). "Flux tubes in the SU(3) vacuum: London penetration depth and coherence length". *Phys. Rev.* D89(9): 094505 (cited in sections 4.5, 4.6, and 4.8).

[82] P. Cea, L. Cosmai, F. Cuteri, and A. Papa (2014). "London penetration depth and coherence length of SU(3) vacuum flux tubes". *PoS* LATTICE2014:350 (cited in section 4.5).

[83] R. G. Edwards, U. M. Heller, and T. R. Klassen (1998). "Accurate scale determinations for the Wilson gauge action". *Nucl. Phys.* B517:377–392 (cited in sections 4.5 and 4.6).

[84] P. Cea, L. Cosmai, F. Cuteri, and A. Papa (2015). "Flux tubes at finite temperature". arXiv:1511.01783 (cited in section 4.6).

[85] P. Cea, L. Cosmai, F. Cuteri, and A. Papa. "Anatomy of $SU(3)$ flux tubes at finite temperature". In *Proceedings, 33rd International Symposium on Lattice Field Theory (Lattice 2015)* (2015). arXiv:1510.08993 (cited in section 4.6).

[86] O. K. Kalashnikov (1984). "QCD at finite temperature". *Fortsch. Phys.* 32:525 (cited in section 4.7).

[87] A. Nieto (1997). "Perturbative QCD at high temperature". *Int. J. Mod. Phys.* A12:1431–1464 (cited in section 4.7).

[88] G. S. Bali, J. Fingberg, U. M. Heller, F. Karsch, and K. Schilling (1993). "The Spatial string tension in the deconfined phase of the (3+1)-dimensional SU(2) gauge theory". *Phys. Rev. Lett.* 71:3059–3062 (cited in sections 4.7 and 4.7).

[89] F. Karsch, E. Laermann, and M. Lutgemeier (1995). "Three-dimensional SU(3) gauge theory and the spatial string tension of the (3+1)-dimensional finite temperature SU(3) gauge theory". *Phys. Lett.* B346:94–98 (cited in sections 4.7, 4.7, and 4.7).

[90] M. Caselle and P. Grinza (2012). "On the intrinsic width of the chromoelectric flux tube in finite temperature LGTs". *JHEP* 11:174 (cited in section 4.8).

[91] A. Shibata, K.-I. Kondo, S. Kato, and T. Shinohara (2013). "Non-Abelian dual superconductivity in SU(3) Yang-Mills theory: dual Meissner effect and type of the vacuum". *Phys. Rev.* D87(5):054011 (cited in section 4.8).

[92] P. Bicudo, M. Cardoso, and N. Cardoso (2014). "$SU(3)$ quark-antiquark QCD flux tube". *PoS* LATTICE2013:495 (cited in section 4.8).

[93] J. Liao and E. Shuryak (2007). "Strongly coupled plasma with electric and magnetic charges". *Phys. Rev.* C75:054907 (cited in section 4.8).

[94] O. Philipsen and C. Pinke (2014). "Nature of the Roberge-Weiss transition in $N_f = 2$ QCD with Wilson fermions". *Phys. Rev.* D89(9):094504 (cited in sections 5, 5.1, 5.2, 5.3, 5.2, 5.3, 5.8, and 5.4).

[95] F. Cuteri, C. Czaban, O. Philipsen, and C. Pinke. "The $N_f = 2$ chiral phase transition from imaginary chemical potential with Wilson Fermions". In *Proceedings, 33rd International Symposium on Lattice Field Theory (Lattice 2015)* (2015). arXiv:1511.03105 (cited in sections 5, 5.4, and 5.8).

[96] F. Cuteri, C. Czaban, O. Philipsen, and C. Pinke. "Roberge-Weiss transition in $N_f = 2$ QCD with Wilson fermions and $N_\tau = 6$". To be published. (cited in section 5).

[97] O. Philipsen (2012). "Status of the QCD Phase Diagram from Lattice Calculations". *Acta Phys. Polon. Supp.* 5:825–835 (cited in sections 5.1 and 5.1).

[98] C. Bonati, G. Cossu, M. D'Elia, and F. Sanfilippo (2011). "The Roberge-Weiss endpoint in $N_f = 2$ QCD". *Phys. Rev.* D83:054505 (cited in section 5.1).

[99] P. de Forcrand and O. Philipsen (2010). "Constraining the QCD phase diagram by tricritical lines at imaginary chemical potential". *Phys. Rev. Lett.* 105:152001 (cited in sections 5.1 and 5.3).

[100] M. D'Elia and F. Sanfilippo (2009). "The Order of the Roberge-Weiss endpoint (finite size transition) in QCD". *Phys. Rev.* D80:111501 (cited in section 5.1).

[101] A. Pelissetto and E. Vicari (2002). "Critical phenomena and renormalization group theory". *Phys. Rept.* 368:549–727 (cited in section 5.1).

[102] K. Binder (1981). "Finite size scaling analysis of Ising model block distribution functions". *Z. Phys.* B43:119–140 (cited in section 5.2).

[103] A. M. Ferrenberg and R. H. Swendsen (1989). "Optimized Monte Carlo analysis". *Phys. Rev. Lett.* 63:1195–1198 (cited in section 5.2).

[104] M. Bach, V. Lindenstruth, O. Philipsen, and C. Pinke (2013). "Lattice QCD based on OpenCL". *Comput. Phys. Commun.* 184:2042–2052 (cited in section 5.2).

[105] V. L. Berezinskiĭ (1971). "Destruction of Long-range Order in One-dimensional and Two-dimensional Systems having a Continuous Symmetry Group I. Classical Systems". *Soviet Journal of Experimental and Theoretical Physics* 32:493 (cited in sections 6 and 6.1).

[106] V. L. Berezinskiĭ (1972). "Destruction of Long-range Order in One-dimensional and Two-dimensional Systems Possessing a Continuous Symmetry Group. II. Quantum Systems". *Soviet Journal of Experimental and Theoretical Physics* 34: 610 (cited in section 6.2).

[107] J. M. Kosterlitz and D. J. Thouless (1973). "Ordering, metastability and phase transitions in two-dimensional systems". *Journal of Physics C: Solid State Physics* 6(7):1181 (cited in sections 6 and 6.1).

[108] B. Svetitsky and L. G. Yaffe (1982). "Critical behavior at finite-temperature confinement transitions". *Nuclear Physics B* 210(4):423–447 (cited in section 6).

[109] O. Borisenko, V. Chelnokov, F. Cuteri, and A. Papa. "BKT phase transitions in two-dimensional nonabelian spin models". To be published. (cited in section 6).

[110] M. Hasenbusch (2005). "The Two dimensional XY model at the transition temperature: A High precision Monte Carlo study". *J. Phys.* A38:5869–5884 (cited in section 6.4).

[111] M. Hasenbusch (2008). "The Binder cumulant at the Kosterlitz–Thouless transition". *Journal of Statistical Mechanics: Theory and Experiment* 2008(08):P08003 (cited in section 6.4).

[112] S. K. Baek, P. Minnhagen, and B. J. Kim (Dec 2009). "True and quasi-long-range order in the generalized q-state clock model". *Phys. Rev. E* 80:060101 (cited in section 6.4).

Acknowledgements

"We are like dwarfs perched on the shoulders of giants, and thus we are able to see more and farther [...]. And this is not at all because of the acuteness of our sight or the stature of our body, but because we are carried aloft and elevated by the magnitude of the giants."

Bernard of Chartres,

I like to borrow this suggestive picture to thanks, as an extremely lucky 'dwarf', the 'giants' upon whose 'shoulders' I could rely on.

Starting from the academic context, within which I have grown up in the last few years, I would like to express my gratitude to my supervisor Alessandro Papa for introducing me to the fascinating topics I have dealt with and for his guidance and precious advice. I am also very grateful to all my collaborators: in Bari (Paolo Cea and Leonardo Cosmai), Kiev (Oleg Borisenko and Volodymir Chelnokov) and Frankfurt (Owe Philipsen, Christopher Pinke, Alessandro Sciarra and Christopher Czaban). Thanks for your kind hospitality and, most of all, for having always been the go-to people for a friendly and expert scientific support.

For the best memories, travels, plans, laughters, tears, discussions and lunch and coffe breaks, I am deeply thankful to my wonderful friends: Vittoria, Filomena, Domenico, Beatrice, Caterina, Denise, Vassiliki, Stefania, Michela.

Coming to the best family ever, mine, I have to say I owe everything to them (parents, grandparents and brothers), for leading by example and for their constant support and affection that make me feel like home, no matter where I live, and make me feel encouraged, no matter what I do.

Finally thanks to you, Fabrizio (as well as to your family), even though, unfortunately, you deserve much more gratefulness than I can express in words.